LBL-10913

Lawrence Berkeley Laboratory

UNIVERSITY OF CALIFORNIA

Accelerator & Fusion Research Division

EVALUATION OF TWO-BEAM SPECTROSCOPY AS A PLASMA DIAGNOSTIC

Barton Dawes Billard
(Ph.D. thesis)

April 1980

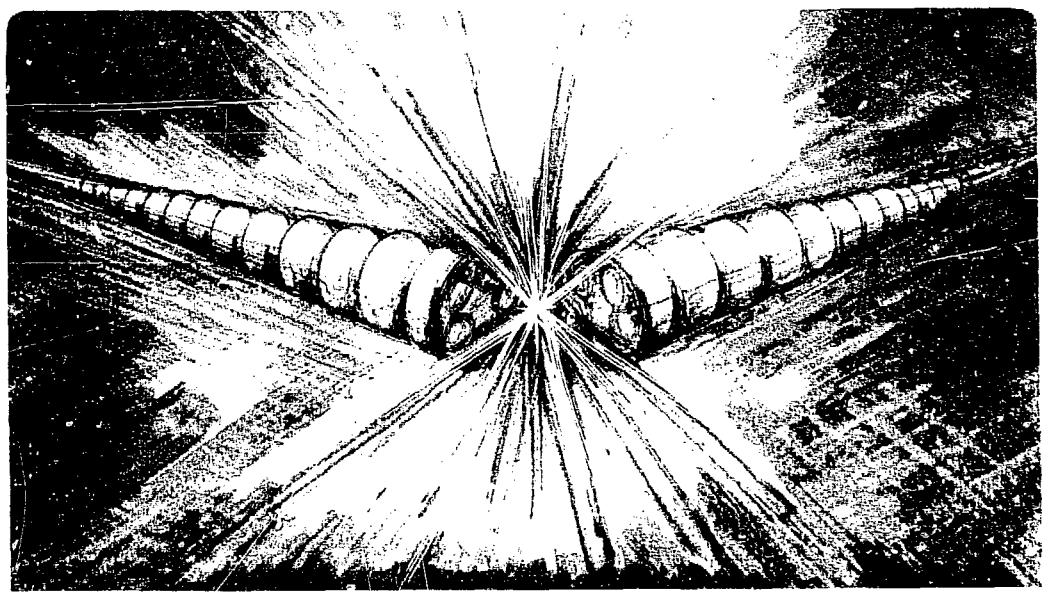

Prepared for the U.S. Department of Energy under Contract W-7405-ENG-48

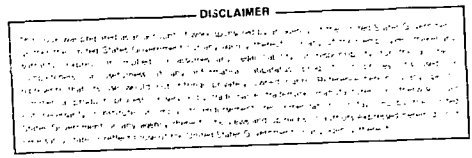

Evaluation of Two-Beam Spectroscopy as a Plasma Diagnostic

Barton Dawes Billard
Lawrence Berkeley Laboratory, University of California
Berkeley, California 94720

ABSTRACT

A two-beam spectroscopy (TBS) system is evaluated theoretically and experimentally. This new spectroscopic technique uses correlations between components of emitted light separated by a small difference in angle of propagation. It is thus a non-perturbing plasma diagnostic which is shown to provide local (as opposed to line-of-sight averaged) information about fluctuations in the density of light sources within a plasma--information not obtainable by the usual spectroscopic methods. The present design is an improvement on earlier systems proposed in a thesis by Rostler.

New theoretical analysis presented extends the range of validity beyond that of the original calculations by Rostler. Results show that the improved design, which abandons some of the components previously deemed essential, does not sacrifice any of the capabilities of the earlier systems in exchange for greater simplicity and increased light efficiency. In particular, these results demonstrate a new but equivalent mechanism of spatial resolution. As a further improvement, the new design also incorporates a practical means of wavelength compensation for use with broadband light sources.

The hot-cathode discharge and prototype TBS system built for evaluation of the technique are described. Efforts to show excitation of an ion-acoustic mode by a double grid as a test mode were unsuccessful, but spontaneous fluctuations in the discharge filled

with ∿ 150 mT of helium were detected using probes and a simple light detector. Attempts were made to detect the fluctuations with the prototype TBS system. More detailed probe studies of the fluctuation, compared with response of the system to a wave simulated by chopping the plasma light, show that the strength and coherence of the spontaneous fluctuation are inadequate to demonstrate the operation of the prototype system.

Substantial improvements are suggested by the evaluation of the prototype TBS system, and these are estimated to be sufficient to allow measurement of the fluctuations studied. The conditions of light emission rate and fluctuation amplitude and bandwidth encountered in this experiment are a basis for evaluating other possible applications of the TBS technique.

Wulf B. Kunkel
Chairman, Dissertation Committee

To my wife, Linda, and my parents, Jules and Dorothy Billard

for their encouragement and support

ACKNOWLEDGEMENTS

In the course of this work, many members of the Magnetic Fusion Energy Group and others at the Lawrence Berkeley Laboratory have made contributions for which I am happy to offer my thanks. In particular, I wish to thank my advisor, Professor Wulf B. Kunkel for his guidance, and Dr. Peter S. Rostler, Dr. William S. Cooper, Dr. J.W. Sterns, Kenneth Ehlers, and Bill Baker for their discussions and suggestions.

In addition, I especially wish to thank Dr. Kurt Schoenberg, Bruce Hammel, and Richard Gale for their assistance. James Galvin, Elliot B. Hewitt, Norman Abt, Dr. W.F. Steele, Jack Borde, Vince Honey, and Glenn Rankin have also helped in various capacities, as have members of the shops of Harlan Hughes, Lou Biagi, and Dane Anderberg.

Finally, I wish to thank my wife, Linda, for her encouragement throughout, and for her highly qualified contribution as technical editor and typist. In addition to my gratitude, I believe she merits a share of the credit for the quality of the final product.

This work was supported by the Fusion Energy Division of the U.S. Department of Energy under contract W-7405-ENG-48.

TABLE OF CONTENTS

CHAPTER I: INTRODUCTION

The use of two-beam spectroscopy (TBS) as a plasma diagnostic technique was first proposed in the generalized case by Rostler.[1,2] As first conceived, the technique involved making use of phase correlations in emitted light by observing interference effects upon recombining beams emitted in different directions by a distribution of incoherent sources such as a self-luminous plasma. A reason for using phase correlations is that correlations in light from incoherent sources must be due to those sources observed via both beams. By arranging a TBS system so that only a limited region may be seen with both beams, meaning that the beams cross and overlap only for part of their length, one can obtain a localized measurement instead of the usual line-of-sight average. Figure I.1[3] is an example of a system taking advantage of this method of making a localized measurement.

This thesis describes extensions of Rostler's work resulting in a TBS system that is more efficient and can also be used to advantage on plasmas emitting continuum light (such as bremsstrahlung or recombination radiation). Before outlining these improvements, a brief discussion of the basic concepts is presented.

Analysis shows that within the limited region of overlap (or common source volume), the measurement responds to a spatial Fourier component of fluctuations in the light source distribution. The system used as an example in Fig. I.1 is similar to a stellar interferometer[4] in front of which a lens has been placed for use with a nearby source of light (the plasma). The lens serves to form an image of the plasma

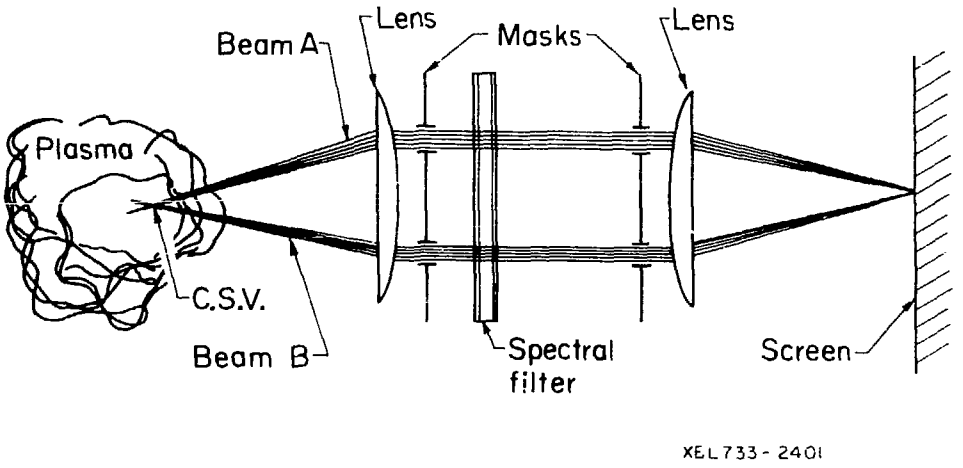

Figure I.1 Simple version of a TBS experiment. Sources in a limited region emit light into both beams. Detection of coherence between the two beams by interference effects, for example, is thus indication of information about sources in this common source region. Reproduced from Ref. 2.

at a distance, providing collimated light from the common source volume as the stellar interferometer receives collimated light from a star. In stellar interferometry, the angular diameter of a star is determined from the relationship between the visibility of the interference pattern produced on the screen (e.g., Fig. I.2 (a) and (b)[5]), to the distance D between the two apertures of the masks. If the star's diameter is much smaller than λ/D (where λ is the wavelength of light selected), the star acts as a point source and the interference pattern produced is sharp, as in Fig. I.2 (a). When D is increased until the fringes begin to become indistinct [Fig. I.2 (b)], the approximate angular diameter of the star is found as the resulting value of λ/D.

Evaluation of stellar interferometry assumes a simple pointlike or disklike distribution of sources. Substitution of a (nearby) plasma as in Fig. I.1 requires consideration of a more general distribution of sources. Each point source is capable of producing an interference pattern similar to that of Fig. I.2 (a). The position of the zero order interference fringe depends on the difference in path lengths to the two apertures in the last mask, which in turn depends on the position of the sources. With a distribution of incoherent sources one generally expects no interference pattern will be visible. The reason is that no interference occurs between incoherent sources, and the various individual interference patterns are shifted relative to one another by varying amounts in random fashion, so that the total intensity loses all the detail of the individual patterns.

A star which produces an indistinct pattern as in Fig. I.2 (b) is small enough that the cancellation of patterns is incomplete. More

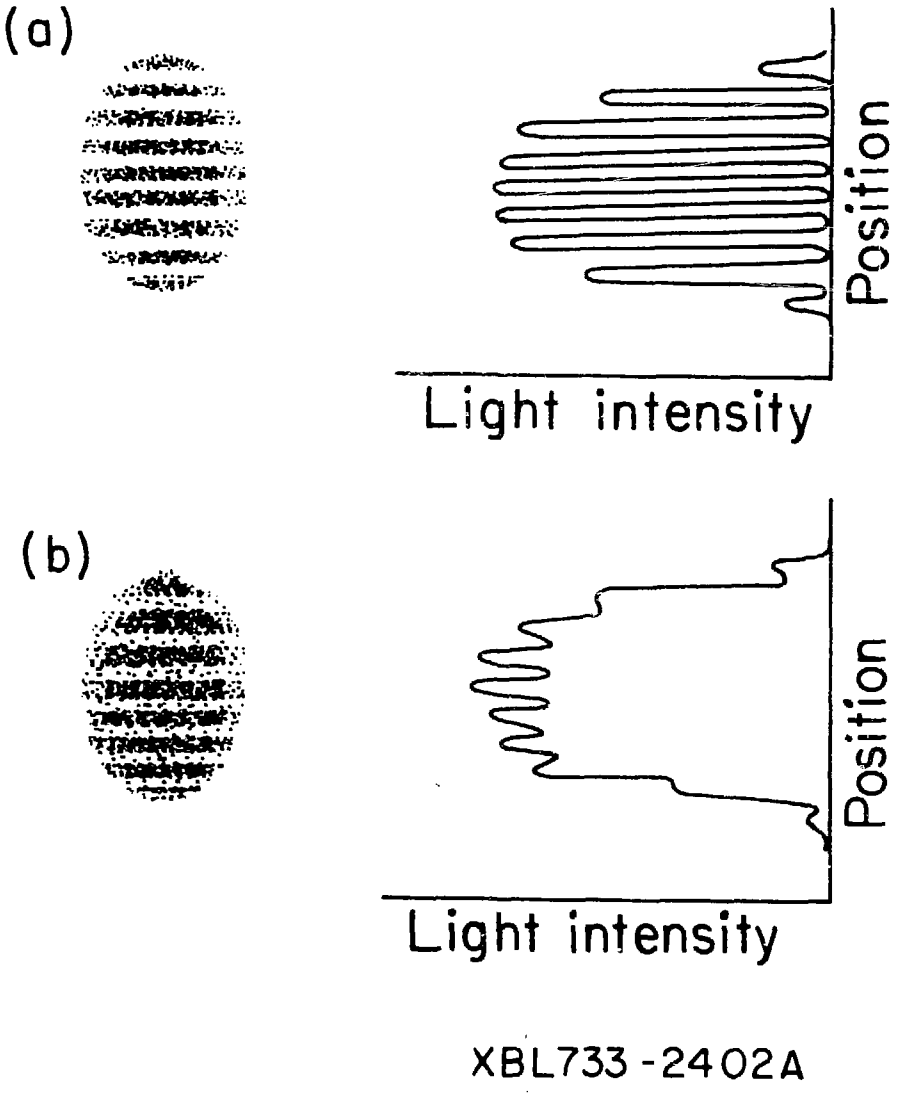

Figure I.2 Examples of interference patterns showing coherence in the light between the two beams. The sharp pattern in (a) shows highly coherent beams as from a single point source. Pattern (b) is partially visible showing some coherence due to a finite source distribution of limited extent or to certain distributions of sources. Reproduced from Ref. 2.

generally, in a plasma certain source distributions may be found which leave a residual pattern. If sources are distributed uniformly, no residual pattern results. If instead some correlation in their distribution results in a concentration of sources near positions for which the zero order fringe of the interference pattern is always located at an nth (where n is an integer) order fringe of some given pattern, then the majority of individual patterns will be similar to the given pattern. The total intensity will show some residual interference.

In the region near the focal point of the lens (and thus in the common source volume) these positions lie in planes perpendicular to the line between the apertures in the first mask and separated by integral multiples of the angle λ/D, as measured in the focal plane from the center of the lens. Hence, a fluctuation in the source distribution within the common source volume of wavenumber $k_\Delta = (2\pi/\lambda)D/f_1$ (where f_1 is the focal length of the first lens, and the wavevector is parallel to the line between the two apertures) results in a "visible" interference pattern. The degree of visibility depends on the amplitude of the fluctuation within the common source volume multiplied by the fraction of the total received light which originates there.

Thus Rostler proposed TBS as a plasma diagnostic technique which could be used to make localized measurements of fluctuations in light sources, or indirectly of other plasma fluctuations which affect the light sources. He analyzed the technique in a general way for light sources near the focal plane of the collimating lens. This analysis confirmed the conclusions from the simplified physical picture used above and suggested more practical designs, having greater light

gathering efficiency than the example in Fig. 1.1. Based on the idea of obtaining spatial resolution using distinct pairs of beams with a limited region of overlap, a multiple-beam system was proposed (Fig. I.3[6]) with a collimator to combine independent pairs of beams.

As noted by Rostler, information about the k_Δ component of the light source distribution is contained in light over a broad range of wavelengths that might be emitted by the plasma. In the system shown in Fig. I.3, the separation D between beams in each pair is determined by the properties of the calcite component, and will vary somewhat with wavelength. If a system is made in which D is proportional to wavelength, k_Δ becomes a constant. Then the TBS system could be used to advantage on plasmas emitting continuum light, such as bremsstrahlung or recombination radiation.

Such a system, which can be made achromatic,[7] is the subject of this thesis. It is based on a simple interferometer, which is analyzed in detail in the first three appendices. Appendix B explains the wavelength compensation possible. The body of the thesis includes a theoretical analysis in Chapter II and discussion of the experimental evaluation of a prototype TBS system in Chapter IV. Chapter III contains a more practically oriented qualitative physical description of TBS and is intended as a bridge between the theory and the experiment, as well as a basis for designing similar systems. The approach is along the lines of the introductory description above, but it covers the range of experimental considerations from the plasma and its light, to the optical system, detectors and amplifier, and the signal extraction from the inherent noise. The final chapter contains a discussion of possible improvements and conclusions. In the

Figure I.3 Multiple-beam system obtained by combining a number of pairs of beams using a calcite rhomb to shift one beam (the extra-ordinary polarization) of each pair. Combining the beams and using polarization interference allows detection of coherence by finding a net polarization from a comparison of intensities for the two resultant polarization directions. The purpose of the Glan-Thompson prism and pair of photomultiplier tubes is to make this intensity comparison. Reproduced from Ref. 2.

A multiple-beam spectrometer

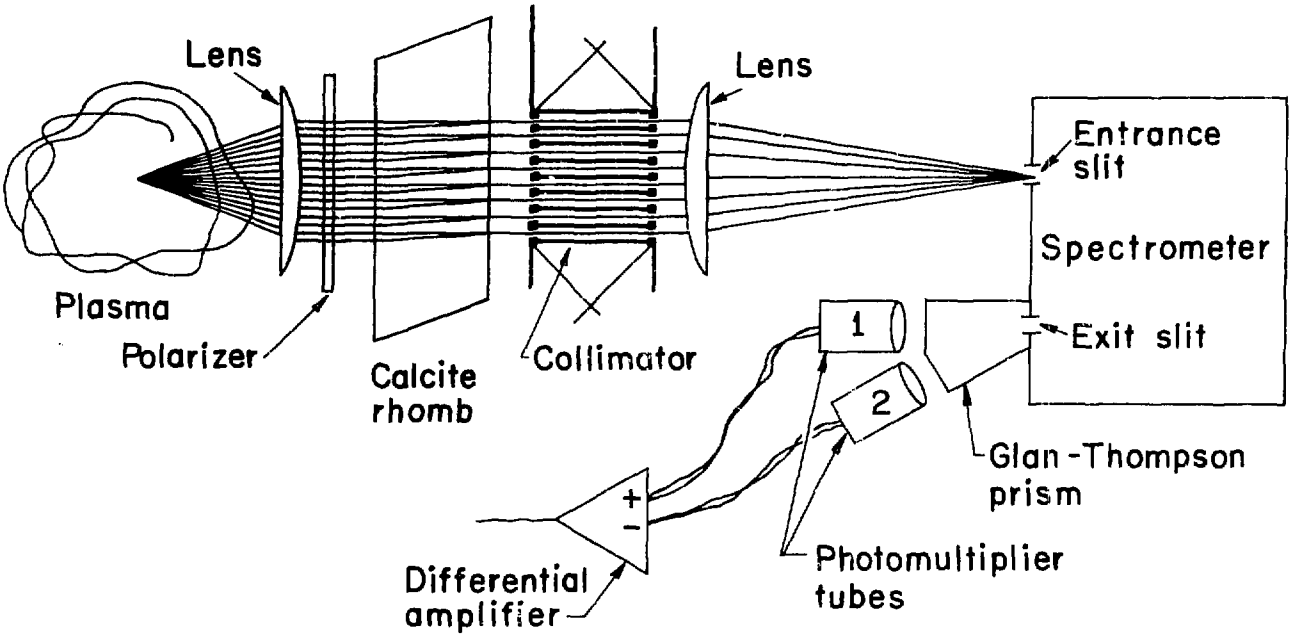

Figure 1.3

XBL 7210-4329

following discussion some of the highlights of this report are outlined.

In the multiple-beam system (Fig. 1.3), each beam pair has an aperture limited to less than or order of one-half of the spacing between the pairs, in order to limit the common source volume. If the aperture is larger than the spacing, then the beams are not completely separated, and the common source volume is not localized. For small values of k_Δ, it becomes difficult to limit the common source volume because of the correspondingly small spacing D between the beam pairs. In this thesis, a new configuration is explored in which no attempt is made to limit the common source volume. It follows that the aperture width is not limited, and it is unnecessary to use a multiple beam configuration--one pair of broad, overlapping beams covers the entire system aperture.

This new configuration was initially of interest as a way to use as much of the light as possible in a situation where the combination of the fluctuation wavenumber k_Δ and the plasma size made it difficult to show any spatial resolution. The common source volume would have exceeded the plasma thickness in any case. In addition to increasing the fraction of the available aperture used, eliminating the collimator also relaxes restraints on the angle of light acceptance of the system, for even greater light collection.

However, the supposed sacrifice of spatial resolution turns out to be unnecessary. Qualitative analysis of the new configuration as in the approach of Chapter III suggests another way of achieving spatial resolution. For a source position sufficiently far from the focal plane of the collimating lens, variation of the interference

effect for different portions of the uncollimated (curved) wavefronts tends to cancel the effect sought. This possibility suggests the need for a reformulation of Rostler's analysis for this configuration, with an extension to include light sources farther from the focal plane of the collimating lens than the approximations used by him allowed. Chapter II presents the new analysis, which confirms that spatial resolution is not dependent on the formation of a localized common source volume. Thus the new configuration is a substantial improvement on Rostler's multiple-beam system, even when spatial resolution is an important feature of the application.

Whatever the method used, spatial resolution does come with a sacrifice in the fractional part of the light which contributes to the signal. If the fluctuation to be detected is confined to some fraction of the depth of the plasma, only that fraction of the light received can contain a signal. The signal is diluted by the light from the rest of the plasma that the system must look through. This has important consequences for the signal-to-noise ratio of the measurement. As explained in Chapter III, an important noise component is the statistical fluctuations in the total light, due to the fact that light consists of photons, and intensities predicted must be interpreted as probabilities of arrival or detection of the photons.

Rostler first tested a multiple-beam system of the type illustrated in Fig. I.3. Optical tests with laser light showed satisfactory interference effects with ordinary quality optical components. This minimal sensitivity to imperfections is due to the fact that the two interfering beams are always quite close to each other as they pass through the system. Vibrations or imperfections tend to

affect both beams equally.

A test of the system as a diagnostic for plasma waves was then tried using an electron beam-plasma discharge produced by a 4 kV, 30 mA electron beam along the axis of a 7 kG magnetic field in a chamber with helium at 0.3 mTorr. Based on pulse propagation tests showing excitation of density perturbations with speeds near the expected ion acoustic speed, a negatively biased Langmuir probe driven with a sinusoidal signal of 10 to 50 MHz was used to provide the multiple-beam system with disturbances with wavelengths of a fraction of a millimeter. Results clearly indicated a signal detected by the multiple-beam system associated with the light. (To select this signal, the light was chopped to allow phase-sensitive detection techniques.)

I continued the work with this apparatus and was able to repeat the above results. Rostler suggested testing the polarization dependence of the signal, as the system uses polarization interference, requiring an initial polarizer oriented to provide equal components for the pairs of beams. Rotating the polarizer 45 degrees would result in transmission of only one beam, making the system inoperative, alhtough it still transmits the same amount of light.

The signal failed this polarization dependence test. I then substituted an unrelated light source (a microscope lamp) for the plasma light and found the signal still remained. The explanation appears to be that the signal is not from a wave driven in the plasma, but from spurious coupling of the driving voltage to the detection electronics. In order for the spurious signal to pass the phase-sensitive detection, it must be impressed on the output of the photomultipliers, presumably by modulation in some nonlinear part of the

electronics. Unfortunately, the signal from the light is in the form of pulses amplified by the photomultipliers, and they are quite likely to be sharp enough to drive the spectrum analyzer nonlinear in an early stage before unwanted frequency components are eliminated. Much of the frequency selection is in the intermediate frequency(IF) stages, and the conversion to IF is, of course, accomplished by a modulation circuit.

After the beam-plasma device succumbed to the advance of the neutral beam test stands, it became necessary to build a new plasma and provide a known wave in the plasma for a test of the new TBS configuration. Chapter IV describes the positive column plasma chosen, and the attempts to obtain a suitable wave, either as externally driven (by grids) or as spontaneous fluctuations of the plasma.

Spontaneous fluctuations were found with the helium positive column, and a prototype TBS system in the new configuration was designed and constructed for testing with the plasma. More detailed probe measurements of the spontaneous fluctuations proved necessary for correlation with the TBS measurements. These probe measurements provided cross power spectral density information as a function of both frequency and wavenumber. The results showed the coherence and intensity of the fluctuations were not quite sufficient to provide an adequate signal-to-noise ratio with the prototype TBS system.

Nonetheless, experience with the prototype was helpful in determining problem areas, and possibilities for improvement are discussed in the final chapter, in which it is estimated that a larger, more efficient system could offer up to two orders of magnitude increase in sensitivity. Substantial data acquisition and analysis gains are

also possible with appropriate equipment, and actually might be sufficient with the present system for measuring the wave available. It is worth noting that this spontaneous wave is not a well-defined test wave tailored for providing a TBS signal as hoped. Rather it is a fairly incoherent fluctuation of moderate amplitude more typical for a possible application of this new technique.

REFERENCES

1. P.S. Rostler, W.S. Cooper, and W.B. Kunkel, Bull. Am. Phys. Soc. 17, 986 (1972).
2. P.S. Rostler, Ph.D. Thesis, University of California, Berkeley (1974) (unpublished).
3. Ibid., Figure II.2.
4. R.H. Brown, Ann. Rev. Astron. Astrophys. 6, 13 (1968).
5. P.S. Rostler, Ph.D. Thesis, University of California Berkeley (1974) (unpublished), Fig. II-3 (b) and (c).
6. Ibid., Fig. C-7.
7. B.D. Billard, W.S. Cooper, and W.B. Kunkel, Bull. Am. Phys. Soc. 19, 975 (1974).

CHAPTER II: THEORETICAL PRINCIPLES

An understanding of the application of TBS as a diagnostic technique for a plasma wave involves two considerations. First, a theoretical explanation of TBS is needed, showing how information about correlations in the distribution of incoherent light sources is contained in detectable correlations, or coherence, in light emitted in different directions from one region. The second consideration is what plasma phenomena are involved. We must understand how the distribution of light sources in the plasma is influenced by the wave in question so that it may be detected by TBS.

Rostler's[1] report on multiple-beam spectroscopy explains the general formalism he devised for analyzing systems designed to use coherence effects in the emitted light, and applies the analysis to a number of types of systems. In this experiment a new type of system[2] is used. In part A of this chapter, Rostler's analysis is modified and extended to this new system. (A more intuitive approach, along the lines of Rostler's preliminary discussion of TBS, is presented in section B of Chapter III, where the important components and features are discussed to help in the adaptation of this type of TBS to various applications.) Interesting new conclusions are reached regarding the spatial resolution of TBS.

In part B of this chapter, some of the possible plasma phenomena involved are explained. The theory of ion acoustic waves is presented briefly, followed by a discussion of the mechanisms by which light intensity is modulated by plasma phenomena.

A. Analysis of Two-Beam Spectroscopy (TBS)

Rostler[3] applies his formalism to analyze a general type of system, illustrated by Fig. II.1 (a) (Rostler's Fig. II.6). The important characteristics of the design used for this experiment are illustrated for comparison in Fig. II.1 (b). Although the dual path optical system substituted for the birefringent system does not necessarily use anisotropic materials (having different refractive indices for different polarization components), Rostler's analysis does not distinguish the two. The birefringent system should be considered as including some type of exit arrangement of masks with one or more apertures, of which the aperture in Fig. II.1 (b) is a specific example. The analyzer and detectors added in Fig. II.1 (b) are like the analyzer and detectors not shown in Fig. II.1 (a), but which are assumed to exist beyond the slit. The dual path optical system in this discussion represents the interferometer analyzed in Appendix A, with additional details in Appendices B and C. In this section Rostler's analysis is outlined, then the arrangement in Fig. II.1 (b) is considered. Certain extensions and adaptations of Rostler's analysis are required, and the results are compared with some arrangements analyzed by him.

Briefly, Rostler's analysis calculates, in the Huygens' approximation of classical optics, the contributions to the fields at points $\underline{r}''$ (at the slit entrance to the analyzer) due to sources in the vicinity of the points $\underline{r}'$ within the plasma. Two fields, $\xi_A(\underline{r}'',\omega;\underline{r}')$ and $\xi_B(\underline{r}'',\omega;\underline{r}')$, represent the equal components "A" and "B" into which the initial polarization component selected is resolved by the optical system (see Fig. II.2). The two linear relations found for the two components may be expressed as

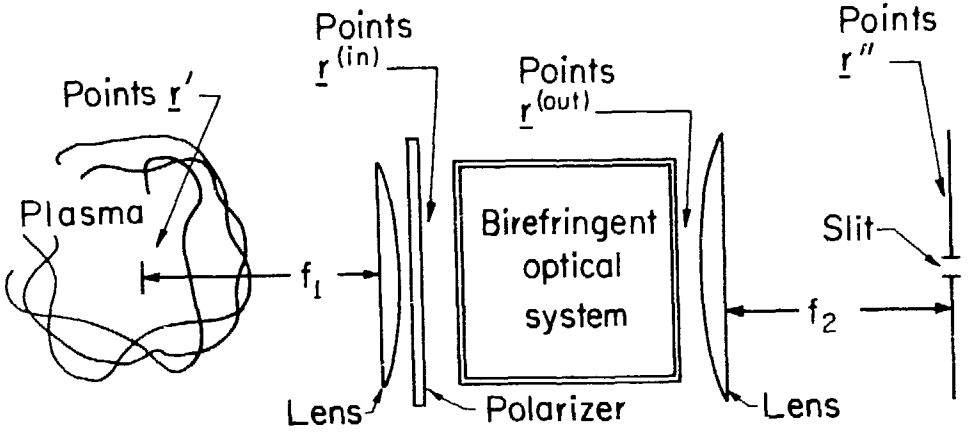

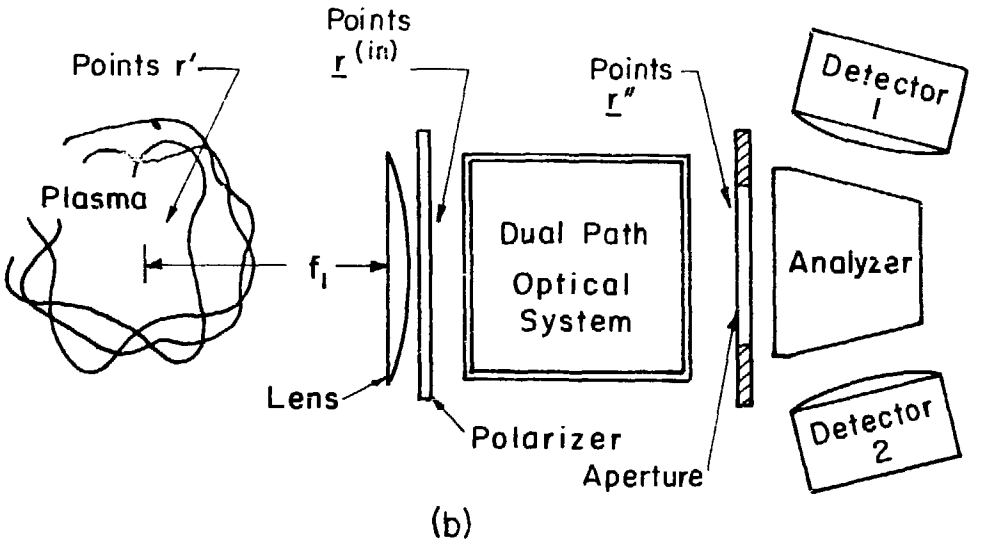

XBL802-4651

Figure II.1 (a) General type of two-beam or multiple-beam spectroscopy system analyzed by Rostler for points r' near the focal plane of the collimating lens. From Ref. 1.

(b) Type of TBS system to be analyzed in this chapter. In this system a large aperture defines overlapping beams with negligible diffraction effects.

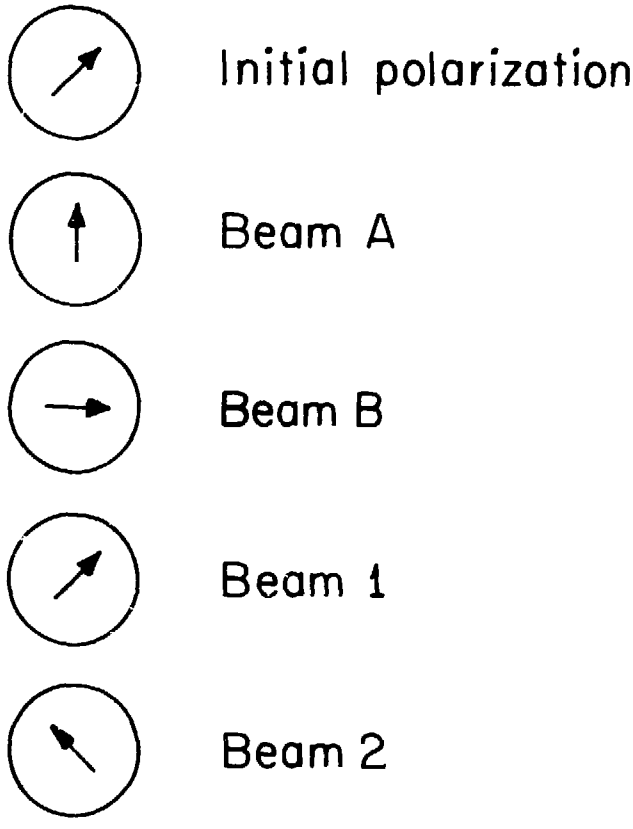

Figure II.2 Relation of polarization components of TBS system. From Ref. 1.

$$\xi_{A,B}(\underline{r}'',\omega;\underline{r}') = \phi_{A,B}(\underline{r}'',\underline{r}',\omega)s(\underline{r}',\omega), \qquad \text{(II-1)}$$

where $s(\underline{r}',\omega)$ is the (scalar) source density contributing to the initial polarization component. In the analyzer the resultant field is separated into intermediate components "1" and "2" (Fig. II.2),

$$\xi_1 = \frac{1}{\sqrt{2}}(\xi_A + \xi_B)$$
$$\xi_2 = \frac{1}{\sqrt{2}}(\xi_A - \xi_B); \qquad \text{(II-2)}$$

and their intensities are compared. Since the sources are incoherent, they cannot interfere with each other. Their intensities are determined separately and then integrated over the plasma volume. The signal, which is the difference in intensity for the components "1" and "2," is then found to depend only on a spatial component of the spectral density of the source distribution

$$\mathcal{S}(\omega;\underline{r}',t) = |s(\underline{r}',\omega;t)|^2, \qquad \text{(II-3)}$$

selected by the effects of the transfer functions $\phi_{A,B}$. (A slow time dependence is introduced in the Fourier transform to represent the time dependent spectrum of the light obtained experimentally.)

The procedure is illustrated below as it applies to the analysis of the system used in the experiment. Differences in approach appropriate for this system are pointed out. They allow extension of the validity beyond the region allowed by Rostler's approximations.

Because a single polarization component is selected, the amplitude is represented by a scalar field $\xi(\underline{r},t)$ obeying the scalar wave equation[4]

$$\nabla^2\xi(\underline{r},t) - \frac{1}{c^2}\frac{\partial^2}{\partial t^2}\xi(\underline{r},t) = -4\pi s(\underline{r}',t), \qquad \text{(II-4)}$$

where $s(\underline{r}',t)$ (assumed isotropic) is the scalar source density for

this component. The plasma is assumed to have no interaction with the waves other than the emission indicated in Eq. (II-4). (The plasma is optically thin and has a dielectric constant equal to unity.) In the space surrounding the plasma this has the retarded solution[5]

$$\xi(\underline{r},t) = \int d^3r' \frac{1}{|\underline{r} - \underline{r}'|} s\left(\underline{r}', t - \frac{|\underline{r} - \underline{r}'|}{c}\right). \qquad \text{(II-5)}$$

Using the thin lens approximation for points $\underline{r}^{in}$ immediately following the lens, the solution has an additional retardation term,

$$-\frac{\phi_1(\underline{r}^{in})}{c} = -\frac{1}{c}\left[\phi_{10} - \tfrac{1}{2}\frac{(x^{in})^2 + y^{in})^2}{f_1}\right], \qquad \text{(II-6)}$$

in the time at which the source density is evaluated. In this equation f_1 is the focal length of the lens, and it is assumed that the coordinates of the point $\underline{r}^{in}$ are (x^{in},y^{in},z^{in}), with the axis of the lens corresponding to the z axis.

The interferometer analyzed in Appendix A is now used as an example of the dual path optical system. Rather than integrating the wave equation [Eq. (II-4)] for the field $\xi(\underline{r}^{in},t)$ immediately beyond the lens, we can determine the propagation through the system as a superposition of solutions for fields from small regions d^3r' of sources near each point $\underline{r}'$. We rewrite Eq. (II-5):

$$\xi_o(\underline{r}^{in},t) = \int d^3r' \xi_o(\underline{r}^{in},t;\underline{r}'), \qquad \text{(II-7)}$$

where

$$\xi_o(\underline{r}^{in},t;\underline{r}') = \frac{1}{|\underline{r}^{in} - \underline{r}'|} s\left[\underline{r}', t - \frac{|\underline{r}^{in} - \underline{r}'| + \phi_1(\underline{r}^{in})}{c}\right] \qquad \text{(II-8)}$$

[from Eqs. (II-5) and (II-6)] is the field at $\underline{r}^{in}$ due to sources near $\underline{r}'$.

The purpose of this representation is to provide a more geometrical method of analyzing the propagation through the system. Viewed in this way Eq. (II-5) can be seen as a superposition of spherical wavefronts from the points $\underline{r}'$. Geometric optics suggests that the fields following the lens [$\xi_o(\underline{r}^{in},t;\underline{r}')$ in Eq. (II-8)] are also spherical wavefronts centered on the image $\underline{r}_c'$ of $\underline{r}'$. As the analysis of Appendix A indicates, we assume negligible diffraction effects (the apertures and hence the wavefronts passed are very large compared with the wavelength of the light--conditions appropriate for the geometric optics approximation), and determine the propagation through the interferometer by applying the transformation appropriate to the reflections undergone for each polarization component. We identify a wavefront by finding the points $\underline{r}^{in}$ such that $\xi_o(\underline{r}^{in},t;\underline{r}')$ in Eq. (II-8) is the same at the same time t. In this short-wavelength approximation, we can do this by finding the points $\underline{r}^{in}$ such that the retardation in Eq. (II-8) is constant, neglecting variations in the amplitude factor $1/|\underline{r}^{in} - \underline{r}'|$ compared with the rapid variation of s with retarded time.

With the spherical wavefront approximation, the amplitude is expressed as

$$\xi_o(\underline{r}^{in},t;\underline{r}') = \left|\frac{\rho_o^{in}}{\rho^{in}}\right| \xi_o(\underline{r}_o^{in},t - \frac{\rho^{in} - \rho_o^{in}}{c};\underline{r}'), \qquad \text{(II-9)}$$

where (see Fig. II.3) ρ^{in} and ρ_o^{in} are the (signed) radii of curvature of two wavefronts passing through points $\underline{r}^{in}$ and $\underline{r}_o^{in}$. The radii are positive (negative) for diverging (converging) wavefronts:

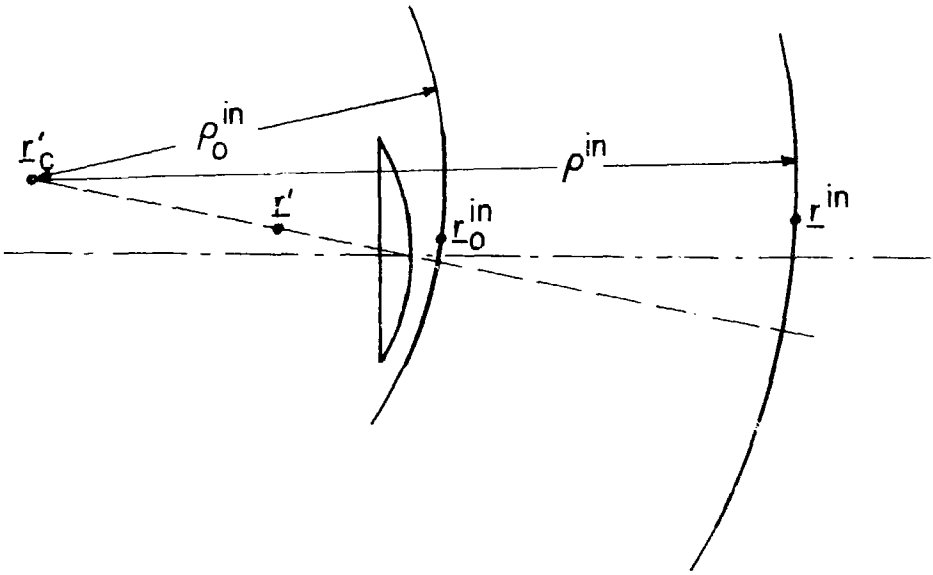

XBL 803-4919

Figure II.3 Radii of curvature of the wavefronts obtained by assuming spherical wavefronts propagating beyond the lens as if from the image point $\underline{r}_c$. The radii ρ_o^{in} and ρ^{in} are obtained from the wavefronts at points $\underline{r}_o^{in}$ and $\underline{r}^{in}$ respectively.

$$|\rho_o^{in}| = |\underline{r}_o^{in} - \underline{r}_c'|$$

$$|\rho^{in}| = |\underline{r}^{in} - \underline{r}_c'|$$

$$\text{sign}(\rho_o^{in}) = \text{sign}[(\underline{r}_o^{in} - \underline{r}_c')\cdot(\underline{r}_o^{in} - \underline{r}')]$$

$$\text{sign}(\rho^{in}) = \text{sign}[(\underline{r}^{in} - \underline{r}_c')\cdot(\underline{r}^{in} - \underline{r}')], \qquad \text{(II-10)}$$

where $\underline{r}_c'$ is the image of $\underline{r}'$ formed by the lens.

In Appendix A the transformations found appropriate for the type of interferometer used in the experiment are rotations about parallel axes by the same angle:

$$\begin{aligned} R_A &= R_{\underline{x}_A}(\hat{e}, 2\theta) \\ R_B &= R_{\underline{x}_B}(\hat{e}, 2\theta). \end{aligned} \qquad \text{(II-11)}$$

Since these preserve the relations between vectors used in determining the propagation of the fields, the rotations may be applied before or after calculating the wavefront propagation. The field at points $\underline{r}''$ in the aperture of the analyzer is then given by the components

$$\xi_{A,B}(\underline{r}'', t; \underline{r}') = \frac{1}{\sqrt{2}}\, \xi_o(R_{A,B}\underline{r}^{in}, t; \underline{r}') \qquad \text{(II-12)}$$

where

$$\underline{r}'' = R_{A,B}\underline{r}^{in} \qquad \text{(II-13)}$$

can be solved as

$$\underline{r}_{A,B}^{in} = R_{A,B}^{-1}\underline{r}'' \qquad \text{(II-14)}$$

for the two beams. Thus, the interferometer serves to superpose (at $\underline{r}''$) the components which would reach the two points $\underline{r}_A^{in}$ and $\underline{r}_B^{in}$ in the absence of the interferometer. Equations (II.8), (II-9), (II-12), and (II-14) are combined to obtain

$$\xi_{A,B}(\underline{r}'',t;\underline{r}') =$$

$$\frac{1}{\sqrt{2}}\left|\frac{\rho_o^{in}}{\rho_{A,B}\underline{r}''}\right| \frac{1}{|\underline{r}_o^{in}-\underline{r}'|}\, s\left[\underline{r}', t - \frac{|\underline{r}_o^{in}-\underline{r}'|+\phi_1(\underline{r}_o^{in})-\rho_{A,B}(\underline{r}'')+\rho_o^{in}}{c}\right] \quad \text{(II-15)}$$

where $\rho_{A,B}(\underline{r}'')$ stands for ρ^{in} evaluated for $\underline{r}^{in} = R_{A,B}^{-1}\underline{r}'' = \underline{r}_{A,B}^{in}$. Next the Fourier transform in time,

$$\tilde{\xi}_{A,B}(\underline{r}'',\omega;\underline{r}') = \int_{-\infty}^{\infty} dt\; e^{i\omega t}\xi_{A,B}(\underline{r}'',t;\underline{r}'), \quad \text{(II-16)}$$

is app ied to Eq. (II-15) to obtain a relation of the form given in Eq. (II-1):

$$\tilde{\xi}_{A,B}(\underline{r}'',\omega;\underline{r}') =$$

$$\int_{-\infty}^{\infty} dt\, \frac{e^{i\omega t}|\rho_o^{in}|}{\sqrt{2}|\rho_{A,B}(\underline{r}'')||\underline{r}_o^{in}-\underline{r}'|}\, s\left[\underline{r}', t - \frac{|\underline{r}_o^{in}-\underline{r}'|+\phi_1(\underline{r}_o^{in})-\rho_{A,B}(\underline{r}'')+\rho_o^{in}}{c}\right]$$

$$= \frac{|\rho_o^{in}|\exp\{i\,\frac{\omega}{c}[|\underline{r}_o^{in}-\underline{r}'|+\phi_1(\underline{r}_o^{in})-\rho_{A,B}(\underline{r}'')+\rho_o^{in}]\}}{\sqrt{2}|\rho_{A,B}(\underline{r}'')||\underline{r}_o^{in}-\underline{r}'|}\int_{-\infty}^{\infty} dt'\; e^{i\omega t'}s(\underline{r}',t')$$

$$= \frac{|\rho_o^{in}|\exp\{i\,\frac{\omega}{c}[|\underline{r}_o^{in}-\underline{r}'|+\phi_1(\underline{r}_o^{in})-\rho_{A,B}(\underline{r}'')+\rho_o^{in}]\}}{\sqrt{2}|\rho_{A,B}(\underline{r}'')||\underline{r}_o^{in}-\underline{r}'|}\,\tilde{s}(\underline{r}',\omega). \quad \text{(II-17)}$$

Figure II.4 serves to illustrate the results obtained thus far. Sources in the neighborhood of $\underline{r}'$ give rise to a field $\xi_o(\underline{r}^{in},t)$ for points $\underline{r}^{in}$ just beyond the lens. Neglecting diffraction and abberations and assuming sufficiently isotropic sources, spherical surfaces of equal ξ_o, or wavefronts, are found centered on the image $\underline{r}_c'$ of $\underline{r}'$. The field is resolved into orthogonal polarization components with amplitudes ξ_A and ξ_B, and the images generated by the interferometer are followed in their porpagation to points $\underline{r}''$ in the aperture immediately in front of the analyzer. Equivalently, the inverse of the

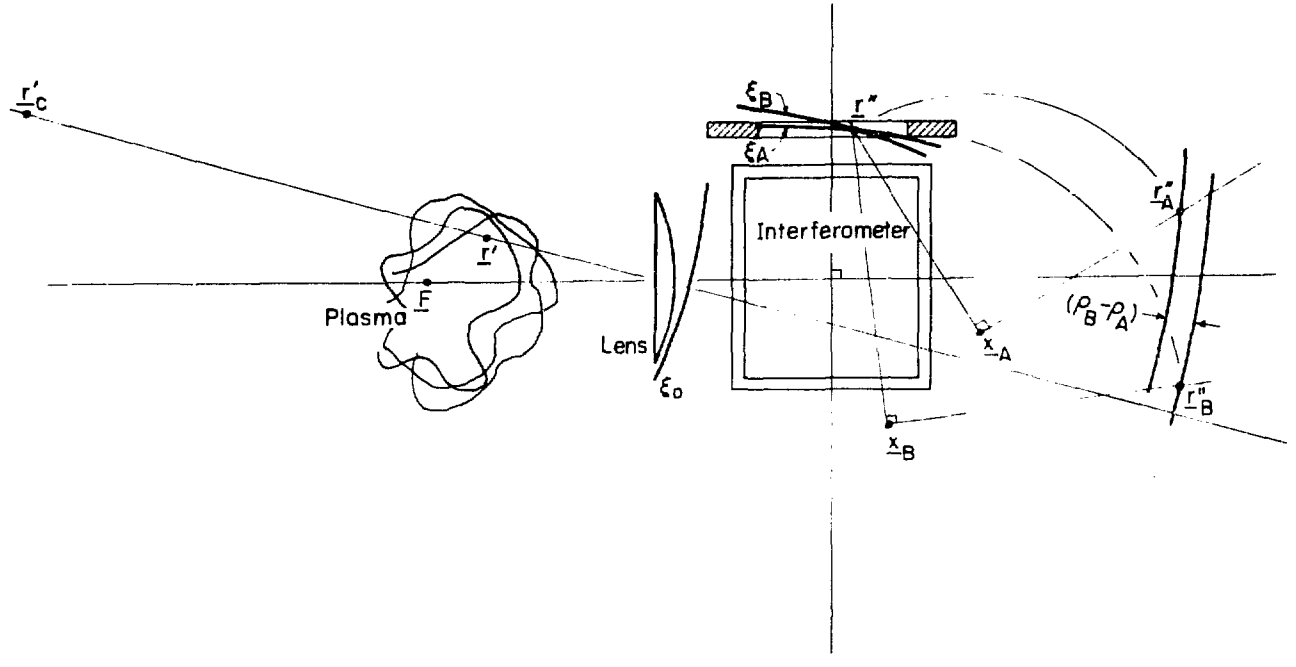

XBL 802-4663

Figure II.4 Determination of fields ξ_A and ξ_B reaching point $\underline{r}''$. Spherical wavefronts centered at the image point $\underline{r}'_c$ are transformed by the two rotations representing the interferometer into wavefronts for beams A and B, which then propagate directly to the aperture. The same result is obtained by finding the points $\underline{r}''_A$ and $\underline{r}''_B$ which are transformed by the corresponding rotations into $\underline{r}''$, and following the propagation of the field directly to these two points. The field reaching $\underline{r}''_A$ is equivalent to ξ_A, and that reaching $\underline{r}''_B$ to ξ_B.

transformations representing the interferometer are applied to $\underline{r}''$, producing pairs of points $\underline{r}''_A$ and $\underline{r}''_B$ in the path of the input wavefront, and the two components ξ_A and ξ_B are obtained from the propagation of the input field to each of these points.

Comparing Eq. (II-1) and (II-17) shows

$$\phi_{A,B}(\underline{r}'',\underline{r}',\omega) = \frac{|\rho_o^{in}|\exp\{i\frac{\omega}{c}[|\underline{r}_o^{in}-\underline{r}'|+\phi_1(\underline{r}_o^{in})-\rho_{A,B}(\underline{r}'')+\rho_o^{in}]\}}{\sqrt{2}|\rho_{A,B}(\underline{r}'')||\underline{r}_o^{in}-\underline{r}'|}. \quad \text{(II-18)}$$

Therefore, ϕ_B is expressed simply in terms of ϕ_A:

$$\phi_B(\underline{r}'',\underline{r}',\omega) = \left|\frac{\rho_A(\underline{r}'')}{\rho_B(\underline{r}'')}\right| \exp\{i\frac{\omega}{c}[\rho_A(\underline{r}'') - \rho_B(\underline{r}'')]\}\phi_A(\underline{r}'',\underline{r}',\omega). \quad \text{(II-19)}$$

If the source density $s(\underline{r}',t)$ represents sources emitting nearly monochromatic light at a frequency ω_o (wavenumber ω_o/c) with a linewidth $\Delta\omega$, then experimentally the light may be resolved, and changes in intensity with time over periods long compared with $\Delta\omega^{-1}$ may be observed. Conceptually, an approximation to the spectrum is obtained within a finite period τ ($t_o \leq t \leq t_o+\tau$), and variations over longer time intervals may be observed as time variations in the approximate spectra. Alternatively, a filter or spectrometer of finite resolution $\delta\omega \gtrsim \Delta\omega$ passes the light from the sources and responds to time variation slower than $\delta\omega^{-1}$. This situation is represented by introducing a time-dependent spectrum $\tilde{s}(\underline{r}',\omega;t)$ and a response function $f(\omega)$ giving the frequency resolution of the spectrometer or other light-selecting device in the system.

Assuming the points $\underline{r}''$ are sufficiently close to the analyzer which resolves the light resulting from the superposition of the "A" and "B" polarization components into the intermediate components "1" and "2," the intensities of the light received by the two detectors

due to sources near $\underline{r}'$ are given by an integral over the analyzer aperture a of the spectral density,

$$I_{1,2}(t;\underline{r}') = \int_a d^2\underline{r}'' \int_0^\infty \frac{d\omega}{2\pi}|f(\omega)|^2 \cdot \tfrac{1}{2}|\phi_A(\underline{r}'',\omega;\underline{r}')\tilde{s}(\underline{r}',\omega;t) \pm \phi_B(\underline{r}'',\omega;\underline{r}')\tilde{s}(\underline{r}',\omega;t)|^2. \quad \text{(II-20)}$$

In this equation, Eqs. (II-1) and (II-2) are used, and the response function and slow time dependence discussed above are included. The retardation is assumed negligible on this time scale.

For a distribution of incoherent sources, the total intensities are obtained by summing the individual intensities from the different points $\underline{r}'$. If the sources were coherent, it would be necessary to first sum the amplitudes and then obtain the intensities so that interference effects between sources would be included. In the present case, the only interference effects are between the two beams "A" and "B" from each individual source. The difference in intensities, which is the signal to be observed, is then obtained by:

$$Y(t) = \int d^3\underline{r}' I_1(t,\underline{r}') - \int d^3\underline{r}' I_2(t;\underline{r})$$

$$= \int d^3\underline{r}' \int_0^\infty \frac{d\omega}{\pi}|f(\omega)|^2 \int_a d^2\underline{r}'' \cdot \mathrm{Re}[\phi_A^*(\underline{r}'',\omega;\underline{r}')\tilde{s}^*(\underline{r}',\omega;t)\phi_B(\underline{r}'',\omega;\underline{r}')\tilde{s}(\underline{r}',\omega;t)]. \quad \text{(II-21)}$$

Rostler also fomulates this as

$$Y(t) = \int d^3\underline{r}' \int d\omega\ |f(\omega)|^2 T(\underline{r}',\omega) \mathcal{S}(\omega;\underline{r}',t), \quad \text{(II-22)}$$

where

$$T(\underline{r}',\omega) = \mathrm{Re}\,\frac{1}{\pi}\int_a d^2\underline{r}'' \phi_A^*(\underline{r}'',\omega;\underline{r}')\phi_B(\underline{r}'',\omega;\underline{r}'), \quad \text{(II-23)}$$

and Eq. (II-3) has been employed. The transmission function $T(\underline{r}',\omega)$ for the system represents the difference in visibility for the two

detectors of sources with frequency ω located near $\underline{r}'$; and thus T may be negative.

For the interferometer of this experiment, Eqs. (II-18) and (II-19) yield for the transmission function [Eq. (II-23)]

$$T(\underline{r}',\omega) =$$

$$\mathrm{Re}\,\frac{1}{\pi}\int_{a} d^2r'' \left|\frac{\rho_A(\underline{r}'')}{\rho_B(\underline{r}'')}\right| \exp\{i\,\tfrac{\omega}{c}[\rho_A(\underline{r}'')-\rho_B(\underline{r}'')]\}\cdot|\phi_A(\underline{r}'',\omega,\underline{r}')|^2$$

$$= \mathrm{Re}\,\frac{1}{\pi}\int_{a} d^2r'' \left|\frac{\rho_A(\underline{r}'')}{\rho_B(\underline{r}'')}\right| \exp\{i\,\tfrac{\omega}{c}[\rho_A(\underline{r}'')-\rho_B(\underline{r}'')]\}\frac{(\rho_o^{in})^2}{2\rho_A(\underline{r}'')^2|\underline{r}_o^{in}-\underline{r}'|^2}$$

$$= \mathrm{Re}\,\frac{1}{\pi}\int_{a} d^2r'' \frac{\rho_o^{(in)2}\exp\{i\,\frac{\omega}{c}\,[\rho_A(\underline{r}'')-\rho_B(\underline{r}'')]\}}{|2\rho_A(\underline{r}'')\rho_B(\underline{r}'')||\underline{r}_o^{in}-\underline{r}'|^2}. \qquad \text{(II-24)}$$

The basic system Rostler considers for TBS is of the type shown in Fig. II.5 (Rostler's Fig. C-4). The calcite rhomb may be treated as an interferometer in which a pair of translations $\underline{z}_A^{-1}$ and $\underline{z}_B^{-1}$ are substituted for the rotations R_A^{-1} and R_B^{-1}

$$Z_{A,B}^{-1}\,\underline{r}'' = \underline{r}'' + \Delta\underline{r}_{A,B},$$

and delays τ_A and τ_B due to refraction by the rhomb are added to the retardations $(1/c)\rho_A(\underline{r}'')$ and $(1/c)\rho_B(\underline{r}'')$ appearing in the exponential of Eq. (II-24). Since much of this difference between the interferometer model and Rostler's birefringent system example is compensated by the difference necessary in the aperture placement, the two systems may be compared in most respects by applying the model for the interferometer system developed here.

It is helpful to temporarily view the transmission function as depending upon $\underline{r}_c'$ through the object-image relation of $\underline{r}'$ and $\underline{r}_c'$, rather than upon $\underline{r}'$.

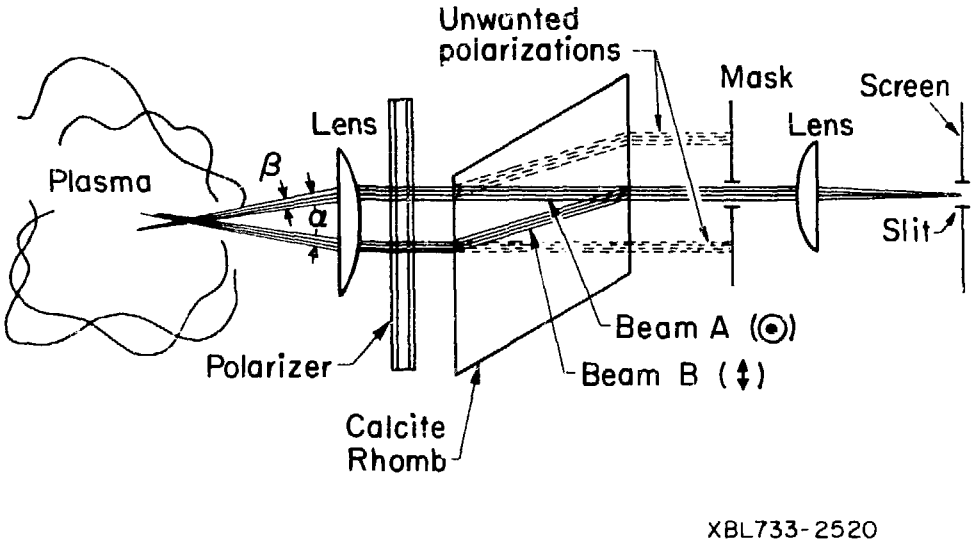

Figure II.5 Two-beam system of the type Rostler considered. (From Ref. 1.)

For points $\underline{r}'$ sufficiently near the focal plane of the lens, the image points $\underline{r}_c'$ are very far from the lens, and the integrand of Eq. (II-24) may be taken as constant. Points $\underline{r}'$ farther from the focal plane of the lens are equivalent to points $\underline{r}_c'$ axially closer to the lens. When $\underline{r}_c'$ is too close to $\underline{r}_A^{in}$ and $\underline{r}_B^{in}$, the relative path difference $\rho_A(\underline{r}'')-\rho_B(\underline{r}'')$ can vary signficantly across the aperture and even the amplitudes, proportional to $\rho_A(\underline{r}'')^{-1}$ and $\rho_B(\underline{r}'')^{-1}$ [see Eq. (II-15)] may vary substantially.

In general, Eq. (II-24) which may be rewritten as

$$T(\underline{r}_c',\omega) = \frac{1}{2\pi}\frac{\rho_o^{(in)2}}{|\underline{r}_o^{in}-\underline{r}'(\underline{r}_c')|^2}\,\mathrm{Re}\int_a d^2r''\,\frac{\exp\{i\frac{\omega}{c}[\rho_A(\underline{r}'')-\rho_B(\underline{r}'')]\}}{|\rho_A(\underline{r}'')\rho_B(\underline{r}'')|}$$

$$= \frac{1}{2\pi}\frac{\rho_o^{(in)2}}{|\underline{r}_o^{in}-\underline{r}'(\underline{r}_c')|^2}\int_a d^2r''\,\frac{\cos\frac{\omega}{c}[\rho_A(\underline{r}'')-\rho_B(\underline{r}'')]}{|\rho_A(\underline{r}'')\rho_B(\underline{r}'')|} \qquad \text{(II-25)}$$

for the interferometer system, is difficult to evaluate. However, it is apparent that when the argument of the cosine varies by 2π or more across the aperture, the transmission function is reduced compared to the amplitude for points $\underline{r}'$ near the focus of the lens (approximated by assuming the integrand constant).

As long as $\rho_A(\underline{r}'')$ and $\rho_B(\underline{r}'')$ both have the same sign we may assume they are positive for the purpose of evaluating the integral in Eq. (II-25):

$$\int_a d^2r''\,\frac{\cos\frac{\omega}{c}[\rho_A(\underline{r}'')-\rho_B(\underline{r}'')]}{|\rho_A(\underline{r}'')\rho_B(\underline{r}'')|} = \int_a d^2r''\,\frac{\cos\frac{\omega}{c}(|R_A^{-1}\underline{r}''-\underline{r}_c'|-|R_B^{-1}\underline{r}''-\underline{r}_c'|)}{|R_A^{-1}\underline{r}''-\underline{r}_c'|\cdot|R_B^{-1}\underline{r}''-\underline{r}_c'|}$$

$$= \int_a d^2r''\,\frac{\cos\frac{\omega}{c}(|\underline{r}''-\underline{r}_c^A|-|\underline{r}''-\underline{r}_c^B|)}{|\underline{r}''-\underline{r}_c^A|\cdot|\underline{r}''-\underline{r}_c^B|}, \qquad \text{(II-26)}$$

where $\underline{r}_c^{A,B} = R_{A,B}\underline{r}_c$, and we have used the invariance of lengths under the transformations R_A and R_B. Figure II.6 illustrates the evaluation of the argument of the cosine in Eq. (II-26). The procedure is the same as for finding the phase difference in an interference calculation for two point sources. One can ascertain from the interference pattern sketched in dashed lines as an example (the interference pattern represents surfaces of constant phase difference equal to integral multiples of 2π), that if the image points $\underline{r}_c^A$ and $\underline{r}_c^B$ are within a certain distance in front of the aperture (or behind in the case of converging light entering the aperture--the sketch in Fig. II.6 may still be viewed as representative, if perhaps upside-down in this case), the cosine in the integrand of Eq. (II-26) begins to vary over the range of integration sufficiently rapidly to average the transmission function to a small value.

Because ω/c in the cosine is large [this is the short-wavelength approximation--ω/c is determined by the spectral characteristics of the sources $\tilde{s}(\underline{r}',\omega;t)$ and by the response $f(\omega)$ for the system], the distance in front of the aperture within which the transmission function is reduced may still be large enough to use an expansion. Letting

$$\begin{aligned} \underline{r}_c^o &= \tfrac{1}{2}(\underline{r}_c^A + \underline{r}_c^B) \\ \underline{r}_{AB} &= \tfrac{1}{2}(\underline{r}_c^A - \underline{r}_c^B), \end{aligned} \tag{II-27}$$

we find

$$|\underline{r}'' - \underline{r}_c^A| - |\underline{r}'' - \underline{r}_c^B| \simeq \frac{2(\underline{r}'' - \underline{r}_c^o)}{|\underline{r}'' - \underline{r}_c^o|} \cdot \underline{r}_{AB} \tag{II-28}$$

and

$$|\underline{r}''-\underline{r}_c^A| \cdot |\underline{r}''-\underline{r}_c^B| \simeq |\underline{r}''-\underline{r}_c^o|^2 \left\{ 1 - \left[\frac{(\underline{r}''-\underline{r}_c^o)\cdot\underline{r}_{AB}}{|\underline{r}''-\underline{r}_c^o|^2} \right]^2 \right\} . \tag{II-29}$$

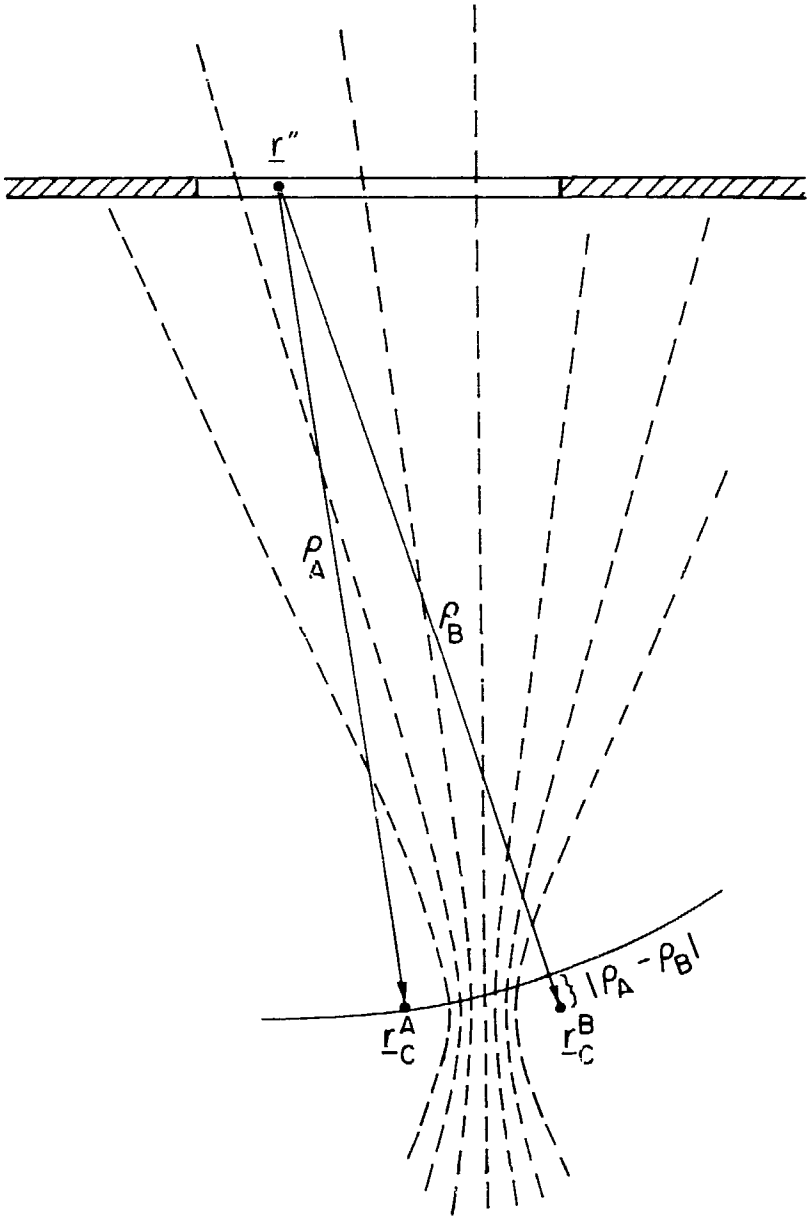

XBL802-4670

Figure II.6 Construction showing evaluation of quantities in integrand of Eq. (II-26). The argument of the cosine is the same phase difference factor which would be involved in a two point source interference pattern such as the one represented by the dashed hyperbolas. The more fringes there are across the aperture, the more rapidly varying is the cosine factor in the integrand.

Thus to first order in $|\underline{r}_{AB}|/|\underline{r}'' - \underline{r}_c^o|$, Eq. (II-26) becomes

$$\int_a d^2r'' \frac{\cos \frac{\omega}{c}[\rho_A(\underline{r}'')-\rho_B(\underline{r}'')]}{\rho_A(\underline{r}'')\rho_B(\underline{r}'')} = \int_a d^2r'' \frac{\cos \frac{2\omega}{c} \frac{(\underline{r}''-\underline{r}_c^o)\cdot\underline{r}_{AB}}{|\underline{r}''-\underline{r}_c^o|}}{|\underline{r}'' - \underline{r}_c^o|^2}$$

$$= \int_a d^2v \frac{\cos[2 \frac{\omega}{c} \hat{v}\cdot(\underline{r}_c^A-\underline{r}_c^B)]}{v^2} \qquad \text{(II-30)}$$

where

$$\underline{v} = \underline{r}'' - \underline{r}_c^o$$
$$\hat{v} = \underline{v}/v. \qquad \text{(II-31)}$$

Writing $\underline{k}(\omega) = (\omega/c)\hat{v}$, we see that the argument of the cosine does indeed represent a phase difference in an interference calculation. The approximation made in going from Eq. (II-26) to Eq. (II-30) amounts to equating the directions from the two points $\underline{r}_c^A$ and $\underline{r}_c^B$ to $\underline{r}''$ to the direction from the midpoint $\underline{r}_c^o$ to $\underline{r}''$ as an average (and using the distance between the latter two points in the denominator of the integrand). This approximation may be quite adequate while the average direction varies sufficiently at different points across the aperture for the argument to vary by much more than 2π.

As an example, suppose the aperture is rectangular with dimensions L×W, and the side L is perpendicular to the displacement vector $\underline{r}_{AB} = x_{AB}\hat{x} + z_{AB}\hat{z} = (x_{AB}, 0, z_{AB})$. If the center of the aperture is at (x_o, y_o, z_o), and the origin is at $\underline{r}_c^o$, we can write the integral (Eq. (II-30) as

$$\int_a d^2r'' \frac{\cos[(2\frac{\omega}{c}\frac{\underline{r}''}{r''}\cdot\underline{r}_{AB})]}{(\underline{r}'')^2} =$$

$$\int_{y_o-(L/2)}^{y_o+(L/2)} dy \int_{x_o+(W/2)}^{x_o+(W/2)} dx \frac{\cos\left[2\frac{\omega}{c}\frac{x_{AB}x + z_{AB}z_o}{(x^2+y^2+z_o^2)^{\frac{1}{2}}}\right]}{x^2+y^2+z_o^2} \quad (II-32)$$

Making the substitution

$$u = \frac{x}{(x^2+y^2+z_o^2)^{\frac{1}{2}}} \quad (II-33)$$

transforms the x integration to:

$$I = \int_{x_o-(W/2)}^{x_o+(W/2)} dx \frac{\cos\left[2\frac{\omega}{c}\frac{x_{AB}x + z_{AB}z_o}{(x^2+y^2+z_o^2)^{\frac{1}{2}}}\right]}{x^2+y^2+z_o^2}$$

$$= \frac{1}{(y^2+z_o^2)^{\frac{1}{2}}} \int_{u_1}^{u_2} du \frac{\cos\left\{2\frac{\omega}{c}\left[x_{AB}u + \frac{z_{AB}z_o}{(y^2+z_o^2)^{\frac{1}{2}}}(1-u^2)^{\frac{1}{2}}\right]\right\}}{(1-u^2)^{\frac{1}{2}}} \quad (II-34)$$

where

$$u_{2,1} = \frac{x_o \pm (W/2)}{[(x_o \pm \frac{W}{2})^2 + y^2 + z_o^2]^{\frac{1}{2}}} . \quad (II-35)$$

If we assume a properly constructed TBS system has the aperture centered on the axis (that is, the aperture midpoint is halfway between the two images of the axis of the first lens formed by the interferometer), then

$$u_o = \frac{x_o}{(x_o^2+y_o^2+z_o^2)^{\frac{1}{2}}} \quad (II-36)$$

is of the order of the sine of the angle the x coordinate of the

image point $\underline{r}'_c$ makes with the axis at the center of the lens, provided the optical path between the lens and the aperture is not long enough to be important. The angle the image makes is also the angle the object point $\underline{r}'$ makes with the center (actually it is the appropriate principal point in both cases) of the lens. Generally, it is necessary to limit this angle and also the range of angles (and hence the range of u) because of such considerations as the acceptable field of view of the interferometer (see Appendix A and the discussion of the optics in Chapter IV.B.1). Thus we may take $u^2 \ll 1$ and find that if $z_{AB} \lesssim x_{AB}$, then the second term in the argument of the cosine [Eq. (II-34)] varies much less than the first. The quantity $(1 - u^2)^{\frac{1}{2}}$ in this term and in the denominator of the integrand varies slowly between $(1 - u_1^2)$ and $(1 - u_2^2)$ or between the smaller of these two values and unity. We can then estimate the integral in Eq. (II-34) as

$$I \approx \frac{c\{\sin [\frac{2\omega}{c} x_{AB}(u_2+Z)] - \sin [\frac{2\omega}{c} x_{AB}(u_1+Z)]\}}{2\omega x_{AB}(y_o^2+z_o^2)^{\frac{1}{2}}(1-u_b^2)^{\frac{1}{2}}}$$

$$= \frac{c \cos [\frac{2\omega}{c} x_{AB}(u_a+Z)] \sin [\frac{\omega}{c} x_{AB}(u_2-u_1)]}{\omega x_{AB}(y^2+z_o^2)^{\frac{1}{2}}(1-u_b^2)^{\frac{1}{2}}} \qquad \text{(II-37)}$$

where

$$u_a = (u_1 + u_2)/2$$

$$Z = \frac{z_{AB} z_o}{z_{AB}(y^2 + z_o^2)^{\frac{1}{2}}} (1 - u_b^2)^{\frac{1}{2}}, \qquad \text{(II-38)}$$

and u_b is chosen from the interval u_1 to u_2 to give an appropriate value between the minimum and maximum values assumed by $(1 - u^2)^{\frac{1}{2}}$.

The integral of Eq. (II-34), estimated by Eq. (II-37), must be used in Eqs. (II-32) and (II-25) to obtain the approximate transmission function for points $\underline{r}_c^A$ and $\underline{r}_c^B$ sufficiently far from the aperture. We see, however, that Eq. (II-37) is of the form

$$I = \left\{ \frac{\sin\left[\frac{\omega}{c} x_{AB}(u_2-u_1)\right]}{\left[\frac{\omega}{c} x_{AB}(u_2-u_1)\right]} \right\} (u_2-u_1) \frac{\cos\left[\frac{\omega}{c} x_{AB}(u_a+z)\right]}{(y^2+z_o^2)^{\frac{1}{2}}(1-u_b^2)^{\frac{1}{2}}} \quad . \quad \text{(II-39)}$$

The first factor shows the behavior interpreted earlier as an averaging away of the transmission function. Varying as (sinX)/X (where X is one-half the change in phase difference across the aperture for the two beams), this factor represents a decreasing amplitude for the transmission function for image points not sufficiently far from the aperture, or for points in the plasma sufficiently far from the focal plane of the lens.

The rest of Eq. (II-39) can be interpreted as depending approximately on the width of the aperture, the distance $[(y^2+z_o^2)^{\frac{1}{2}}]$, and on the oscillatory weighting factor varying with the angle from the aperture to this point through u_a. From Eq. (II-33),

$$\frac{u}{(1-u^2)^{\frac{1}{2}}} = \frac{x}{(y^2+z_o^2)^{\frac{1}{2}}} \qquad \text{(II-40)}$$

is needed to show that

$$\frac{u_1-u_2}{(1-u_b^2)^{\frac{1}{2}}} \approx \frac{W}{(y^2+z_o^2)^{\frac{1}{2}}} \quad . \qquad \text{(II-41)}$$

This interpretation illustrates that it is reasonable to factor the integral as in Eq. (II-39).

To complete the analysis of the transmission function, it now suffices to simplify to a more specific case of a properly adjusted interferometer and points $\underline{r}'$ confined only to the vicinity of the

focal plane of the lens. This latter simplification is suggested by the effect of the first factor in Eq. (II-39), which approaches unity for these points. For a properly adjusted interferometer we will assume the separation between $\underline{r}_c^A$ and $\underline{r}_c^B$ is perpendicular to the axis, i.e., that $z_{AB} = 0$. With these simplifications Eq. (II-34) becomes

$$I = \frac{1}{(y^2+z_o^2)^{\frac{1}{2}}} \int_{u_1}^{u_2} du \, \frac{\cos \frac{2\omega}{c} x_{AB} u}{(1-u^2)^{\frac{1}{2}}}$$

$$\approx \frac{(x_o^2+y_o^2+z_o^2)^{\frac{1}{2}}}{y_o^2+z_o^2} (u_2-u_1) \cos \frac{2\omega}{c} x_{AB} u_o, \qquad \text{(II-42)}$$

and the integral over y is

$$\int_{y_o-(L/2)}^{y_o+(L/2)} I \, dy \approx \frac{LW}{y_o^2+z_o^2} \cos \frac{2\omega}{c} \frac{x_{AB} x_o}{(x_o^2+y_o^2+z_o^2)^{\frac{1}{2}}} \qquad \text{(II-43)}$$

The coordinates (x_o, y_o, z_o) are those of the center of the aperture relative to $\underline{r}_c^o$. However, since Eq. (II-43) is even in the coordinates, they might must as well be those of $\underline{r}_c^o$ relative to the center of the aperture. From Eq. (II-25) the transmission function becomes

$T(x_o, y_o z_o) =$

$$\frac{1}{2\pi} \frac{(\rho_o^{in})^2}{|r_o^{in} - \underline{r}'(x_o, y_o, z_o)|^2} \frac{LW}{y_o^2+z_o^2} \cos \frac{2\omega}{c} \frac{x_{AB} x_o}{(x_o^2+y_o^2+z_o^2)^{\frac{1}{2}}} \qquad \text{(II-44)}$$

or

$$T(\underline{r}', \omega) = \frac{LW}{2\pi f_1^2} \cos \frac{2\omega}{c} x_{AB} \frac{x_o}{z_o}, \qquad \text{(II-45)}$$

assuming small angles and neglecting the path difference between the lens and the aperture compared with the distance to $\underline{r}_c'$ (ρ_o^{in}). As in

Fig. II.1, f_1 is the focal length of the lens. If x' is the coordinate of $\underline{r}'$ corresponding to x_o, we can substitute x'/f_1 for x_o/z_o in the cosine. We rewrite Eq. (II-45) as

$$T(\underline{r}',\omega) = \frac{LW}{2\pi f_1^2} \cos \frac{\omega}{c} \left(\frac{2x_{AB}}{f_1}\right)x'. \qquad \text{(II-46)}$$

If this simplified version of the transmission function is substituted into Eq. (II-22) for the signal Y(t), we see we have

$$Y(t) = \frac{LW}{2\pi f_1^2} \int d^3r' \int_{-\infty}^{\infty} d\omega \, |f(\omega)|^2 \cos \frac{\omega}{c} \left(\frac{2x_{AB}}{f_1}\right)x' \mathcal{S}(\omega;\underline{r}',t). \qquad \text{(II-47)}$$

Assuming the source spectral density $\mathcal{S}$ and the response function f confine the light accepted to a single spectral line of width $\Delta\omega$ at ω_o (as discussed above), the ω integration may be dropped for the substitutions $\omega \to \omega_o$ and $d\omega \to \Delta\omega$ leaving

$$Y(t) = \frac{LW}{2\omega f_1^2} |f(\omega_o)|^2 \int d^3r' \cos \left[\frac{\omega_o}{c} \left(\frac{2x_{AB}}{f_1}\right)x'\right] \mathcal{S}(\omega_o;r',t). \qquad \text{(II-48)}$$

Were the range of the $\underline{r}'$ integration infinite, it would be simply the real part of the Fourier transformation of $\mathcal{S}$, evaluated for the wavevector:

$$\underline{k}_\Delta \equiv \hat{x}' \frac{\omega_o}{c} \frac{2x_{AB}}{f_1} . \qquad \text{(II-49)}$$

In fact, the integral must be limited to a finite region because of the approximations made: $\underline{r}'$ is near the focal plane and within a small angle of the axis of the lens, measured from the principal point. The limitation to points near the focal plane can be relaxed somewhat if Eq. (II-39) is used, reinstating the amplitude factor that decays for points sufficiently far from the focal plane (image points sufficiently

close to the aperture). At any rate, we can write Eq. (II-48) as the real part of the Fourier transform of $\mathcal{J}(\omega;\underline{r}',t)$ multiplied by a localizing function $g(\underline{r}')$ which goes to zero outside of the region to be integrated over. The result is given by the convolution of the Fourier transform of $\mathcal{J}$ along with that of g:

$$g(\underline{k}) = \int d^3r' e^{i\underline{k}\cdot\underline{r}'} g(r') \tag{II-50}$$

$$Y(t) = \mathrm{Re}\left[\frac{LW\Delta\omega}{2\pi f_1^2} |f(\omega_o)|^2 \left(\frac{1}{2\pi}\right)^3 \tilde{g}(\underline{k}_\Delta)^* \mathcal{J}(\omega;\underline{k}_\Delta,t)\right], \tag{II-51}$$

where

$$u(\underline{k})^* v(\underline{k}) = \int d^3\nu\ u(\nu)v(\underline{k} - \underline{\nu}). \tag{II-52}$$

For example, if $g(\underline{r}')$ were a Gaussian of width r_o,

$$g(\underline{r}') = \exp(-r^2/2r_o^2), \tag{II-53}$$

we find

$$\tilde{g}(\underline{k}) = (2\pi r_o^2)^{3/2} \exp(-\tfrac{1}{2}k^2 r_o^2) \tag{II-54}$$

is a Gaussian of width $1/r_o$. Roughly speaking, $\mathcal{J}(\omega;\underline{k}_\Delta,t)$ is smoothed by averaging together values for $\underline{k}$ within about $\delta k = 1/r_o$ of $\underline{k}_\Delta$.

We also find that it matters little what the behavior of $\mathcal{J}(\omega;r',t)$ is for distances from the center of $g(\underline{r}')$ (presumably the focus $\underline{F}$ of the lens) large compared with r_o. As with the Fourier transform in time, we could write this as

$$Y(\underline{F},t) = \frac{LW}{2\pi} |f(\omega_o)|^2 \mathcal{J}(\underline{k}_\Delta,\omega_o;\underline{F},t). \tag{II-55}$$

With a little more detailed discussion this time, the argument is the same as that which led to the introduction of the time-dependent spectrum; that is, an experimentally obtained spectrum must necessarily be an approximation to the mathematical Fourier transform, due to the finite time (and spatial) range of measurable information. It may be

viewed as a time- (and position) dependent spectrum with a finite frequency (and wavenumber) resolution.

As outlined at the beginning of this section, we have shown that TBS is sensitive to a spatial component of the spectral density of the source distribution, namely the $T(\underline{r}',\omega)$ component of $\mathcal{S}(\omega;\underline{r}'t)$. Also, we have found that for the type of TBS system used in this experiment, the component selected is $\mathcal{S}(\underline{k}_{\ell},\omega_o;\underline{F},t)$. Finally, we have found that the measurement is local in space as well as in time, measured on a sufficiently large scale.

This last point, spatial resolution, requires emphasis. As Rostler points out[6] a conventional spectroscopic measurement may provide a localized measurement transverse to the line of sight, but sources along the line of sight are not distinguished. Here we are discussing an additional localization along the line of sight (normal to the focal plane). Originally, Rostler proposed that this resolution would be obtained from the intersection of two distinct beams, as illustrated for the system in Fig. II.5 by the detail in Fig. II.7 [Rostler's Fig. C-5 (b)]. Although the transverse resolution (ϕ_A, ϕ_B are zero outside the transverse limits of beams A,B) obtainable in conventional spectroscopy is not included explicitly in the TBS derivation presented here, we can see how it leads to a line of sight resolution, or locaization of the transmission function T to the region of intersection of the two beams. Only in this common source volume, where ϕ_A and ϕ_B are both nonzero, is T nonzero.

The system analyzed in this chapter is different. The analysis presented allows for overlapping beams as shown in Fig. II.8--yet the form of Eq. (II-39) shows spatial resolution is still possible.

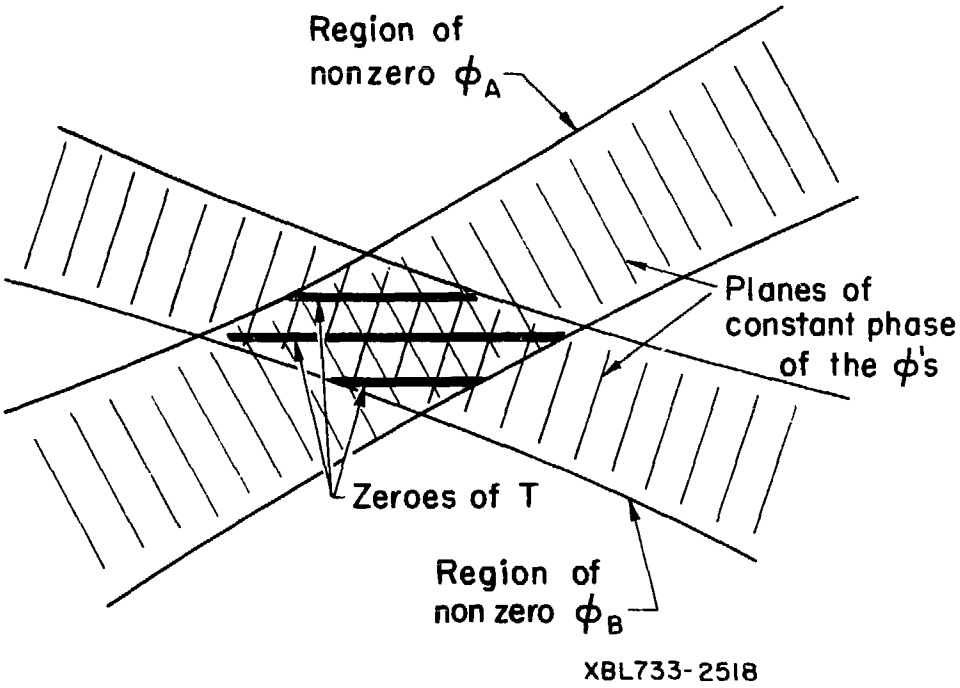

Figure II.7 Region where two non-overlapping beams cross, providing spatial resolution as Rostler orginally proposed. The transmission function T is obtained from the product of the two beams' transfer functions ϕ_A and ϕ_B. Thus, T is nonzero only where the beams intersect.

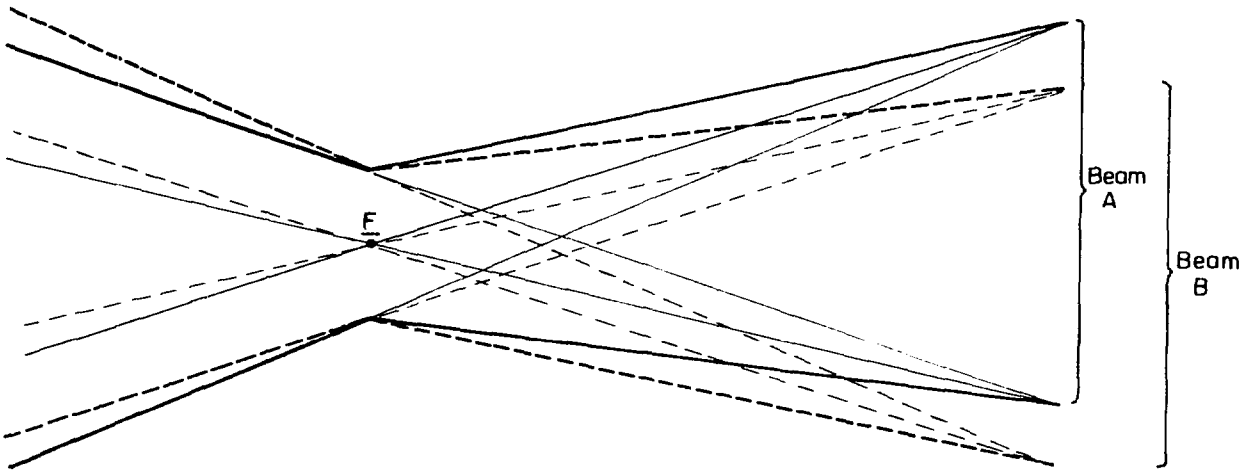

XBL 803-4916

Figure II.8 Overlapping beam situation analyzed in this chapter. In this case TBS can still achieve spatial resolution by a different mechanism than that illustrated in Fig. II.7. The solid and dashed lines delineate outlines and some rays associated with beams A and B respectively.

We can see this most easily when the scale of localization is small compared with the focal length of the lens. Using the lens formula, we may write

$$\Delta z' \Delta z'_c = f_1^2, \tag{II-56}$$

where $\Delta z'$ is the distance of the point $\underline{r}'$ behind the left focal plane of the lens in Fig. II.1 (b), and $\Delta z'_c$ is similarly the distance of the image point $\underline{r}'_c$ beyond the other focal plane (not shown). In Eq. (II-39) we are interested in the quantity $u_2 - u_1$, (to the accuracy of the small angle approximations used in this chapter) the angle subtended by the width W of the aperture at the point $\underline{r}_c^o$ derived from $\underline{r}'_c$. That angle is approximately

$$\frac{W}{\Delta z} \approx \frac{W}{\Delta z'_c}, \tag{II-57}$$

where Δz is the distance from $\underline{r}_c^o$ to the plane of the aperture, which we approximate by the distance of $\underline{r}'_c$ to the right focal plane of the lens, neglecting the path difference through the system between the two planes compared with the distance $\Delta z'_c$. The factor responsible for spatial resolution in Eq. (II-39) becomes

$$\frac{\sin[\frac{\omega}{c} x_{AB}(u_2 - u_1)]}{\frac{\omega}{c} x_{AB}(u_2 - u_1)} = \frac{\sin(\frac{\omega}{c} x_{AB} \frac{W}{f_1^2} \Delta z')}{\frac{\omega}{c} x_{AB} \frac{W}{f_1^2} \Delta z'}$$

$$= \frac{\sin(\frac{k_\Delta W}{2f_1} \Delta z')}{\frac{k_\Delta W}{2f_1} \Delta z'}, \tag{II-58}$$

using Eqs. (II-56) and (II-57), and then Eq. (II-49) (where we anticipate that ω will be limited to $\approx \omega_o$).

From Eq. (II-58) we can conclude that the distance $|\Delta z'|$ of the sources from the focal plane is limited to order

$$\Delta z_o = \frac{2\pi f_1}{k_\Delta W}$$

$$= \frac{\lambda_\Delta}{w} f_1, \qquad \text{(II-59)}$$

where $\lambda_\Delta = 2\pi/k_\Delta$ is the wavelength selected by the TBS system. If $\lambda_\Delta << W$, Eq. (II-58) is an adequate estimate of the spatial resolution. The factor in Eq. (II-58) could then be included in Eq. (II-46) without exceeding the limits of the approximations used.

The analysis presented in this section shows that TBS may be used to make a local measurement of the time dependence of a spatial Fourier component of the distribution of incoherent light sources in a plasma. In particular, Rostler's analysis has been extended to include overlapping beams, and it has been shown that a localized common source volume is unnecessary in obtaining spatial resolution. The multiple-beam spectroscopy system proposed by Rostler[7] to collect more light while maintaining pairs of beams with well-defined common source volumes can be replaced by a simpler system collecting still more light.

B. Plasma Phenomena Relevant to TBS

In the preceding section, the response of a TBS system to fluctuations in the light source distributions is explained. We now discuss how plasma waves may be detected through their influence on the light source distribution. This discussion begins with a derivation of the properties of an ion acoustic wave as an example appropriate to the experiment. Plasma fluctuations related to the detectable light source

distribution fluctuations are shown. In the second section, coupling between some types of plasma fluctuations and various light sources are considered.

I. Properties of Ion Acoustic Waves. The spontaneous fluctuations found in the positive column used in this experiment show a frequency range and dispersion relation resembling ion acoustic waves. Ion acoustic waves were predicted by Tonks and Langmuir.[8] A simplified derivation using kinetic theory is presented here assuming an infinite, homogeneous plasma with ions and electrons having Maxwellian velocity distributions of unequal temperature. Features of the electron and ion fluctuations important for a TBS measurement are shown. Ion acoustic waves are found to propagate with weak damping under conditions of high electron temperature relative to ions, appropriate to many low pressure discharge plasmas. Numerical analysis of a more complete dispersion relation appropriate to positive columns including collisions with neutrals through BGK terms, and the destabilizing effect of a relative drift between electrons and ions (due to the discharge current) are given by Ilić, et al.[9]

The Boltzmann equation with no collisions, or the Vlasov equation for the distribution function $f_s(\underline{x},\underline{v},t)$ of particles of species s is[10]

$$\frac{\partial f_s}{\partial t} + \underline{v}\cdot\nabla_{\underline{x}} f_s + \frac{e_s \underline{E}}{m_s}\cdot\nabla_{\underline{v}} f_s = 0, \qquad \text{(II-60)}$$

where

$$\nabla_{\underline{x}} = \sum_i \hat{x}_i \frac{\partial}{\partial x_i} \quad \text{and} \quad \nabla_{\underline{v}} = \sum_i \hat{v}_i \frac{\partial}{\partial v_i}$$

are the gradient operators with respect to position and velocity respectively. Assuming the distribution consists of a homogeneous, time-independent equilibrium distribution $f_{o,s}(\underline{v})$ plus a first order one-dimensional fluctuation $f_{1,s}(z,v_z,t)$--

$$f_s(\underline{x},\underline{v},t) = f_{o,s}(\underline{v}) + f_{1,s}(z,v_z,t) \qquad \text{(II-61)}$$

--and that the field is also a one-dimensional first-order fluctuation

$$\underline{E} = \hat{z}E_1(z,t), \qquad \text{(II-62)}$$

the Vlasov equation [Eq. (II-60)] may be linearized and reduced to a one-dimensional form:

$$\frac{\partial}{\partial t} f_{1,s}(z,v,t) + v \frac{\partial}{\partial z} f_{1,s}(z,v,t) + \frac{e_s n_o E_1(z,t)}{m_s} \frac{\partial}{\partial v} g_s(v) = 0. \qquad \text{(II-63)}$$

Here we have defined

$$n_o g_s(v_z) = \int_{-\infty}^{\infty} dv_x \int_{-\infty}^{\infty} dv_y f_{o,s}(\underline{v}), \qquad \text{(II-64)}$$

with

$$\int_{-\infty}^{\infty} g_s(v)\, dv = 1. \qquad \text{(II-65)}$$

(Where only one dimension is involved, the subscript of v_z is dropped.)

A dispersion relation for fluctuations in the form of electrostatic waves in the plasma may be obtained from the assumption of a harmonic spatial and time dependence of the fluctuation quantities,

$$f_{1,s} = f_{1,s}(v) \exp(ikz - i\omega t) \qquad \text{(II-66)}$$

and

$$E_1 = -\frac{\partial}{\partial z}\phi_1 = -ik(\phi_{ext} + \phi_e + \phi_i) \exp(ikz - i\omega t), \qquad \text{(II-67)}$$

and from Poisson's equation for the fields:

$$-k^2(\phi_{ext}+\phi_e+\phi_i) = -4\pi e\{n_{ext} + \int_{-\infty}^{\infty} dv[f_{1,i}(v) - f_{1,e}(v)]\} \qquad \text{(II-68)}$$

due to the external, electron, and ion charge densities respectively. In this electrostatic approximation, the dispersion relation for nor-

mal modes (zero external field) is obtained by solving the linearized Vlasov equation [Eq. (II-63)] and Poisson's equation [Eq. (II-68)] using Eqs. (II-66) and (II-67) with $\phi_{ext} = n_{ext} = 0$. We obtain

$$(-i\omega + ikv)f_{1,i} = + \frac{ikn_o e}{m_i} (\phi_e + \phi_i) \frac{\partial}{\partial v} g_i,$$

$$(-i\omega + ikv)f_{1,e} = - \frac{ikn_o e}{m_e} (\phi_e + \phi_i) \frac{\partial}{\partial v} g_e, \qquad \text{(II-69)}$$

$$k^2(\phi_e+\phi_i) =$$

$$4\pi n_o e^2(\phi_e+\phi_i) \int_{-\infty}^{\infty} dv\left[\frac{1}{m_i} \left(\frac{1}{-\frac{\omega}{k} + v}\right)\frac{\partial}{\partial v} g_i + \frac{1}{m_e} \left(\frac{1}{-\frac{\omega}{k} + v}\right)\frac{\partial}{\partial v} g_e\right],$$

or

$$k^2 = \int_{-\infty}^{\infty} dv\left[\frac{1}{v - (\omega/k)}\right] \frac{\partial}{\partial v} (\omega_i^2 g_i + \omega_e^2 g_e), \qquad \text{(II-70)}$$

where $\omega_{i,e}^2 = 4\pi ne^2/m_{i,e}$. This dispersion relation may also be written in terms of the plasma dielectric function:

$$\varepsilon(k,\omega) = 1 - \frac{\omega_e^2}{k^2} \int_{-\infty}^{\infty} dv \left[\frac{\partial g_e/\partial v}{v - \frac{\omega}{k}}\right] - \frac{\omega_i^2}{k^2} \int_{-\infty}^{\infty} \left[\frac{\partial g_i/\partial v}{v - \frac{\omega}{k}}\right] = 0. \qquad \text{(II-71)}$$

The ion acoustic wave is a normal mode of a plasma consisting of electrons and ions with Maxwellian velocity distributions,

$$g_{e,i} = \frac{1}{\sqrt{\pi}\, c_{e,i}} \exp\,(-v^2/c_{e,i}^2), \qquad \text{(II-72)}$$

with separate temperatures T_e and T_i for electrons and ions, where

$$c_{e,i}^2 = \frac{2k_B T_{e,i}}{m_{e,i}} \qquad \text{(II-73)}$$

and k_B is Boltzmann's constant. In this case the dielectric function may be expressed as[11]

$$\varepsilon(k,\omega) = 1 - \frac{\omega_e^2}{k^2 c_e^2} Z'\left(\frac{\omega}{kc_e}\right) - \frac{\omega_i^2}{k^2 c_i^2} Z'\left(\frac{\omega}{kc_i}\right), \qquad \text{(II-74)}$$

using the plasma dispersion function

$$Z(\zeta) = \frac{1}{\sqrt{\pi}} \int_{-\infty}^{\infty} \frac{\exp(-x^2)}{x - \zeta} \tag{II-75}$$

and its derivative Z', which are tabulated by Fried and Conte.[12]

Setting $\varepsilon = 0$ in Eq. (II-74) and choosing k as a real independent variable yields, in certain cases, a nearly real solution $\omega(k)$. If we let

$$\omega_r = \mathrm{Re}[\omega(k)]$$

and (II-76)

$$\gamma = \mathrm{Im}[\omega(k)],$$

then nearly real means $\gamma \ll \omega_r$, and the mode is weakly damped (growing) wave for $\gamma < 0$ ($\gamma > 0$) [see Eqs. (II-66) and (II-67)]. For ions much colder than electrons

$$T_i \ll T_e, \tag{II-77}$$

and where

$$m_e \ll m_i, \tag{II-78}$$

we can find a range of values such that

$$c_i \ll |\omega/k| \ll c_e, \tag{II-79}$$

for which

$$Z'(\zeta) = -2 - 2i\sqrt{\pi}\, \zeta \exp(-\zeta^2) \tag{II-80}$$

is the expansion to be used for small $|\zeta|$, while in the ion term the expansion for large $|\zeta|$

$$Z'(\zeta) = \frac{1}{\zeta^2} - 2i\sqrt{\pi}\, \zeta \exp(-\zeta^2) \tag{II-81}$$

applies for $\gamma < 0$. We then obtain from Eqs. (II-74), (II-80), and (II-81) with $\varepsilon = 0$ the approximate dispersion relation

$$1 + 2(\omega_i^2/k^2c_e^2) - (\omega_i^2/\omega_r^2) = 0, \tag{II-82}$$

giving

$$\omega_r^2 = \frac{\omega_i^2}{1 + (k^2\lambda_D^2)^{-1}}, \tag{II-83}$$

using

$$\lambda_D^2 = \frac{k_B T_e}{4\pi n_o e^2} \quad . \tag{II-84}$$

Rewriting Eq. (II-83) with the definition

$$c_s^2 = \frac{k_B T_e}{m_i} = \omega_i^2 \lambda_D^2 \tag{II-85}$$

results in

$$\omega_r^2 = \frac{k^2 c_s^2}{1 + k^2 \lambda_D^2} \quad . \tag{II-86}$$

The imaginary part γ can be found by substituting $\omega = \omega_r + i\gamma$ in the dispersion relation and using Eqs. (II-80), (II-81), and (II-86). After some algebra the approximate relation obtained is

$$\frac{\gamma}{\omega_r} = -\sqrt{\pi/8}\,\left(\frac{1}{1+k^2\lambda_D^2}\right)^{3/2}\left\{\sqrt{m_e/m_i} + \left(\frac{T_e}{T_i}\right)^{3/2} \exp\left[-\frac{T_e}{2T_i}\left(\frac{1}{1+k^2\lambda_D^2}\right)\right]\right\}. \tag{II-87}$$

We find that Eqs. (II-86) and (II-87) satisfy $\gamma << \omega_r$ and inequality (II-79) if inequalities (II-77) and (II-78) hold and the wavelength is sufficiently long ($k\lambda_D < 1$). Also we note that $\gamma < 0$ [as required for the expansion in Eq. (II-81)], indicating a damped wave.

Equations (II-69) may be solved for the electron and ion number density $n_{1,e}$ and $n_{1,i}$:

$$\begin{aligned} n_{1,e}(z,t) &= \exp(ikz - i\omega t)\delta n_e \\ &= \exp(ikz - i\omega t) \int_{-\infty}^{\infty} dv\, f_{1,e}(v) \\ n_{1,i}(z,t) &= \exp(ikz - i\omega t)\delta n_i \\ &= \exp(ikz - i\omega t) \int_{-\infty}^{\infty} dv\, f_{1,i}(v). \end{aligned} \tag{II-88}$$

Comparing with the results obtained above, we find [see Eqs. (II-71) and (II-74)]

$$\delta n_{e,i} = + \left[\frac{k^2(\phi_i + \phi_e)}{4\pi e} \chi_{e,i}(k,\omega)\right], \qquad \text{(II-89)}$$

where

$$\chi_{e,i}(k,\omega) = - \frac{\omega_{e,i}^2}{k^2 c_{e,i}^2} Z'\left(\frac{\omega}{kc_{e,i}}\right). \qquad \text{(II-90)}$$

With expansions of Eqs. (II-80) and (II-81), Eqs. (II-89) reduce to

$$\frac{\delta n_e}{\phi_e + \phi_i} = \frac{1}{4\pi\lambda_{De}^2} \left(1 + i\sqrt{\pi} \frac{\omega}{kc_e}\right),$$

and $\qquad \text{(II-91)}$

$$\frac{\delta n_i}{\phi_e + \phi_i} = \frac{k^2}{4\pi e} + \frac{\delta n_e}{\phi_e + \phi_i},$$

using $\epsilon = 1 + \chi_e + \chi_i = 0$. If we use Eqs. (II-85) and (II-86) for ω_r, then by neglecting terms smaller than first order in γ/ω_r, we obtain

$$\frac{\delta n_e}{\phi_e + \phi_i} = \frac{1}{4\pi\lambda_{De}^2} \left(1 + i\sqrt{\pi m_e/m_i} \frac{1}{1 + k^2\lambda_D^2}\right),$$

and $\qquad \text{(II-92)}$

$$\frac{\delta n_i}{\phi_e + \phi_i} = \frac{1}{4\pi\lambda_{De}^2} \left(1 + k^2\lambda_D^2 + i\sqrt{\pi m_e/m_i} \frac{1}{1 + k^2\lambda_D^2}\right).$$

Equations (II-92) show that the density fluctuations of the electrons and ions are roughly in phase with the potential. In Fig. II.9 the real parts of $n_{1,e}(z,t)$ and $n_{1,i}(z,t)$ are plotted for a time when the real part of the potential varies as cos(kz), and for a wavenumber such that $k^2\lambda_D^2 = 0.1$. For a plasma of singly ionized helium atoms, the imaginary part in Eqs. (II-92) is 2×10^{-2}, which means that the electron density lags the potential by 2×10^{-2} radians, and the ions by slightly less. These phase differences are

Figure II.9 Electron and ion density fluctuations as a function of position for $k^2\lambda_D^2 = 0.1$ in a singly-ionized helium plasma. The real parts are shown for a time t_o when $\omega_r t_o = 2\pi p$ (where p is an integer). and are normalized by the magnitude of the potential ϕ (so that the damping is not shown).

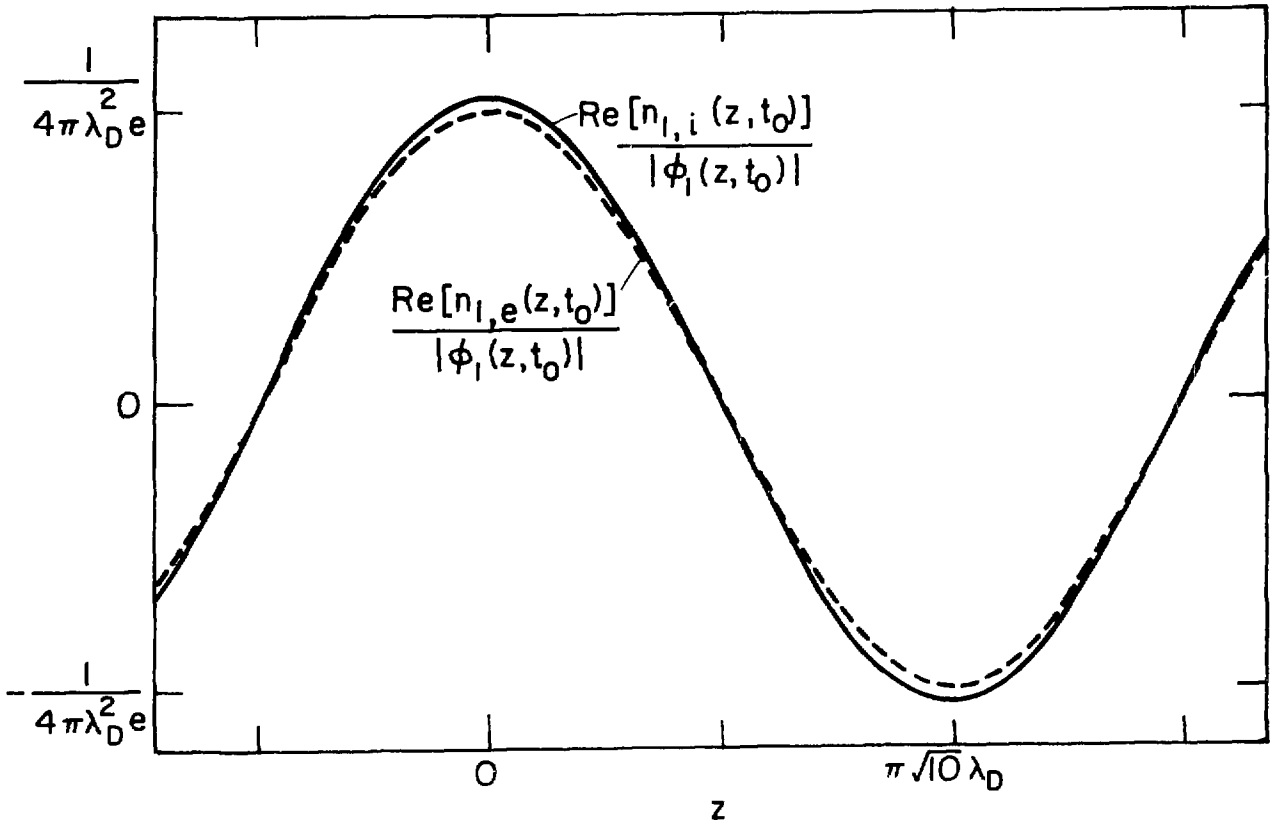

Figure 11.9

XBL 802-4674

too small to be shown in the illustration.

The ion acoustic wave is a traveling density perturbation analogous to sound waves in a compressible fluid. The frequency range is low enough for the electrons and ions to move together with a small difference in density apparent in Fig. II.9 serving to produce the field which couples electrons and ions and allows the electron pressure to drive the ions as well. From the sound speed c_s [see Eq. (II-85)] we see that the electrons' compression coefficient must be equal to unity, i.e., the frequency is sufficiently low for isothermal compression of the electrons.

2. Light Intensity Modulation by Plasma Fluctuations. With the ion acoustic wave just discussed, we have an example of the type of fluctuation which TBS may be adjusted to match. The ion acoustic waves are seen to propagate for wavenumbers smaller than $1/\lambda_D$. The theory of TBS in the first part of this chapter shows it is sensitive to a light intensity fluctuation of wavenumber k_Δ, adjustable up to a fraction (consistent with the small angle approximations in section A, at least $\sim$ 1%) of the wavenumber of light emission used.

It remains to discuss ways in which plasma fluctuations such as the ion acoustic waves, can modulate the light emission of the plasma in a way that allows TBS to detect the influence of the waves in the time and spatial dependence of the light source distribution. Starting with line emission (as used in the experiment), examples of light emission and the ways plasma fluctuations affect it are now considered.

Line emission occurs in plasmas where neutrals or ions not fully stripped exist and are excited to states from which radiative transitions occur. Usually selecting the wavelength allows a specific transition to be distinguished, which means the light is known to come

from a particular species in a particular excited state. The emission rate per unit volume is given by the product of the number density in the excited state $n(\nu,\underline{r},t)$ and the radiative transition probability:

$$s_{\nu\to\nu'}(\underline{r},t) = T_{\nu\to\nu'}n(\nu,\underline{r},t), \qquad \text{(II-93)}$$

where ν represents the set of quantum numbers specifying the initial state and ν' the final state. Since TBS can be used to measure a component of the fluctuation of $s_{\nu\to\nu'}(\underline{r},t)$ [and it can be normalized by the spatial average $\langle s_{\nu\to\nu'}\rangle(t)$], a direct measurement of the same component of the fluctuation in the population of the state ν of the species selected can be obtained.

More often one species in some excited state would provide an indirect measurement of another species or state. For example, an ion emission line intensity might reflect the density of ions. If most of the ions are in the ground state, we may expect the population of an excited state ν to be determined from that of the ground state by the probability of excitation from the ground state and the lifetime τ_ν of the state:

$$\frac{\partial n}{\partial t}(\nu,\underline{r},t) = T_{1\to\nu}n(1,\underline{r},t) - \tau_\nu^{-1}\, n(\nu,\underline{r},t). \qquad \text{(II-94)}$$

(As discussed below for excitation of neutrals by electrons, $T_{1\to\nu}$ may also include an electron density dependence which would then be reflected in the emission rate along with the dependence on the ground state ions.) This has the quasi-steady state solution:

$$n(\nu,\underline{r},t) = \tau_\nu T_{1\to\nu}n(1,\underline{r},t). \qquad \text{(II-95)}$$

To use Eq. (II-95) we have assumed that the time variation is on a long enough time scale compared with τ_ν, and that the motion of the excited species in time τ_ν is negligible. The lifetime of the state

includes all types of transitions out and is not longer than the time for a radiative transition to the state ν', which is the reciprocal of the transition probability $T_{\nu\to\nu'}$.

Instead of transitions from the ground state, the population of the state ν might involve recombination from the next higher ionization state. The rate for this process would introduce dependence on the electron density. We can consider a number of ways in which the transition probability from an initial state and species (which may not fluctuate with the plasma fluctuation of interest) to the state observed may be affected by quantities which fluctuate in a plasma wave.

In the case just mentioned, the rate for radiative recombination into the excited state ν,

$$e^- + A^{Z+1} \to A^Z(\nu) + \text{photon},$$

will vary with the temperature and density of the electron distribution. For dielectronic recombination,

$$e^- + e^- + A^{Z+1} \to e^- + A^Z(\nu),$$

the rate involves the square of the electron density as well as the electron velocity distribution.

In a weakly ionized gas, the density of neturals in the ground state is unlikely to fluctuate with a plasma wave. However, excitation by collisions with plasma electrons introduces a transition rate that depends on the electron density and velocity distribution. The 2p to 2s He(I) transitions used in the experiment are an example. As shown above, the electrons in an ion acoustic wave behave isothermally. In fact, we can see from Eq. (II-69) that there is very little perturbation of the electron velocity distribution for speeds $|v| >> |\omega/k|$. Since the phase velocity ω/k is less than or the order

of the sound speed, there is little perturbation of the distribution for velocities greater than the electron thermal speed. The thermal speed in the helium discharge of the experiment is not even sufficient to excite a helium atom in the ground state. As is typical in such electric discharges, it is the tail of electron velocity distribution that is involved in collisional excitation and ionization. Thus, the transition selected is expected to respond just to the electron density fluctuations in ion acoustic waves.

Next, we can consider radiative recombination directly. Selecting photons due to recombination of an electron and an ion (requiring selection of a range of wavelengths since free electrons have a continuum of allowed states) yields a light intensity proportional to the collision rate of electrons with ions. The intensity will then vary as the product of the electron and ion densities, an advantage for ion acoustic waves or other quasi-neutral fluctuations. However, the recombination rate is also quite sensitive to the electron temperature or velocity distribution, and this may cancel or dominate the response in waves where temperature fluctuates as well as density.

The most highly excited states tend to merge with the continuum in a plasma. For a sufficiently high principal quantum number p, we may expect the Saha equilibrium population density to apply:

$$n_E(P) = n_i n_e p^2 (h^2/2\pi m k_B T_e)^{3/2} \exp(I_p/k_B T_e), \qquad \text{(II-96)}$$

where $n_E(p)$ is the equilibrium population density, n_e and n_i densities of electrons and ions, h is Planck's constant, and I_p is the ionization potential of the level p. If this equilbirum holds on the time scale of the fluctuations to be observed, it is unnecessary to try to distinguish the recombination continuum from the limit of the series

of lines (for transitions to the same final state).

Another source of continuum radiation, and the major light source for fully ionized plasmas, is bremsstrahlung from electrons accelerated in encounters with ions. Since bremsstrahlung also involves collisions between electrons and ions, the emission rate is proportional to the product of their densities. For temperatures high enough to make bremsstrahlung more important, i.e., as recombination and collisional excitation cross sections decrease, the bandwidth of the bremsstrahlung radiation exceeds the range of wavelengths which is likely to be useful for an achromatic TBS system. In this case the temperature dependence of bremsstrahlung emission for a fixed wavelength range, rather than the temperature dependence of the total emission rate, is of interest. For a Maxwellian electron velocity distribution, the emission rate per unit frequency varies approximately as the reciprocal of the square root of the temperature. In a wave where electrons undergo adiabatic compressions the temperature dependence would partially cancel the electron density dependence.

Neither recombination light nor bremsstrahlung is an indirect measure of fluctuations in the sense that emission occurs subsequent to some excitation which is affected by a fluctuating property (electron density or temperature, etc.). Thus, we can expect to get a local dependence of their emission rate [or source density $s(\underline{r},t)$] fluctuations on collective oscillations of the ion density, or electron density or temperature.

The discussion of this section illustrates how a plasma wave can modulate light sources and allow detection by TBS. Numerous possibilities clearly exist, but a general analysis would be a large

undertaking. The intention here is to point out possibilities and limitations to consider in exploring specific applications of TBS.

REFERENCES

1. P.S. Rostler, Ph.D. Thesis, University of California, Berkeley (1974) (unpublished).
2. B.D. Billard, W.S. Cooper, and W.B. Kunkel, Bull. Am. Phys. Soc. 19, 975 (1974).
3. Ref. 1, pp. 63-69.
4. J.D. Jackson, Classical Electrodynamics (Wiley, New York, 1962), p. 183.
5. Ibid., p. 186.
6. Ref. 1, pp. 8-10.
7. Ibid, pp. 224-225.
8. L. Tonks and I. Langmuir, Phys. Rev. 33, 195 (1929).
9. D. Ilić, G.M. Wheeler, F.W. Crawford, and S.A. Self, J. Plasma Phys. 12, 433 (1974).
10. R.N. Franklin, Plasma Phenomena in Gas Discharges (Clarendon Press, Oxford, 1976), p. 13.
11. Ibid., pp. 113 and 140.
12. B.D. Fried and S.D. Conte, The Plasma Dispersion Function (Academic, New York, 1961).

CHAPTER III: SOME CONSIDERATIONS FOR THE DESIGN OF THE TBS EXPERIMENT

The experimental arrangement for testing a two-beam spectrometer system includes four major parts: the plasma, the optical system, the detectors and amplifier, and the data acquisition and analysis system. The purpose of this chapter is to describe the more important features of a TBS measurement as illustrated by this experiment, leaving more specific details of the apparatus and procedures for Chapter IV and the appendices.

A. Hot Cathode Discharge

A hot cathode positive column plasma was chosen for this experiment because it promised features fairly well suited to TBS, in addition to being a reasonably straightforward project to set up. The object was a plasma in which an appropriate wave is present or can be excited while light emission requirements for TBS are satisfied. This section will concentrate on what makes a plasma like this suitable for TBS with the intention of indicating how a given plasma may be evaluated for the possible use of this technique. A more detailed discussion of the plasma and the waves used will be found in Chapter IV.

The first feature of the plasma of importance is the spectrum of waves present. TBS is designed to see waves of selected wavenumber $\underline{k}$ perpendicular to the direction from which the light is viewed. The limits on the magnitude of $\underline{k}$ which can be selected are like the limits imposed by laser scattering, except that the small $\underline{k}$ limit is not as difficult to obtain in this case. There are two possible upper limits on the frequency $\omega(\underline{k})$ of the wave. One is set by the bandwidth of the detector and the other has to do with the coupling

between the wave and the light sources (discussed in the next paragraph). In addition, the spectral density $S(\underline{k},\omega)$ of the wave fluctuations in the plasma must be sufficient for the signal-to-noise requirements explained in Section D. For a given level of fluctuation, say $\delta n/n$, in the plasma due to the presence of the waves, there is then an upper limit on $\Delta\omega$, the range of frequencies excited, in addition to the limit on ω.

The characteristics of the emitted light are also important in determining the ability to detect the waves in the plasma. First, the plasma must satisfy the assumption of being an optically thin set of incoherent sources. Next, the coupling of the wave fluctuations to light sources mentioned above must be satisfied. Either the sources must be of a species whose density fluctuates with the wave or a species whose excitation rate is affected by the wave. In the latter case, the lifetime of the excitation must be short enough compared with the period of the wave such that the emission rate can vary as fast as the excitation rate varies with the fluctuations. Lastly, the intensity of the light is a factor affecting the signal-to-noise ratio.

In the positive column, likely candidates for waves are striations, ion acoustic waves, and electron plasma waves. Striations tend to be low frequency coherent ($\Delta\omega$ small) modes well coupled with the light but with wavelengths that are rather long. The light fluctuations have been measured[1] simply by looking at a short enough section of the column with a suitable detector. Electron plasma waves of wavelength less than or the order of the column radius propagate at frequencies greater than or the order of ω_p.

They are longitudinal waves which perturb the electron density and velocity distribution, both of which affect the excitation rate of the neutrals in the column. However, plasma frequencies in the gigahertz range for densities $n_e \gtrsim 10^{10}$ cm^{-3} are high enough to cause difficulties with the bandwidth limitations of detectors and the transition rates of excited states. In addition, if the frequency spread $\Delta\omega$ of the wave spectrum is an appreciable fraction of ω_p, the spectral density may be low for signal-to-noise requirements. Ion acoustic waves are a good example of a well-suited mode for TBS. Their frequency range is much lower than that of the electron plasma waves for the same wavenumber range. The density fluctuations can couple with the light emission by neutral atoms through the dependence of the collisional excitation rate on electron density.

In the positive column of this experiment the dominant form of light emission is line radiation of excited neutrals. As already indicated, excitation is via collisions with electrons and depends on the electron density and velocity distribution, as well as on neutral density. Lifetimes of excited states are of the order of 10^{-8} sec and could be shortened by collisional transitions back and forth in a steady-state situation. Other forms of light emission which could be considered include ion lines, recombination light, and bremsstrahlung. These all depend directly on ion density, as well as on electron density. The intensities possible are lower in most cases, so that the TBS may be more difficult. In the case of bremsstrahlung high Z impurities in hot hydrogen plasmas would increase the light and improve the effectiveness TBS.

B. Optical System

The key element in the optical system is the interferometer, which provides separate paths for light of two orthogonal polarization components (called A and B). In addition, the input system must project an image of the plasma suitable for the interferometer and select a polarization of the light consisting of equal coherent components of A and B polarization. An analyzer must separate the resultant light into orthogonal components (called 1 and 2) containing equal amounts of polarization A and B, and image the two components onto separate detectors. A filter may be necessary to select from the light emitted by the plasma a limited range of wavelengths for which the interferometer is designed.

This section describes the main functions of these components, starting with the interferometer, which determines the requirements for the others. More detailed design, analysis, and alignment information is included in Chapter IV and Appendices A through C.

According to the analysis (Appendix A), the alternate paths for the two polarizations A and B in the interferometer result in two similar transformations composed of rotations and reflections of the points seen through it. Via paths A and B we see virtual images $\underline{P}'_A \equiv T_A\underline{P}$ and $\underline{P}'_B \equiv T_B\underline{P}$ of point $\underline{P}$ through the interferometer. Since the transforms T_A and T_B each reduce to a single rotation or combination of a rotation and a reflection (if assumptions discussed in Appendix A hold), one can simply transform a coordinate system, and the coordinates of the transformed points in the transformed coordinate system will be the same as the coordinates of the untransformed points in the original coordinate system. Figure III.1 shows an

Figure III.1 Effects of interferometer upon incident light treated as a transformation of wavefronts. Here the A component is shown transformed by a rotation of 90° about the axis A. Light from the point P leaves the interferometer as if it were propagating directly from the point P'_A. Image sources and wavefronts can be found with the same coordinates as those of the originals by transforming the coordinate system by the same rotation.

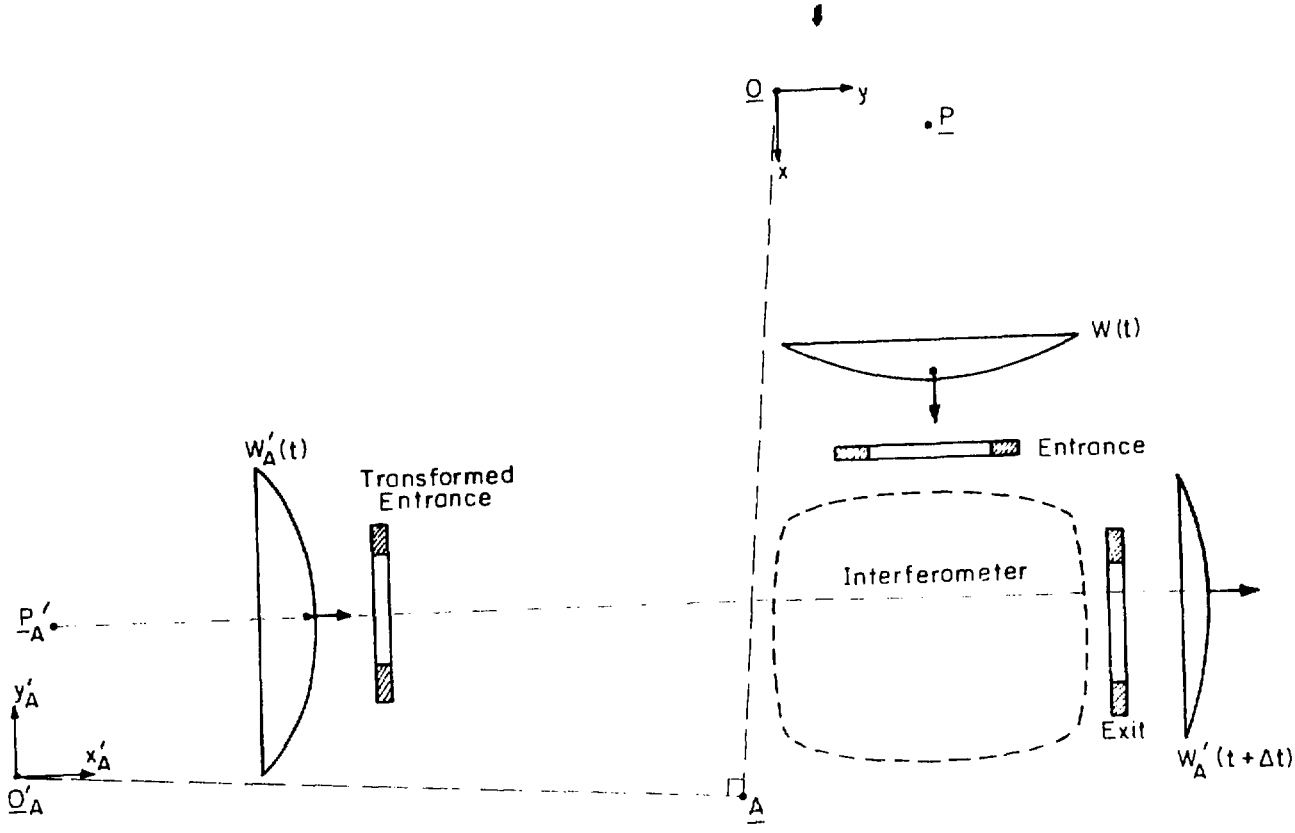
O
y
x
P
W(t)
Entrance
Interferometer
Exit
$W_A'(t)$
Transformed Entrance
P_A'
y_A'
x_A'
O_A'
A
$W_A'(t+\Delta t)$
XBL803-4927

Figure III.1

example where an approaching wavefront has been transformed along with the entrace aperture of the interferometer. Only one transformation (a rotation by $\pi/2$ radians about an axis out of the page indicated by point A) is shown for clarity. Once the transformation has been performed, the propagation of the wavefront can be followed by any convenient optical method without further regard for the details of the interferometer other than checking to see if additional apertures within the interferometer block some of the light. (We assume for the moment this is attended to in the set-up and adjustment of the actual interferometer.) Equivalently, one may determine the propagation from the original wavefront without the interferometer and apply the transformation afterwards.

The next illustration (Fig. III.2) shows an example where transformations A and B applied to an approaching wavefront result in two image wavefronts slightly offset from each other. If the original wavefront is a spherical front originating at a point P, the image fronts are also spherical wavefronts originating at P'_A and P'_B. The interference effect associated with the source P is then a two point-source pattern consisting of hyperboloids with foci at P'_A and P'_B. An example is shown in Fig. III.3 (a), where the hyperbolas added indicate positions of some possible resultant polarizations occurring in the plane of the figure. Figure III.3 (b) traces the positions P_{max} where sources would be most visible to a detector at D sensitive to polarization 1, and the positions P_{min} of minimum visibility. For a detector at D sensitive to polarization 2 the roles of P_{max} and P_{min} would reversed. One can compare Figs. III.3 (a) and III.3 (b) to see how the hyperboloids of P_{max} and P_{min} can be

Figure III.2 Transformation of the wavefronts for both beams A and B. The two paths through the interferometer are represented by the two rotations of 90° about parallel axes A and B. Each source produces a pair of wavefronts at the exit of the interferometer.

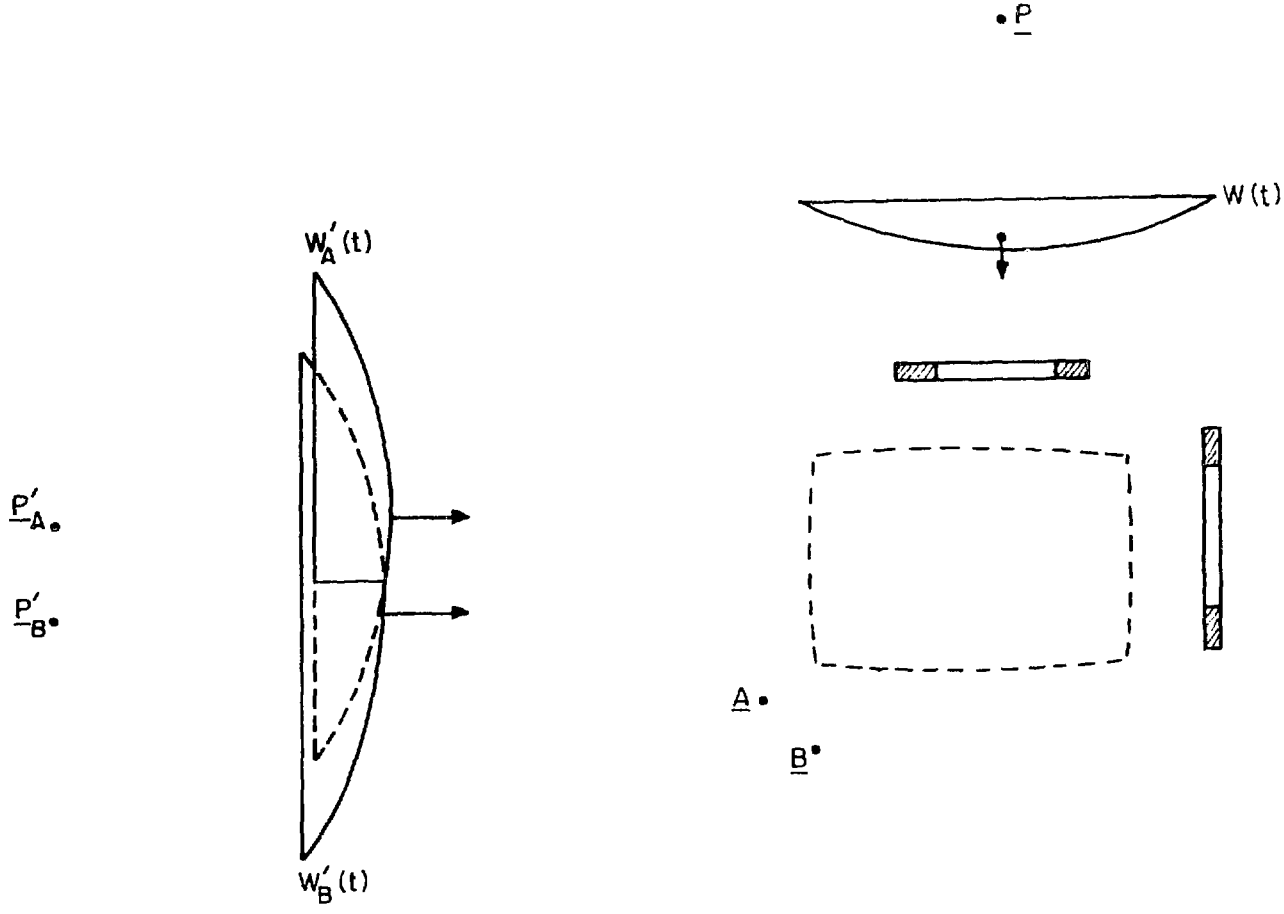

XBL803-4926

Figure III.2

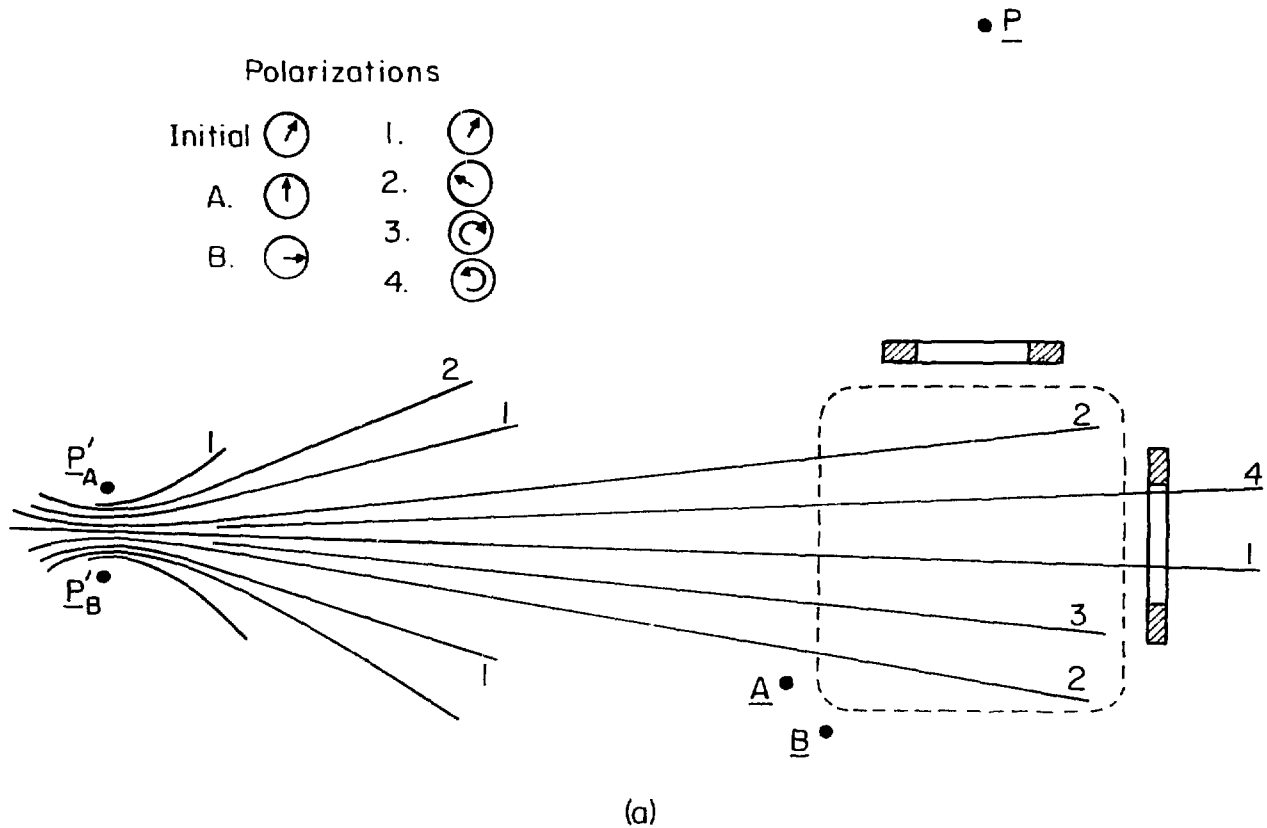

Figure III.3 (a) Polarization interference pattern produced by a point source at P. The lines represent points of equal resultant polarization. These are only observable beyond the exit of the interferometer.

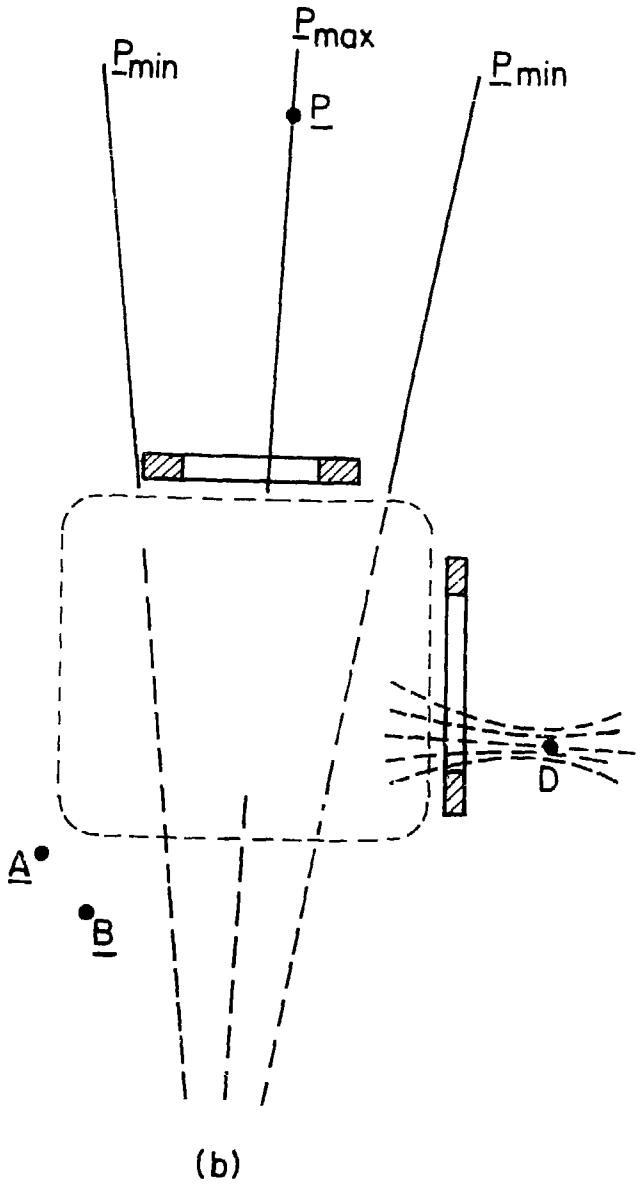

XBL802-4664

Figure III.3 (b) Positions of equal source visibility for a small polarization 1 detector. A small detector at D sensitive only to light of polarization 1 would receive maximum light intensity from sources located at points $\underline{P}_{max}$ and minimum intensity from sources at points $\underline{P}_{min}$.

generated by tracing the points $\underline{P}$ such that the same order interference fringe continues to pass through the point $\underline{D}$. In the example shown the separation of $\underline{P}'_A$ and $\underline{P}'_B$ is independent of the position of $\underline{P}$, so the fringe pattern shown in Fig. III.3 (a) moves bodily with $\underline{P}'_A$ and $\underline{P}'_B$. A distribution of incoherent sources resulting in greater light emission near the points $\underline{P}_{max}$ than near the points $\underline{P}_{min}$ can be detected by the difference in light intensity for the two kinds of detectors at $\underline{D}$.

Note also that the smaller the optical path length between $\underline{P}$ (or $\underline{P}'_A, \underline{P}'_B$) and D, or equivalently the greater the curvature of the wavefronts at $\underline{D}$, the closer will be the spacing of the fringes. The result is a constraint on the size of the analyzer which will separate polarizations 1 and 2 for two detectors to be discussed later in this section. For efficient use of the light accepted by the interferometer the curvature of the wavefronts at the position of the analyzer should be small enough to result in an essentially constant interference pattern over the width of the analyzer aperture. Because of this requirement, it is necessary to use some kind of focusing system to provide flexibility in matching the pattern of source visibility to the plasma wave chosen.

Figure III.4 illustrates the use of a focusing system of focal length f to collimate light from a region of plasma, and at the same time translate the asymptotic separation between the points of maximum visibility [the difference $\Delta\theta$ in angles of asymptotes of the hyperbolas in Fig. III.3 (b)] into a spacing $f\Delta\theta$ in the plasma. The collimation of the light from the region near the focal plane of the system provides the constant interference pattern needed to allow a

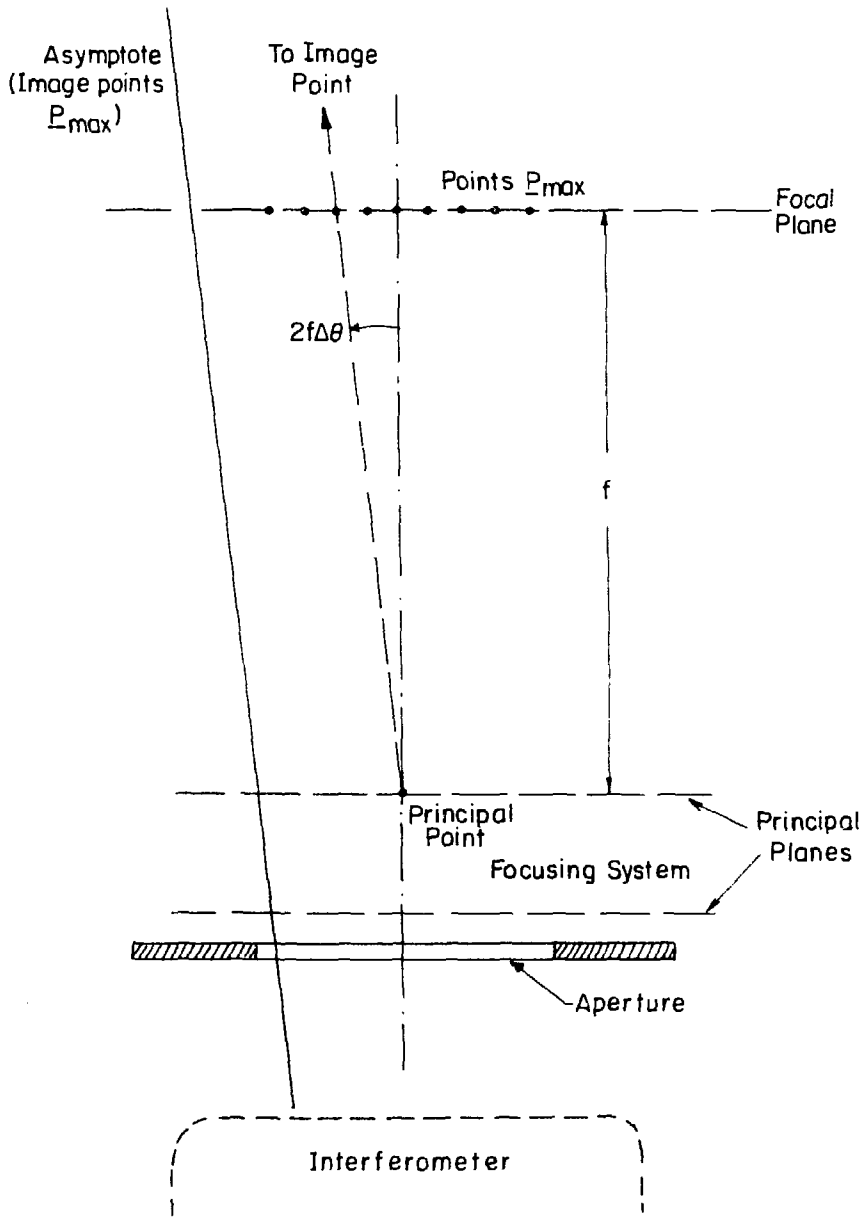

XBL 803-4918

Figure III.4 Input focusing system added for collimation of the light. Near the focal plane, the positions of the points $\underline{P}_{max}$ and $\underline{P}_{min}$ are independent of the position of the detector, allowing use of a detector large enough to collect the entire wavefront which can pass through the interferometer.

larger analyzer aperture. When the larger analyzer is used, the closer spacing of fringes in the uncollimated light from sources farther from the focal plane results in cancellations across the aperture. Thus, the contrast in visibility to detectors 1 and 2 of sources away from the focal plane is reduced, and with it the possibility of obtaining an intensity difference signal from the selected source distribution, unless it occurs near the focal plane of the system. In this way spatial resolution along the line of sight of the system is obtainable.

By considering the features of the interferometer we have already begun to discover what components are needed on the input and output sides to complete the optical system. One other property of the interferometer that we need to know is its light acceptance. Since collimated light (plane wavefronts) is desired we can measure the light accepted in terms of the area of the wavefronts that get through the apertures of the interferometer and the solid angle within which the direction of propagation of the accepted wavefronts lie. The various components in the optical system can be matched to the interferometer by the standard procedure[2] as illustrated in the example (Figure III.5). For all the real apertures, we use images formed by any lenses between the aperture and the interferometer, and then apply the transformation representing the images formed by the interferometer to gather all the images to one side of the interferometer. In the example, the apertures on the input side of the interferometer are transformed to the space corresponding to the exit side. Then we see which apertures limit the light acceptance. The case illustrated shows that two of the apertures within the input focusing

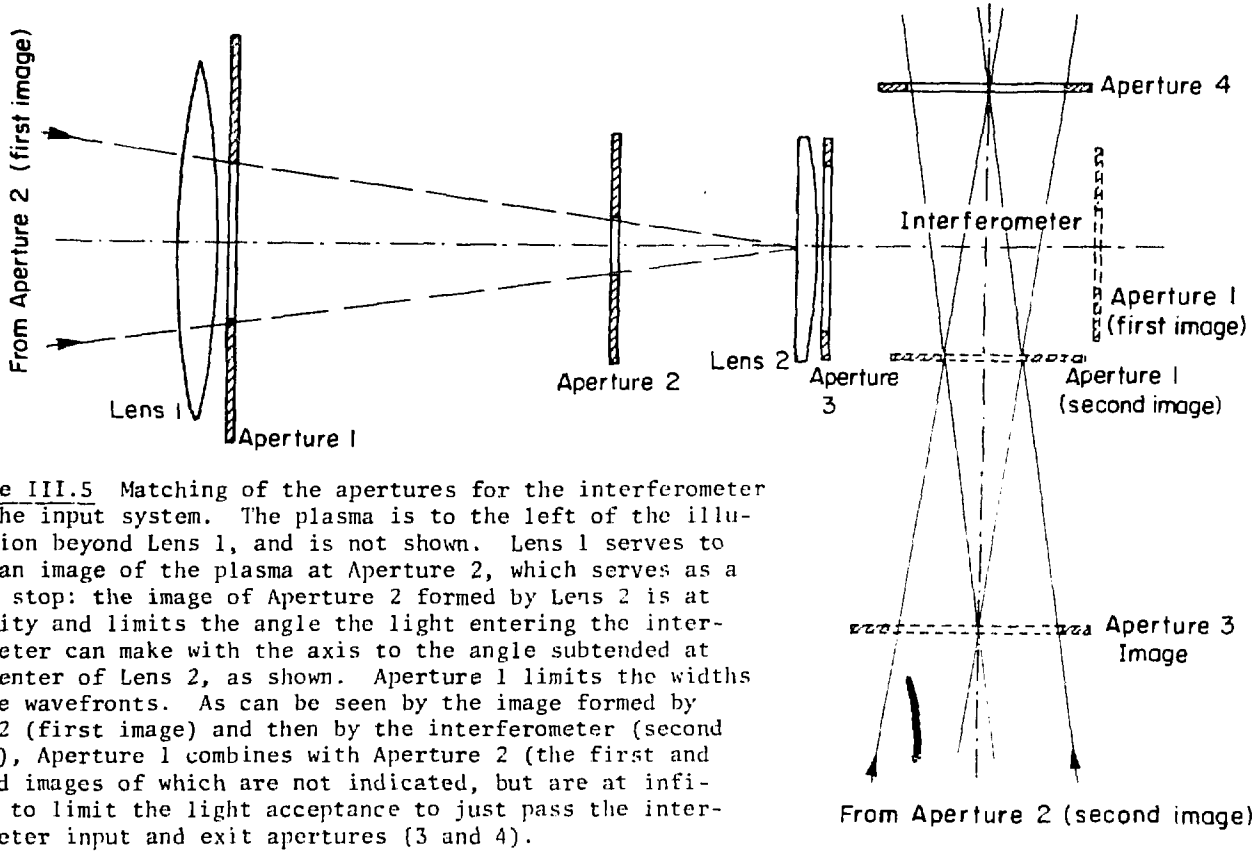

Figure III.5 Matching of the apertures for the interferometer and the input system. The plasma is to the left of the illustration beyond Lens 1, and is not shown. Lens 1 serves to form an image of the plasma at Aperture 2, which serves as a field stop: the image of Aperture 2 formed by Lens 2 is at infinity and limits the angle the light entering the interferometer can make with the axis to the angle subtended at the center of Lens 2, as shown. Aperture 1 limits the widths of the wavefronts. As can be seen by the image formed by Lens 2 (first image) and then by the interferometer (second image), Aperture 1 combines with Aperture 2 (the first and second images of which are not indicated, but are at infinity) to limit the light acceptance to just pass the interferometer input and exit apertures (3 and 4).

system were chosen to define the light acceptance of the system. One was placed so that its image is at infinity and subtends an angle θ, and the other so that its image is at the appropriate point between the output aperture and the image of the input aperture of the interferometer.

As has already been indicated in the introductory discussion of TBS (and as has been assumed in this section), the light entering the interferometer must have a polarization which consists of equal components of the orthogonal polarizations A and B. Also the light must be filtered to limit the wavelength range before it reaches the detectors so that the variation of the interference effect with wavelength is not excessive (see also the discussion of achromatic interferometers in Appendix B). Therefore, the input system will probably have to include some form of polarizer, while any filter required can go either in the input system or the output system.

The polarization analyzer mentioned above will be some form of polarizing beamsplitter to allow simultaneous monitoring of the two complementary patterns of source visibility with two separate detectors. It is likely to be similar to the one used for the interferometer, in which case it may be necessary to include some optical system to relay the light from the output of the interferometer. As in the example illustrated in Fig. III.5, we can think of the relay system (a telescope or focusing system) placing an image of the analyzer (such as that shown in Fig. III.6) at an appropriate place in the region of the interferometer. The same relay system may be made to focus the light on the detectors (to be discussed in Section C).

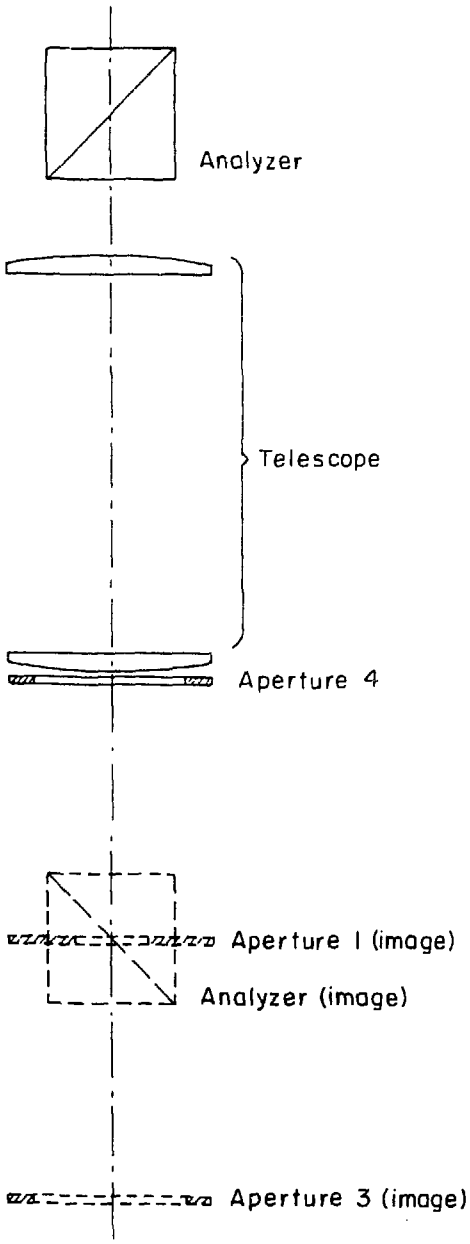

Figure III.6 Use of a telescope output system to relay light from the interferometer to the analyzer. Arranging for the analyzer image to be near the position of the limiting aperture image makes the most efficient use of the light acceptance of the analyzer.

In summary, the general configuration of the optical system includes an input focusing system with the region of interest in the plasma at the focal plane, the interferometer, a filter, and the output system. The input system, which includes an initial polarizer to provide equal coherent components from each source for the interferometer beams A and B, collimates and relays the light to the interferometer, matching its light acceptance. In the output system light is relayed through a polarizing beamsplitter (the analyzer) onto detectors for polarizations 1 and 2. For a source sufficiently close to the focal plane of the input system, the two-beam spectrometer selectively passes emitted light to detector 1 or detector 2 according to the source's position in a pattern selected to match a possible plasma wave.

C. Detector-Amplifier

To understand the requirements for and characteristics of the detector-amplifier combination, we need to consider the nature of the signal contained in the light at the output of the optical system. That light is separated into orthogonal polarization components 1 and 2 representing complementary patterns of visibility vs. position of sources in the plasma. The difference in total intensity of polarization 1 and 2 then amounts to a spatial average of the intensity fluctuations in the plasma light, selecting a spatial Fourier component of the source intensity distribution. When the component selected matches the wavevector of a fluctuation in the plasma, we expect the difference in light intensity of polarizations 1 and 2 to have the same time dependence as the wave in the plasma.

When the light is detected, its quantum nature becomes important in the description. As Rostler has discussed in more detail in his thesis,[3] we interpret the calculation of intensities outlined above as a semiclassical derivation of probabilities per unit time of photons reaching the detectors. Furthermore, statistical fluctuations in the actual arrival (and detection)of photons is one source of noise masking the signal, which is a relative difference in probability of arrival (and detection) of photons for detectors 1 and 2.

In this section we assume an average probability $\dot{Q}\,dt$ that a photon arrives at detector 1 in any time interval dt, and the same for detector 2. We also assume a time dependent change in probability $\beta(t)$, expressed as a fractional increase in the probability of arrival of photons at 1 and corresponding decrease for detector 2, represents the signal contained in the light. Thus at time t the probability of arrival of a photon in a small time interval dt is

$$p_1(t)\,dt = \dot{Q}[1 + \beta(t)]dt \qquad \text{(III-1)}$$

and

$$p_2(t)\,dt = \dot{Q}[1 - \beta(t)]dt \qquad \text{(III-2)}$$

for detectors 1 and 2 respectively.

Rostler[4] gives one approach to the estimate of signal-to-noise ratio in a measurement of this form of signal. A slightly different approach is taken here intended to facilitate incorporation in the noise level effects of other characteristics of detectors which we may wish to consider.

We assume for a moment that our detector has an ideal "front end" where every arriving photon is converted into a photoelectron. Actually,

real detectors have a quantum efficiency less than one, representing the fraction of electrons per photon that actually contribute to the output, other photons being reflected or absorbed without producing photoelectrons, or producing photoelectrons which fail to be collected to produce an output signal. These effects we will include in a moment, in the discussion of the characteristics of real detectors and amplifiers.

With an electron for every arriving photon, we have a current equivalent to the light intensity. A light intensity of $\dot{Q}$ photons per second produces a current $I_o = e\dot{Q}$ (where e is the elementary charge in Coulombs). The noise associated with the light is equivalent to the shot noise associated with this current, which has a noise power spectral density of $2eI_o = 2e^2\dot{Q}$ (in A^2/Hz). The signal current is proportional to $\beta(t)\dot{Q}$, so that the total currents in detectors 1 and 2 are

$$I_1(t) = [1 + \beta(t)]e\dot{Q} \qquad \text{(III-3)}$$

and

$$I_2(t) = [1 - \beta(t)]e\dot{Q}. \qquad \text{(III-4)}$$

We note that the noise amplitude increases with the square root of the light intensity, while the signal amplitude is proportional to the light intensity.

In addition to the inherent noise discussed above, other noise sources degrade the signal in a practical detector-amplifier combination. As mentioned above the actual current is reduced by the quantum efficiency η. Practical detectors will exhibit a leakage or dark current even in the absence of light. The amplifier will have some equivalent input noise, and there may be thermal or Johnson

noise in the circuit. To help with the comparison of alternative detector-amplifier combinations, it will be convenient to express all the practical effects in terms of an equivalent dark current added to the ideal detector. We find a current $I_n(\omega)$, which, added to $e\dot{Q}$, results in a noise power spectral density equivalent to the various contributions in the real circuit.

For example, for polarization 1 the ideal detector photocurrent $e\dot{Q}[1 + \xi(t)]$ is split into a fraction $(1 - \eta)$ that is lost and a fraction η representing the photocurrent of the actual detector. To this is added the dark current I_D. The input noise of the amplifier and the Johnson noise of the circuit are expressed in terms of equivalent currents I_A and I_J to be added to the dark current. We can treat the components of the noise this way because they are statistically independent so that their amplitudes add in quadrature. A current which has an equivalent amount of shot noise is proportional to the square of that noise amplitude, so that adding appropriate currents amounts to combining the noise components in quadrature.

Now we wish to find the equivalent dark current $I_n(\omega)$ in the ideal detector. First define I_1 such that

$$\eta I_1(\omega) \equiv I_D + I_J(\omega) + I_A(\omega). \qquad \text{(III-5)}$$

We can account for the additional current producing shot noise by adding $I_1(\omega)$ to $e\dot{Q}$ in the ideal detector. However, the effect of quantum efficiency $\eta < 1$ is to reduce the signal power by a factor of η^2, while the noise power is only reduced by η. Therefore we must increase the current added to the ideal detector further to match the relation of the signal-to-noise in the actual detector. We find that

$$I_n(\omega) + e\dot{Q} = [I_1(\omega) + e\dot{Q}]/\eta \qquad \text{(III-6)}$$

yields the appropriate equivalent dark current I_n.

The output of the detector-amplifier can now be characterized by a voltage V_s due to the signal

$$V_s(\omega) = \eta\xi(\omega)e\dot{Q}\,\Xi(\omega), \qquad \text{(III-7)}$$

where $\xi(\omega)$ is the Fourier transform of $\beta(t)$, and $\Xi(\omega)$ is the transfer function of the amplifier. The same transfer function applies to the input noise, so that at the output the noise power spectral density will be

$$|V_n(\omega)|^2 = \frac{2[eI_n(\omega) + e^2\dot{Q}]}{2\pi}\,|\Xi(\omega)|^2. \qquad \text{(III-8)}$$

Thus the function $\Xi(\omega)$ will express the gain and bandwidth of the detector-amplifier circuit. The bandwidth of course must satisfy the requirement that it be sufficient to pass the frequencies of importance in the signal $\beta(\omega)$.

D. Data Acquisition and Analysis

To complete the consideration of the problem of observing a plasma fluctuation via TBS, we need to know how the signal discussed in the last section may be observed in the presence of the noise. As was shown, the signal to be analyzed is essentially a replica of the model photocurrent

$$I_n(\omega) + eQ[1 \pm \beta(t)], \qquad \text{(III-9)}$$

for detector 1 or 2. The signal desired is the difference in currents between detectors 1 and 2. If the average light intensity $\dot{Q}$ fluctuates, taking the difference in the two outputs will reduce the spurious signal that results to the extent that the balance between

channel 1 and 2 is good.

If we express the signal we wish to observe in terms of its Fourier transform $\beta(\omega)$, then the signal power spectral density is proportional to

$$|I_S(\omega)|^2 = 4\beta^*(\omega)\beta(\omega)e^2\dot{Q}^2, \qquad \text{(III-10)}$$

while the noise power spectral density is proportional to

$$|I_N(\omega)|^2 = 2\frac{eI_n(\omega) + e^2\dot{Q}}{\pi}. \qquad \text{(III-11)}$$

If we can substitute an equivalent unmodulated light source such that the noise is matched but there is no signal, then a possible observation of the signal would be a case where a measurement of some property of the output shows a significant difference between the modulated and unmodulated cases.

An example given by Rostler gives a picture of how this might be done: The fluctuation of wavenumber $\underline{k}$ to be observed is assumed to be a mode with frequency ω_o and correlation time τ. Then we can expect $\beta(t)$, which follows the time dependence of the plasma fluctuation to oscillate with a period of $2\pi/\omega_o$ and amplitude and phase roughly constant over periods of time less than τ. In Rostler's example one counts the number of (equivalent) photons arriving at detector 1 minus the number arriving at detector 2 each half period. These counts are accumulated over a time τ, reversing the sign every half period. Depending on the phase of $\beta(t)$ relative to the reversing times, one would expect a net excess or deficiency of $\beta_o\dot{Q}\tau$ counts, where β_o is roughly the root mean square of $\beta(t)$. However, this difference is out of a total of approximately $(\langle I_n\rangle/e + \dot{Q})\tau$ counts in each detector, where $\langle I_n\rangle$ is the average over ω of $I_n(\omega)$. Assuming

Poisson statistics, the actual difference could be expected to fluctuate by roughly $[(\langle I_n\rangle/e + \dot{Q})\tau]^{\frac{1}{2}}$ counts with no signal present. If $2\beta_o\dot{Q}\tau$ is significantly larger, then the signal should be observable by this form of measurement. If not, then it may be possible to observe it by repeating the above measurement a number of times and averaging the squares. After N repetitions the averaged square difference should be about $(\langle I_n\rangle/e + \dot{Q}\tau)\tau(1 \pm 1/N^{\frac{1}{2}})$ with no signal present. Since the noise is statistically independent of the signal, the presence of the latter will increase the mean square difference by $(2\beta_o\dot{Q}\tau)^2$, which will be detectable if N can be made sufficiently large.

Equations (III-10) and (III-11) [with Eq. (III.6)]: $[I_n(\omega) + e\dot{Q} = (I_1(\omega) + e\dot{Q})/\eta]$ show that the signal is more detectable the larger $\dot{Q}$ or $\beta(\omega)$ become. They also suggest a power versus frequency measurement would be appropriate for a plasma mode that has a well-defined frequency ω_o associated with the wavenumber $\underline{k}$ for which the interferometer is adjusted. In such a case the peak value of $\beta(\omega)$ is larger for a given root mean square level of fluctuation,

$$\beta_o \equiv \langle[\beta(t)]^2\rangle^{\frac{1}{2}}, \qquad \text{(III-12)}$$

and stands a better chance of showing above the background fluctuations.

As an example, suppose $\beta(\omega)$ has the form

$$\beta(\omega) = \beta_o g(\omega), \qquad \text{(III-13)}$$

so that

$$\int_{-\infty}^{\infty} d\omega \, |g(\omega)|^2 = 1. \qquad \text{(III-14)}$$

If $g(\omega)$ is confined to a finite range $\Delta\omega$, then $|g(\omega)|^2 \sim 1/\Delta\omega$ within that range. A measurement of the power spectral density of signal

plus noise at ω, made over a period of time T, will have a frequency resolution

$$\delta\omega = 2\pi/T. \qquad \text{(III-15)}$$

The expected power measured is

$$\langle P(\omega)\rangle\delta\omega = 4\beta_o^2|g(\omega)|^2e^2\dot{Q}^2\ \delta\omega + 2\frac{eI_n(\omega) + e^2\dot{Q}}{\pi}\delta\omega. \qquad \text{(III-16)}$$

The first term represents signal and the second noise. The statistics of the measurement are such that the standard deviation of the noise term is equal to it. In the range $\Delta\omega$ there are $\Delta\omega/\delta\omega$ statistically independent frequencies which can be measured in this way and for which $|g(\omega)|^2$ in the signal term will be consistently of the order of $1/\Delta\omega$. A similar set of measurements can be made in the absence of signal (modulation of the light) and subtracted from the results with the modulation to obtain just the signal term

$$\langle\Delta P(\omega)\rangle\delta\omega = 4\beta_o^2|g(\omega)|^2e^2\dot{Q}^2\ \delta\omega \pm 2\sqrt{2}\frac{eI_n(\omega) + e^2\dot{Q}}{\pi}\delta\omega. \qquad \text{(III-17)}$$

Taking advantage of the $\Delta\omega/\delta\omega$ independent values allows reduction of the standard deviation by $\sqrt{\delta\omega/\Delta\omega}$, so that β_o^2 can be measured with a standard deviation of

$$\sigma = \left(\frac{\Delta\omega\delta\omega}{2}\right)^{\frac{1}{2}}\frac{I_n(\omega)/e\dot{Q} + 1}{\pi\dot{Q}}$$

$$= \frac{1}{\dot{Q}}\left(\frac{\Delta\omega}{\pi T}\right)^{\frac{1}{2}}\left[\frac{I_n(\omega)}{e\dot{Q}} + 1\right]. \qquad \text{(III-18)}$$

The requirement that β_o^2 is greater than its standard deviation for the signal to be observable gives the inequality

$$\beta_o^2 > \frac{1}{\dot{Q}}\left(\frac{\Delta\omega}{\pi T}\right)^{\frac{1}{2}}\left[\frac{I_n(\omega)}{e\dot{Q}} + 1\right],$$

essentially the same result as that derived by Rostler, with the additional $I_n(\omega)$ term to take into account the quantum efficiency and dark noise of the detector-amplifier, as discussion in the last section.

In order to satisfy the signal-to-noise inequality, a large T may be required. To make the separate frequency measurements individually over the range $\Delta\omega$ would require $(\Delta\omega/\delta\omega)T$, but it is possible to obtain the same information in one interval T. One method is to record the amplifier output and later analyze it for all the independent frequencies, up to the bandwidth of the recorder, and there are also devices that can measure correlation functions or Fourier transforms of a signal in real time. The correlation function contains the information needed because it is the Fourier transform of the power spectrum.

If the conditions in the plasma are stationary over a long enough period of time, a number of measurements of length T could be made and the correlation functions or power spectra obtained and averaged. The result would be the same as a single measurement made for the combined length of time, so long as T is not so short that $\Delta\omega < \delta\omega$.

REFERENCES

1. See, for example, L. Pekarek, Sov. Phys. Usp. 11, 188 (1968).

2. K. Halbach, Am. J. Phys. 32, 90 (1964). See especially pp. 101-102.

3. P.S. Rostler, Ph.D. Thesis, University of California (1974, unpublished), pp. 88-92.

4. Ibid., pp. 94-102.

CHAPTER IV: EXPERIMENTAL PROCEDURE AND RESULTS

This chapter contains a discussion of the experimental procedures and results with a more specific description of of the apparatus. It is divided into two sections, one a report of the preliminary investigation of waves in the discharge and the other the description of and experience with the prototype TBS system constructed. In this second section, more detailed measurements of the fluctuations in the discharge are also discussed.

A. Preliminary Investigation of Waves

The hot-cathode positive column chosen for this experiment was designed with the hope of launching an ion acoustic wave suitable for a TBS measurement, and verifying its presence using probes. This section first describes the discharge apparatus and the methods used in the unsuccessful attempt to propagate and detect ion acoustic waves. Then, preliminary measurements obtained with a helium discharge of spontaneous fluctuations which could be suitable for observation by TBS are reported.

Figure IV.1 is a schematic version of the basic positive column used. The direct current heated tungsten filament cathode is contained in a copper assembly attached to one end of the glass tubing forming the positive column. The anode is inserted through the cover for the other end (originally the cover was the anode). Gas is fed in and pumped away at the cathode end. When the arc is struck, current flow along the column maintains partial ionization of the gas.

The length of the configuration can be varied by using a different length of glass tubing. In addition, two lengths of tubing can

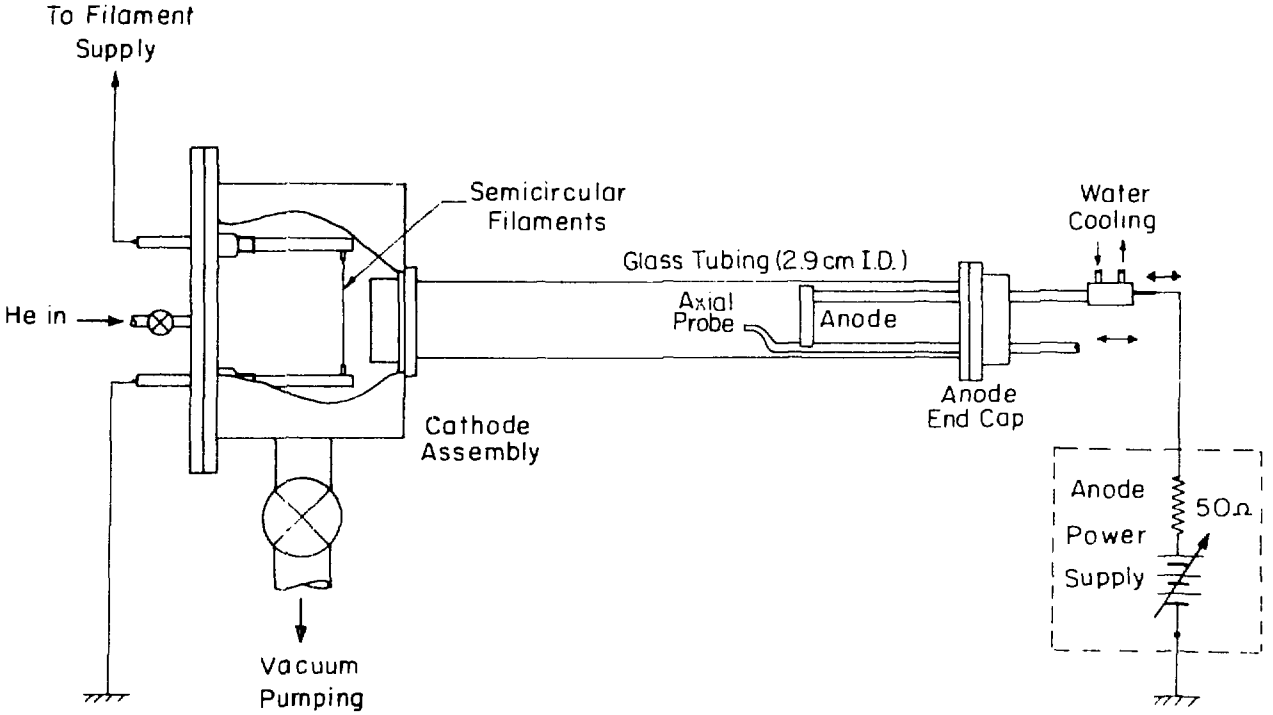

Figure IV.1 Schematic of basic positive column discharge configuration. Two semicircular filaments form a roughly circular cathode with radius larger than that of the discharge tube. The copper cathode assembly serves to contain most of the light from the incandescent filaments.

be joined by a grid assembly that provides a way of mounting various types of grids between the two sections of the positive column (see Fig. IV.2 for a view of the grid assembly in cross section). The cathode, grid, and anode assemblies all make a vacuum seal to the glass tubing with an O-ring seal around the outside.

The anode assembly contains a fitting for inserting a probe along the wall of the tube. The end of the probe is bent, or dog-legged, so that the tip can reach the axis of the tube when rotated into position. Sliding the probe through the fitting allows variation of the tip position along the axis. An example of a double probe used is sketched in Fig. IV.3.

With the discharge tube radius of about 1.5 cm, a wavelength of a few millimeters or less was desirable for a TBS test wave. There would be difficulty exciting and detecting any wavelengths less than about 1 mm due to the size of the grids and probes to be employed. Argon was used for the discharge, giving plasma densities up to about 10^{11} cm^{-3} and electron temperatures of about 4 to 6 eV, for discharge currents of about 1 ampere and gas pressure about 10 millitorr. The argon discharge provided ample light intensity, with bands of lines that would allow demonstration of the achromatic TBS system. With an ion acoustic speed of order 3.5×10^5 cm/sec, a conveniently low frequency of about 1 MHz would provide a reasonably short wavelength for a test of TBS.

The general method used to test for ion acoustic wave excitation and propagation was to introduce grids (mounted in the grid assembly) across the discharge tube, drive them with a voltage at an appropriate frequency, and attempt to detect any resulting disturbance with the

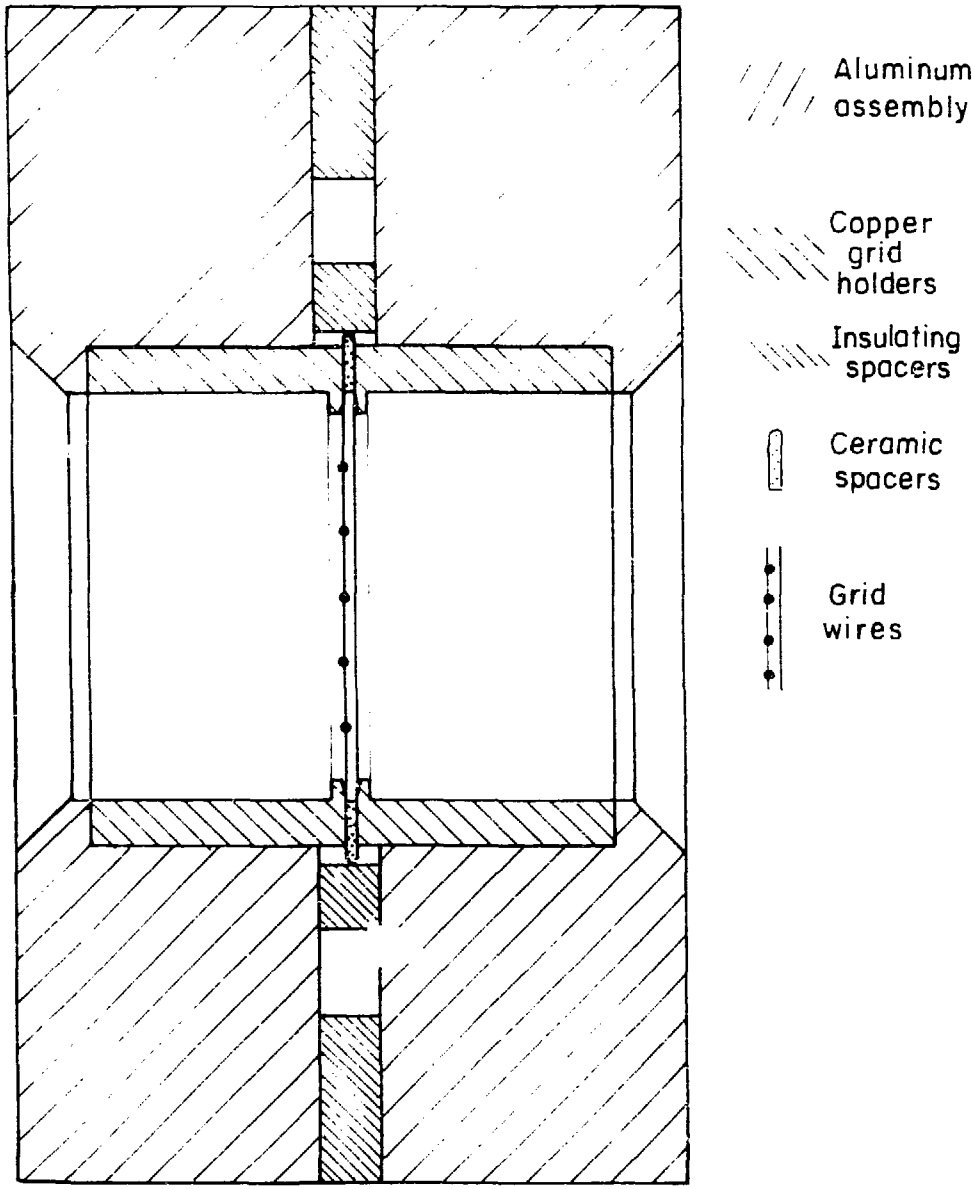

XBL 802-4656

Figure IV.2 Cross section of double grid assembly, shown twice actual size. A set of parallel tungsten wires stretched across a copper grid holder forms each grid. The three vacuum seals using O-rings (not shown) are made between the insulating spacers and at each end in the beveled space around the outside of the glass tubing. The two sections of tubing (also not shown) slide in from either side and seat at the lips of the copper grid holders.

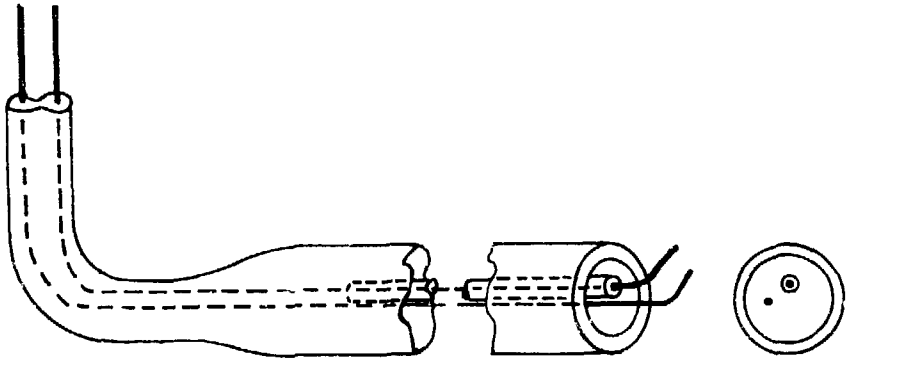

Figure IV.3 Double probe used for fluctuation studies. Two platinum wires are sealed side-by-side in glass tubes, with 3 to 5 mm of wire left exposed at one end to form the probe tips. The other ends of the wire are brought through a larger length of tube forming the shaft, and a seal is made between the shaft and the glass covering the wires near the tips. A smaller glass tube is slid over one of the wires and into the shaft to insulate the two wires. The end of the probe is bent upward so that the tips reach the center of the discharge tube from the shaft along the wall.

movable axial probe. The probe can be biased to respond to density fluctuations. For example, by biasing the probe to draw mainly electron current (in the electron transition region of the characteristic) one could expect fluctuations in the bias current proportional to the density fluctuation.[1] The propagation can be verified by moving the probe axially and observing the phase shift of the response as the distance the wave has to propagate is changed. Some of the problems encountered and techniques tried are described below.

The first difficulty in attempting to drive an ion acoustic wave with a grid is that the grid tends to couple to electron plasma waves better than to ion acoustic waves. The problem is the electric fields of the grids tend to induce the charge separation important in electron plasma oscillations rather than the bulk plasma motion of ion acoustic waves. While the electron plasma wave does not propagate in homogeneous plasmas at ion acoustic frequencies, it <u>does</u> propagate as a guided mode or surface wave on a finite plasma column.[2,3] The phase velocity for long wavelengths is of the order of the column radius times the plasma frequency. In the case of the argon positive column used in this experiment, the velocity is of the order of the speed of light. This mode, along with any spurious coupling between the grid and probe circuits, produces an interfering response to the driving signal. The use of double grids and double probes was intended to minimize this problem by allowing out-of-phase driving signals, in an attempt to cancel the excitation of and response to the long wavelength modes coupling the grids and probe.

Additional help in recognizing the presence of any ion acoustic wave signal results from moving the probe axially and observing the

change in response. The spurious pickup discussed above is not expected to change significantly except for possible amplitude variation. With a signal due to ion acoustic wave propagation, an interference effect would occur, causing a periodic variation of the amplitude and phase of the total signal as the phase of the ion acoustic component shifts with probe separation. A phase sensitive detection technique used by Wong et al.[4] was found useful in this situation. Figure IV.4 shows schematically how in-phase and quadrature components of the probe signal obtained by phase sensitive detection are used with an x-y recorder to plot a diagram on the complex plane of the probe signal. Figure IV.5 (a) illustrates how the curve traced as a function of probe position amounts to a phasor diagram of the probe signal, resulting in this example from the interference between a fast mode with a slight decay of amplitude with separation, and a slow decaying mode with a wavelength of about a centimeter. Figure IV.5 (b) shows how corresponding traces of the probe signal might appear on an oscilloscope triggered by the reference signal, illustrating the advantages the x-y trace offers in detecting an ion acoustic wave in the presence of a fast mode.

As indicated above, the coupling for a grid driving an ion acoustic mode is poor, involving indirect effects such as nonlinearity in the sheath region, as opposed to the more direct coupling to be expected for electron plasma waves where the electric field is a more important part of the motion. However, experiments in other plasmas have demonstrated excitation of ion acoustic waves by grids or similar electrodes,[3,5-8] and calculations have been done to show mecnanisms for the coupling to the waves.[9-12] In this experiment various biased and

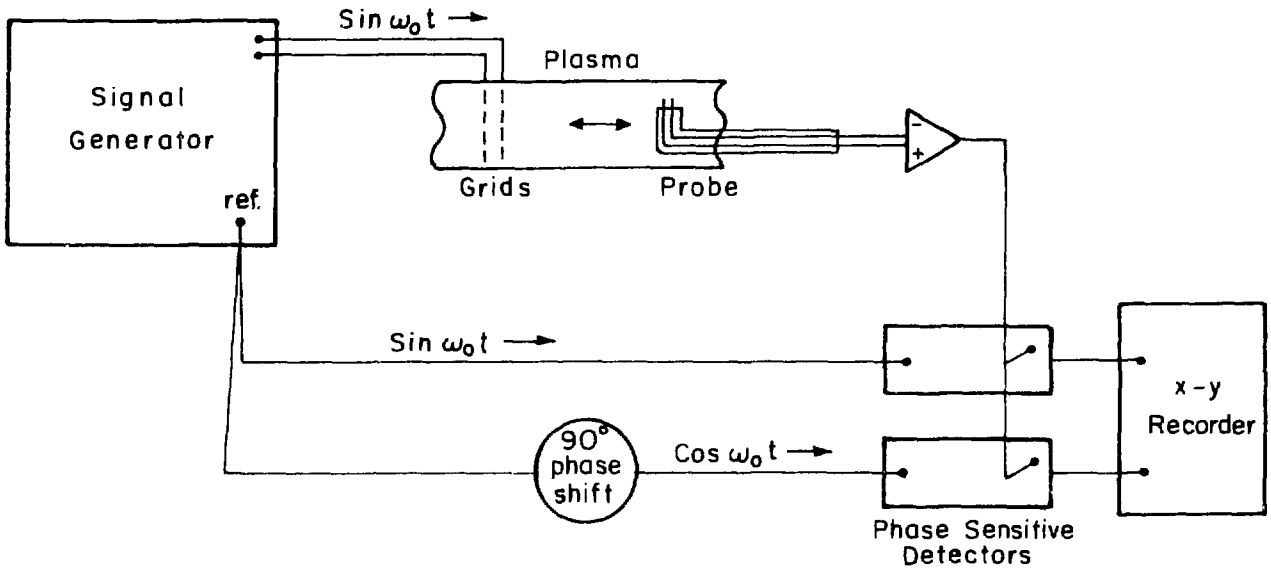

Figure IV.4 Schematic of an interferometric measurement of wave propagation from grids to a movable probe. As the probe is moved, the x-y recorder traces a curve representing real and imaginary parts (in-phase and quadrature components) of the probe signal as a function of probe position. The result is a complex phase diagram such as the example shown in Fig. IV.5 (a).

Figure IV.5 Comparison of two techniques of displaying probe response to two interfering modes excited by the grids. In (a) an x-y recording obtainable with the configuration shown in Fig. IV.4 is simulated. Each point on the curve represents the amplitude and phase of the probe signal (indicated for point 3 by the solid arrow or phasor) corresponding to a probe position. The interference between the two modes (a fast mode and a slow one) propagating to the probe to produce the signal are indicated for point 3 by the dashed phasors. In this example, if the probe was moved a total of 2 cm, we can conclude the wavelength of the slow mode is about 1 cm, because its phasor has made about two full turns in tracing the curve in (a). In (b) oscilloscope traces which would be obtained for probe positions corresponding to points 1 through 4 in (a) are indicated by the same numbers. The interferometric technique provides considerably clearer indication of the presence of a slowly propagating mode in addition to the fast mode.

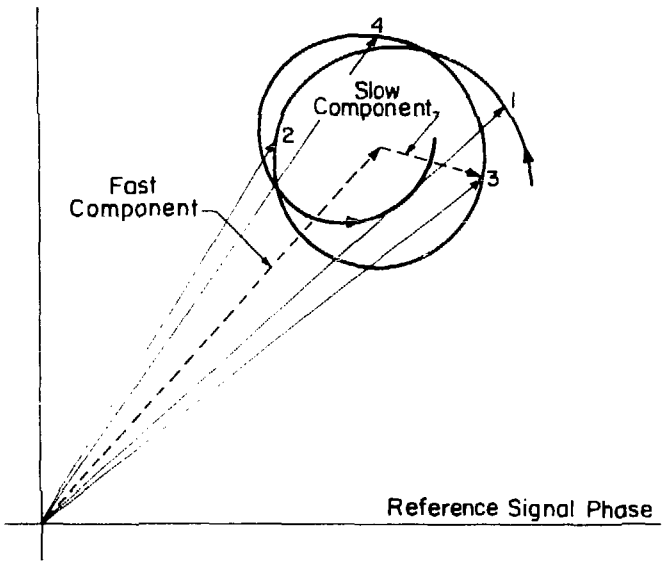

(a)

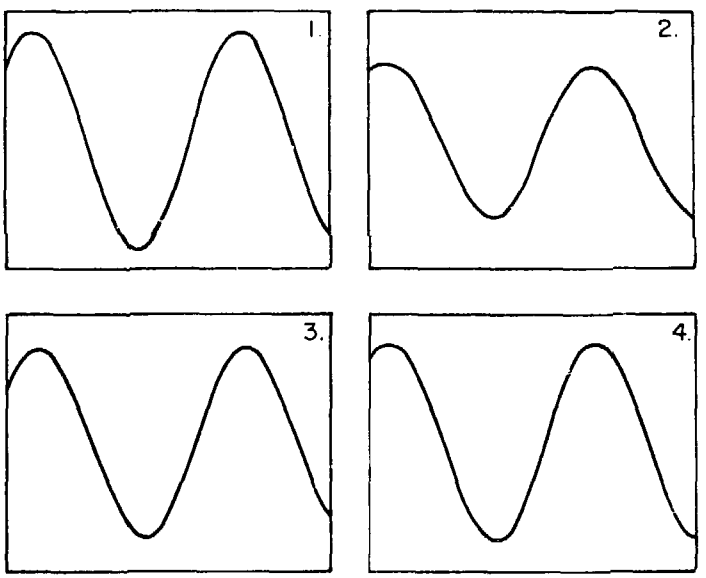

(b)

XBL 803-4917

Figure IV.5

unbiased grids were tried, including an insulated grid suggested by the work of Chen and Schott.[8] No suitable wave was found, although some inconsistent results showed possible generation of one at the second harmonic of the driving frequency. The wavelength involved (about 3 cm) would have been too long to be useful in testing TBS on this plasma.

Helium was substituted for argon in the discharge, and a more quiescent discharge resulted when the gas pressure was kept below a threshold pressure found for onset of striations. A new glass tube having a side arm with a fitting for insertion of probes was used. A pair of probes, side by side, 2 mm apart, in a cylindrical holder, can be inserted radially into the discharge through the side arm, as shown in Fig. IV.6. They can be rotated so that their separation is along or across the axis of the tube.

The He discharge was run at gas pressures of about 100 to 200 mTorr and currents up to about 1 amp. The electron temperature range, from probe traces, appeared to be about 5 to 7 eV.

Comparison of the fluctuations picked up by the radial and axial probes indicated the presence of waves traveling toward the anode at a relatively low frequency of about 1 MHz. Phase sensitive detection techniques could not be used with these spontaneous waves, as there is no well-defined reference signal. Observations of the relative arrival time of fluctuations at the probes using a dual beam oscilloscope showed a delay in arrival as a function of probe separation from which a group velocity of about $9 \pm 1 \times 10^5$ cm/sec in the anode direction can be deduced. The speed is similar to the ion acoustic

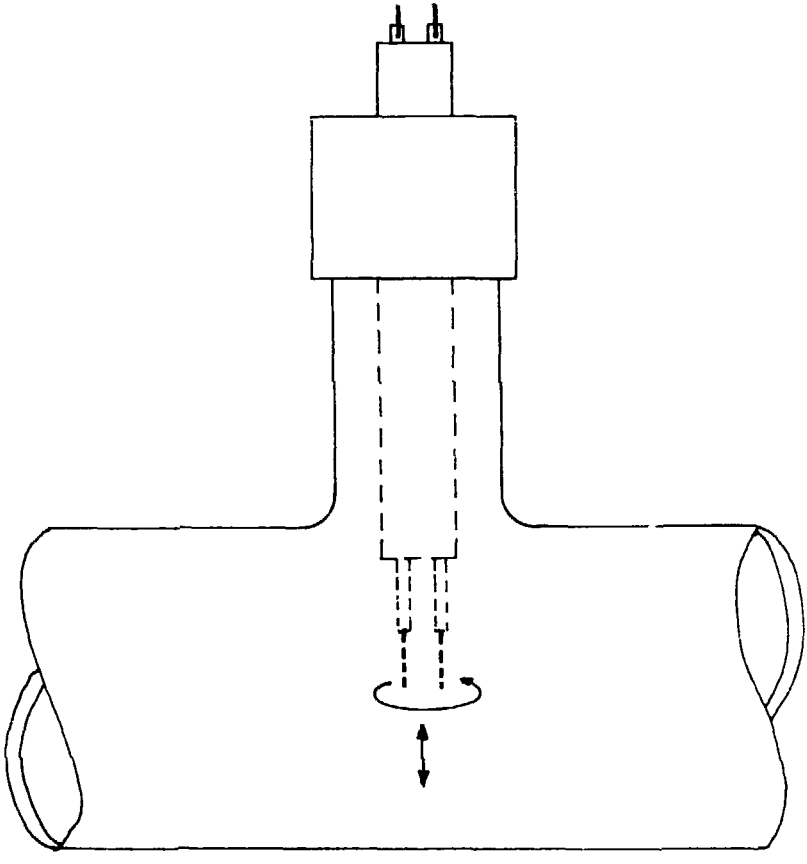

XBL803-4920

Figure IV.6 A schematic of the provision for twin radial probes.

speed of about 1.3×10^6 cm/sec in the ion rest frame. The ion drift, which reduces the apparent wave speed in the laboratory frame, can be estimated from the discharge parameters as approximately 9×10^4 cm/sec.[13]

A light detector using an SGD 100A photodiode to observe a small region (about 0.5 cm diameter) of the plasma gave similar measurements of the waves and confirmed that the emission light intensity is modulated by the fluctuation in the plasma. Although the roughly 1 cm wavelength involved was not as short as desired, it appeared this should be detectable using TBS.

More detailed measurements of the nature of the waves resulted from probe measurement techniques developed in connection with the TBS measurements, and these will be discussed in the next section.

B. Test of the Prototype TBS System

1. TBS Apparatus. Based on the information obtained in the preliminary investigation of the plasma, I designed and built a prototype TBS system, starting with the interferometer, which determined specifications for the rest of the optics and the detector. According to measurements made with the SGD 100A diode light detector, the most prominent lines in the He emission spectrum of the discharge were the 1.083 μm 2p to 2s and the .5876 μm 3d to 2p transitions, with the infrared line the stronger in terms of photocurrent detected. The availability of a commercially made polarizing beamsplitter for an infrared laser line at 1.06 μm (close enough to work with the He infrared line) influenced the choice of that line for the TBS experiment. The quantum efficiency of silicon detectors like the SGD 100A photodiode can be 25% or more, which offers fairly good performance. There are disadvantages to silicon detectors involving their bandwidth and

its effect on signal-to-noise performance (to be discussed later).

INTERFEROMETER The interferometer consists of the beamsplitter (with compensating wedge), a one-inch cube with a multilayer dielectric coating on the diagonal, and two front-surface mirrors (using gold coatings for efficiency in the infrared)--all with individually adjustable mounts on a one-inch thick aluminum slab. The slab also holds the analyzer optics and detectors, and mounts to an optical bench carrying the optics for the input system. Figure IV.7 is a schematic of the interferometer as seen from above. The mounts provided three-point support with screws for adjusting position and rotation or tilt. There was also provision for some freedom to slide along the base with the idea of giving an adjustment of translation without rotation, but in practice this was only useful for initial positioning, and final alignment is done with the screw adjustments.

The basic operation of the interferometer is discussed in Appendix A. The compensating wedge is needed because of imperfections in the beamsplitter angles. Due to small errors in the angles between faces of the two halves of the beamsplitter and some misalignment when they were cemented together, there is about a 5 milliradian angle between one exit face of the beamsplitter and the image of the other (reflected by the beamsplitting surface). As a result, the beamsplitter is equivalent to an ideal beamsplitter with an added wedge of glass between where the exit face is and where it should be. One can show that the effect of such a wedge is a rotation about the axis formed by the vertex of the wedge. The combined rotation of this unwanted wedge, the compensating wedge, and the mirrors must be a rotation about an axis parallel to the plane of the beamsplitting

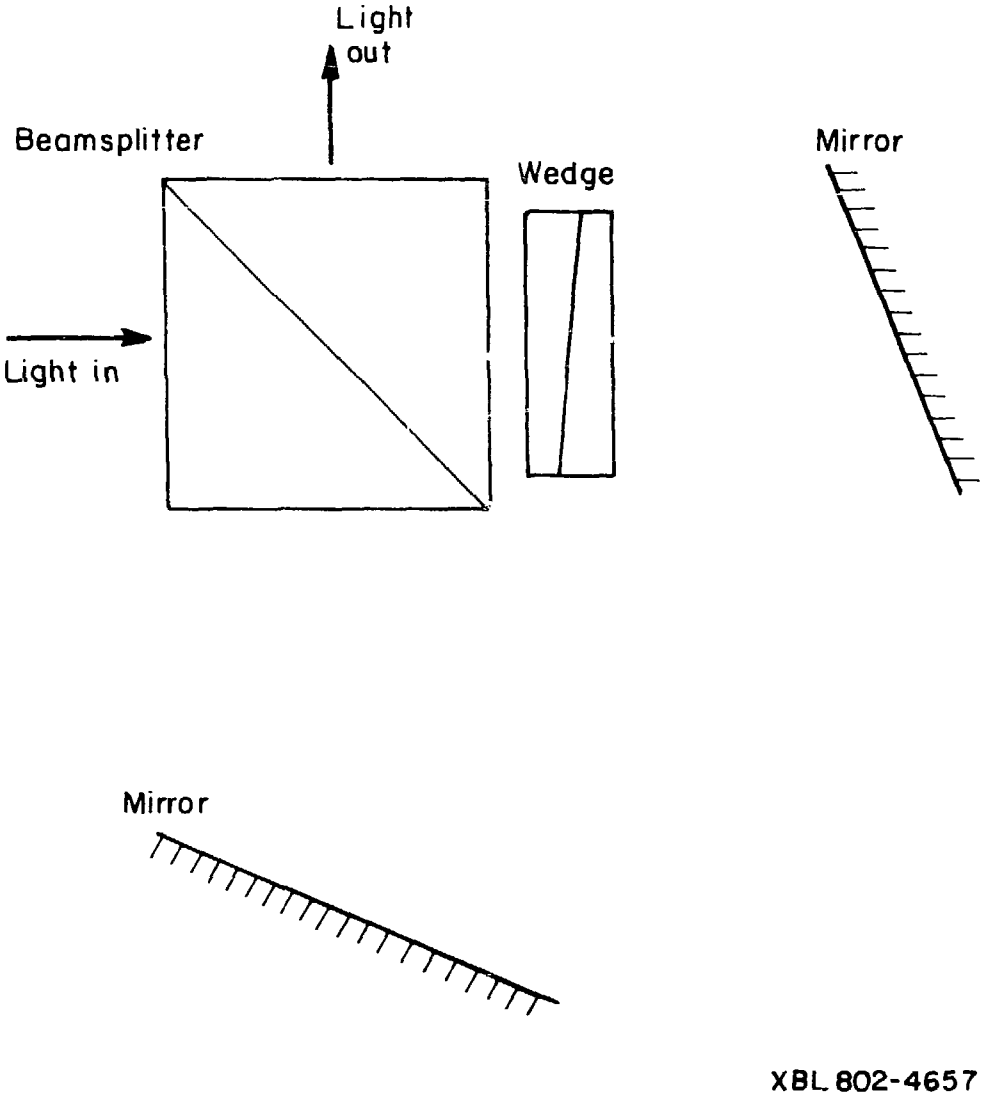

Figure IV.7 Interferometer schematic showing adjustable compensating wedge. Details of the operation of this type of interferometer are given in Appendices A through C.

surface to avoid the undesirable rotating interference fringes explained in Appendix C. The compensating wedge is used because without it correction of the beamsplitter error uses up one too many degrees of freedom of the interferometer. The fringes are stationary, but only if they are tilted a certain way.

The useful aperture of the beamsplitter is 2 cm. For the total optical path length of the interferometer with the compensating wedge as the components are now mounted, a combination of a 1 cm aperture with a $\pm 2^{\circ}$ range of acceptance angle without vignetting gives the best light acceptance. In order to view a 5 cm (about 5 wavelengths) length of the plasma, the range of acceptance angle demands that the focal length of the input optical system be 71.6 cm. A 52.7 cm focal length lens collimates the light from the plasma before it passes through another 1-inch beamsplitter used as the initial polarizer. Then the light is relayed to the interferometer by a telescope consisting of 26.0 cm and 35.1 cm focal length lenses, which are chosen so the combined focal length of the system is approximately the correct value. The two lenses of the telescope are used at a focal ratio of 1:9, while the 52.7 cm focal length lens is used at about the focal ratio of the system, 1:72. The three lenses are coated achromats and do not appear to have excessive aberrations.

The output system has a telescope which relays the light to a beamsplitting Glan Thompson prism of calcite through which the light passes to the two photodetectors, one for each polarization component. The telescope uses two coated achromats (focal lengths 4.5 and 10 cm). In the output system aberrations are not as important, however extraordinary mode propagation in the calcite beamsplitter would introduce

distortion of the plasma image if the light were not collimated when passing through. The telescope, beamsplitter, and detectors of the output system are mounted together in an assembly which can rotate about the axis of the output beam so that the angle of polarization can be adjusted without changing the alignment of the parts.

Initial adjustment of the interferometer was accomplished by using a helium-neon alignment laser to make sure the clockwise and counterclockwise paths overlapped and to check that the beamsplitter faces were aligned, using the reflected beams. In addition, the compensating wedge had to be adjusted in wedge angle and orientation (of the vertex or axis of rotation). The wedge angle adjustment involves rotating the two optically contacted pieces of glass making up the compensating wedge until the combined angle between the outer faces is correct.

Once approximate alignment is achieved, interference effects can be viewed with a detector removed because the polarizing beamsplitter (for $\sim$ 1.06 μm light) acts as a partially reflecting beamsplitter for visible light. Proper adjustment requires fringes of the appropriate spacing perpendicular to the propagation direction of the wave in the plasma. Also, the fringes must remain stationary as the observer moves his eye from side to side to take in the entire area of the beam that will fall on the detector. When the latter is not the case, it indicates the intersection of the planes of the two mirrors (the axis of rotation which the two mirror reflections form) is not parallel to the plane of the beamsplitting surface, or else orientation of the compensating wedge is incorrect. Tilting the top of a mirror forward or back will correct the alignment of the rotation axis, but the

orientation and spacing of the fringes will also change. Tilting the compensating wedge about the axis perpendicular to both the light path through it and the fringes provides a separate adjustment for the orientation of the fringes.

The extra degree of freedom thus available means the angle and orientation of the compensating wedge need not match the wedge of the beamsplitter exactly. Where a range of wavelengths may be involved, a for an achromatic interferometer, there may be problems with dispersion in the index of refraction of the glass if the errors are allowed to be too large. In this experiment such a problem exists when alignment is done using visible light (with the fringe spacing adjusted to take into account the wavelength difference) for a measurement to be made in the infrared. The test described below indicated in this case the problem was not too bad.

To provide a simulated wave a chopper was constructed by cutting 120 equally spaced slots, their width equal to half their spacing, near the edge of a disc of manila paper. The length of the slots is a small fraction of the diameter of the disc. The chosen spacing is in proper proportion to the size of the image of the plasma formed at the common focal plane of the two lenses forming the telescope in the input optical system such that the slots simulate a 1 cm wave in the actual plasma. The fact that the slots are not exactly parallel is not too important since the interferometer only looks at 5 wavelengths at a time. The disc is mounted to a motor so that the chopper, when placed in the position of the plasma image mentioned above and set rotating, will simulate a traveling wave (wavelength of 1 cm and frequency 3.56 KHz) by modulating the light from the plasma seen by the

interferometer. The chopped plasma light provided a strong signal which was useful for final adjustment of the interferometer alignment.

DETECTOR-AMPLIFIER AND DISCUSSION OF NOISE The detector-amplifier circuit is based on the SGD 100A photodiodes and a negative feedback amplifier using an LH0032 operational amplifier. Appendix D discusses the details of the design of the actual circuit. A simplified version diagrammed in Fig. IV.8 (a) illustrates the basic operating principles and noise sources.

The photodiode is reverse biased to operate in the photoconducting mode. The negative feedback amplifier causes the output current from the cathode to flow in the feedback impedance Z while permitting the cathode to "see" a much smaller impedance Z/A (where A is the amplifier gain), ideally a virtual ground. Figure IV.8 (b) shows the same circuit with the equivalent circuit of the diode added. A region around the junction is depleted of carriers by the bias voltage, leaving an intrinsic semiconductor where carriers are produced by photons (giving rise to the photoconduction current i_c) or by thermal excitation (giving rise to leakage current). The guard ring cathode intercepts surface leakage around the junction and shunts it to ground. The leakage resistance is so high that it has been neglected in the equivalent circuit except for the shot noise i_{ns} of the leakage current plus photoconduction current. Only the capacitance C_j across the junction between the undepleted regions is shown. The series resistance of the remaining undepleted material, the contacts, and leads is indicated by R_s. Also neglected is the impedance of coupling from the cathode to the guard ring.

Across the diode series resistance R_s is a noise source i_{nr} due to the thermal noise of R_s. Since the inverting input of the amplifier

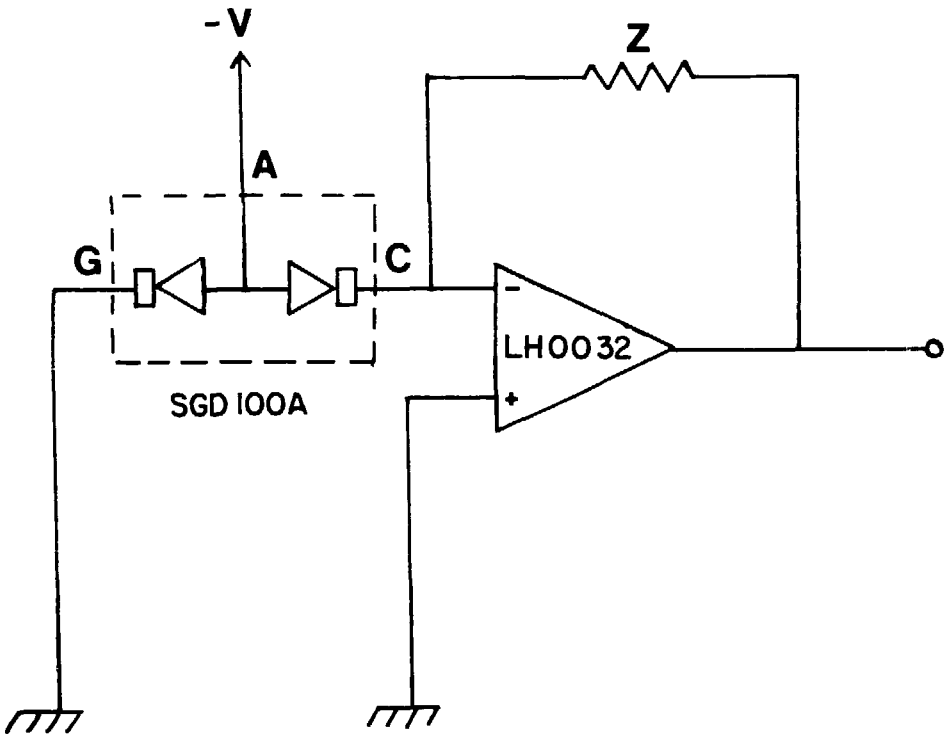

Figure IV.8 (a) Schematic of a simplified detector-amplifier circuit. (The actual circuit is given in Appendix D.) The SGD 100A photodiode consists of anode A, active cathode C, and guard-ring cathode G which surrounds the active cathode and collects excess leakage currents around the surface of the junction.

Figure IV.8 (b) Equivalent circuit of the simplified detector-amplifier [see Fig. IV.8 (a)]. The photoconduction current i_c and the shot noise current i_{ns} due to the fluctuations in the photoconduction plus leakage current appear across the junction capacitance C_j. Additional noise components are the thermal noise currents i_{nr} and i_{nf} of the diode series resistance R_s and the resistive component of the feedback impedance Z_f, respectively; and the amplifier input current and voltage noise i_{na} and v_{na}.

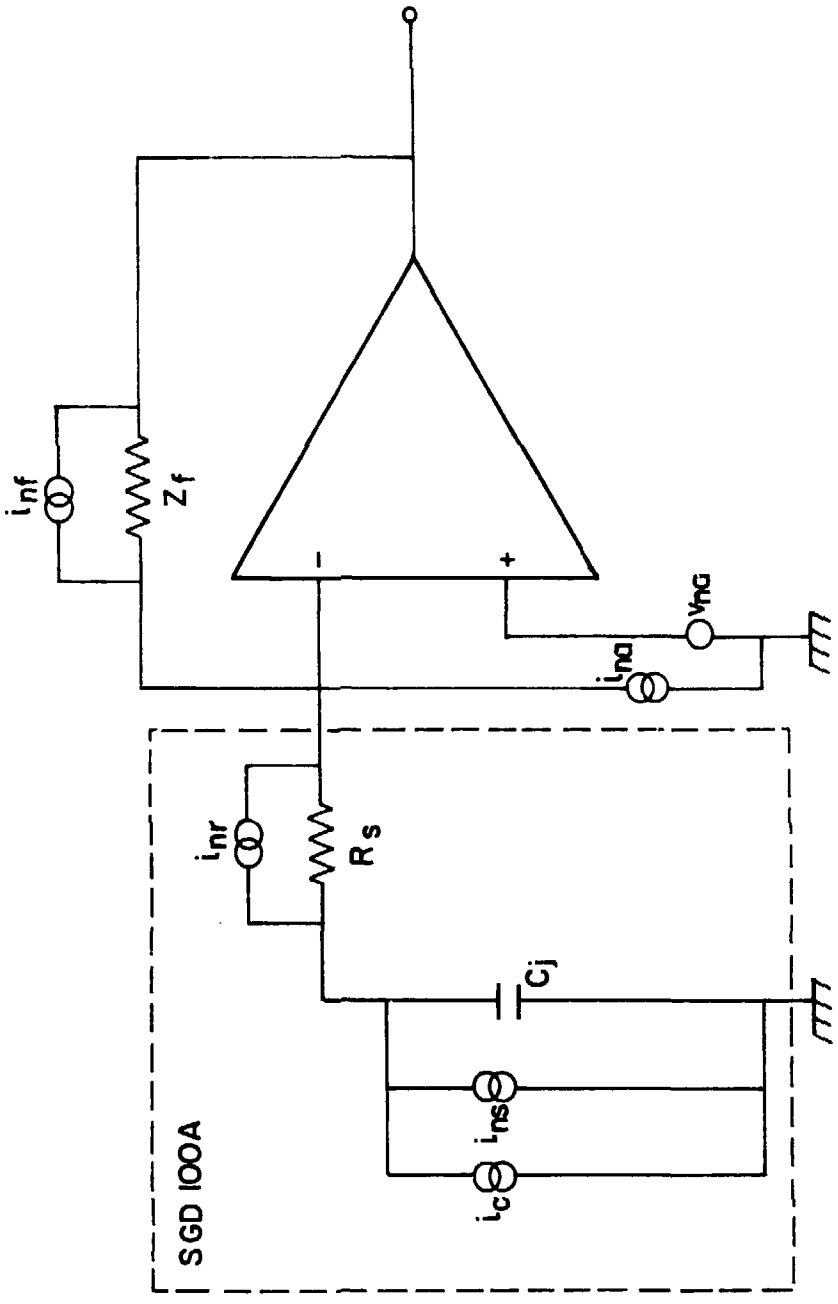

Figure IV.8 (b)

is virtual ground (current into this "summing point" flows in the feedback circuit, then via the amplifier to ground, without any voltage appearing at the summing point), the current i_{nr} is applied to R_s and C_j in parallel, with the portion flowing in C_j being:

$$i_{nr}\left(\frac{1}{R_s} + i\omega C_j\right)^{-1} i\omega C_j = \frac{i_{nr} i\omega\tau_D}{1 + i\omega\tau_D} \qquad \text{(IV-1)}$$

(where $\tau_D \equiv R_s C_j$, ω is the frequency in radians/sec, and i without a subscript is the square root of -1). It does so by flowing into the summing point of the amplifier. Similarly, that portion of the photoconduction current and shot noise current which flows in R_s

$$(i_c + i_{ns})\left(\frac{1}{R_s} + i\omega C_j\right)^{-1} \frac{1}{R_s} = \frac{i_c + i_{ns}}{1 + i\omega\tau_D}\,, \qquad \text{(IV-2)}$$

goes to the summing point of the amplifier. Thus we can represent the noise of the series resistance by a noise current $i_{nr} i\omega\tau_D$ in parallel with the photocurrent i_c and shot noise i_{ns}.

Treatment of the noise current i_{nf} generated by the thermal noise of the resistive components of the feedback impedance Z is straightforward. That current must all flow the same way it would if it were applied between the summing point and ground, instead of directly across Z, because the amplifier provides the path from ground to the other end of Z at the output in the process of maintaining the virtual ground at the summing point. Thus the equivalent feedback noise, if applied across C_j is

$$i_{nf}(1 + i\omega\tau_D). \qquad \text{(IV-3)}$$

Because the phase of the each source is random and statistically independent, the three noise currents discussed can be combined by summing their magnitudes squared. The result, after substituting the formulas for thermal and shot noise, is

$$i_N^2(\omega) = \{\frac{1}{\pi} e((i_c) + i_\ell) + \frac{2}{\pi} kT[\frac{Re(Z)}{|Z|^2} + \omega^2\tau_D^2 \frac{Re(Z)}{|Z|^2} + \frac{\omega^2\tau_D^2}{R_s}]\}, \quad \text{(IV-4)}$$

for the total equivalent noise power spectral density for positive frequency $i_N^2(\omega)$, where i_ℓ is the leakage current of the photodiode. From the form of the expression one can conclude it is desirable to minimize $Re(Z)/|Z|^2$ and τ_D^2 or τ_D^2/R_s, which in practice means using as large a feedback resistance as practical and minimizing junction capactiance and series resistance in the photodiode. The latter may be done by increasing the depletion depth at the expense of some increase in leakage, or by choice of photodiodes. The amplifier current noise has the same effect as noise due to the feedback resistance and would appear as excess noise over that calculated for an ideal resistance. The main effect of the amplifier voltage noise is found to be similar to the photodiode thermal noise because it depends upon the impedance of the diode shunting the amplifier input.

2. Data Acquisition and Analysis. The appearance of the waveforms of the probe fluctuations during the initial investigation using oscilloscopes indicated a fairly large frequency spread (Fig. IV.9). With a 5 cm length of the column analyzed for a 1 cm wavelength fluctuation, the expected resolution of the TBS measurement would be 20%. For an ion acoustic wave we expect

$$\Delta f/f = \Delta k/k, \quad \text{(IV-5)}$$

or a frequency spread of about 200 KHz for a wave near 1 MHz. Thus a substantial fraction of the fluctuation spectrum would be observed, but the wideband nature of that spectrum implies a low spectral density for a given $\langle(\delta n/n)^2\rangle$. Since the thermal noise in the photodiodes contributes more noise than the shot noise of the light, the

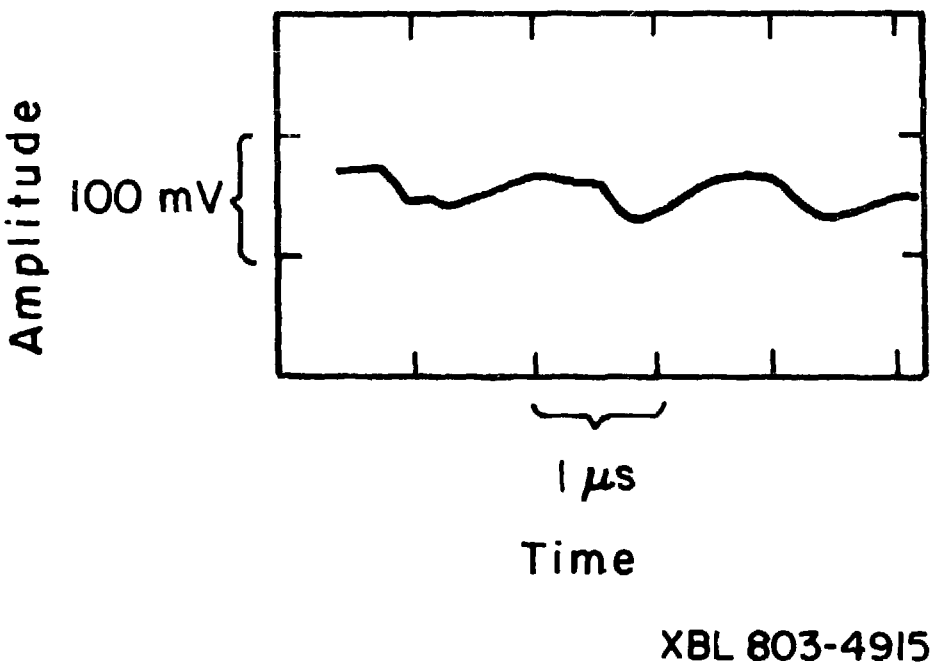

Figure IV.9 Probe fluctuation waveform. This figure is a reproduction of an oscilloscope trace of the twin radial probe signal obtained during initial investigation of the spontaneous fluctuations of the plasma.

measurement proposed is a difficult one.

To obtain the signal averaging suggested in the previous chapter, data was digitized and recorded by a Nicolet digital oscilloscope for transfer to a ModComp Systems computer. The fast analog to digital converter plug-in used with the Nicolet has a range of ±100 mV at maximum sensitivity with 8 bit or about 0.8 mV resolution. Sample rates up to 20 MHz are possible, but 5 MHz was the normal sample rate. The digital oscilloscope can record 4096 words, for a total length of .8192 msec when one channel is recorded at 5 MHz. Two channels may be recorded simultaneously for a length of .4096 msec. After a recording the data can be transferred to the computer in an adjacent building in about 11.5 sec. The computer saves the data on disc, and it can be copied onto magnetic tape for long-term storage.

A modified version of a program written by K.F. Schoenberg[14] manages the data transfer to disc, and can activate the Nicolet for another recording after each transfer. Thus, 90 recordings can be saved on the disc in about 17 minutes.

For signal averaging the program can then obtain the spectra of the recordings using an FFT algorithm and average the power spectra (auto power for single channel recordings, auto and cross power for dual channel recordings) of appropriate sets of recordings.

Use of the digital data recording and processing has certain practical limitations which are discussed by Schoenberg.[19] These are due to the effects of representation of a continuous signal by discrete, evenly spaced samples, the finite length of time during which the signal is sampled, and quantization of the signal amplitude (rounding measured values to a finite set of digital levels).

The first of these limitations is the aliasing of frequency components of the signal higher than one-half the sampling rate (a cutoff known as the Nyquist frequency). Errors due to aliasing must be limited by choosing a sufficiently high sampling frequency and filtering unwanted high frequency components of the signal before it is sampled.

The limitation due to the finite time length of the recording sets a lower bound on the frequency differences in the signal which can be resolved. To be resolved, two frequency components must differ by at least an amount equivalent to a total of one period over the sample time. Another interpretation is that the sample time must be longer than the correlation times of the signals of interest.

The effect of quantization can be interpreted as the addition of a spurious signal equal to the amount the analog signal amplitude has to be shifted in rounding it to the nearest digital level at each sample time. Such a spurious signal varies inversely as the number of levels available for quantizing the input signal. The effect on the spectra obtained by the FFT algorithm can be estimated approximately[16] by a signal-to-noise ratio which varies as the square of the number of levels used in the quantization of the signal amplitude, and inversely as the logarithm of the number of samples transformed. The lesson is that there should be adequate amplification of the signal prior to digitization such that the amplitude range of the digitizer is properly utilized.

With computer data analysis the probe measurements are now used to provide spectral density vs. wavenumber and frequency. The two radial probes are rotated so that their separation is along the axis,

and each is biased by a circuit as diagrammed in Fig. IV.10. The pair are connected via the same length of coaxial cable to a differential amplifier. The 50Ω cables are terminated at the amplifier with 50Ω loads. The difference in electron current drawn by the two probes produces a difference in voltage drop across the two 50Ω cable terminations, which is then amplified by the differential amplifier. The amplifier gain is 10, and its output is connected to one channel of the Nicolet with ac coupling. The other channel is connected via terminated 50Ω cable to the axial probe. AC coupling is also used when fluctuation measurements are to be made. The dc voltage representing the unperturbed bias current is also checked for comparison with the fluctuation levels. Figure IV.11 is a schematic of the connections for probe cross-power measurements.

Use of the two radial probes in differential mode reduces response to fluctuations with wavelengths large compared with twice the radial probe spacing along the axis of the tube. If we assume a wave in the form of a density fluctuation

$$\frac{\delta n}{n_o} = \frac{n_1}{n_o} e^{i(kz-\omega t)}, \qquad \text{(II-6)}$$

where z is the position along the axis of the tube, then we anticipate proportional current fluctuations in the probe bias:

$$\frac{\delta V_{\pm}}{V_{dc}} = \frac{\delta I_{\pm}}{I_{dc}} \exp\left[i\left(\pm\frac{k\Delta z}{2} - \omega t\right)\right], \qquad \text{(IV-7)}$$

where the origin of z is chosen so that the probes are located at $\pm\Delta z/2$. The difference signal is then

$$\frac{\delta V_{+}}{V_{dc}} - \frac{\delta V_{-}}{V_{dc}} = 2i \frac{n_1}{n_o} e^{-i\omega t} \sin\left(\frac{k\Delta z}{2}\right). \qquad \text{(IV-8)}$$

The common mode signal is

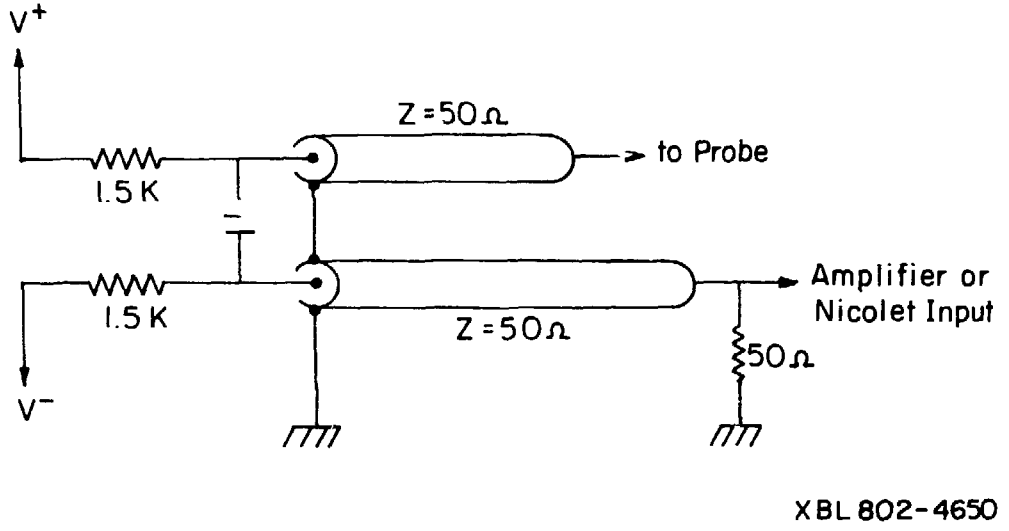

Figure IV.10 Schematic of probe bias circuits. Each of the twin radial probes and the axial probe is biased by a circuit as diagrammed here. The voltage at the 50Ω cable termination is proportional to the probe current, including the direct current and fluctuating components.

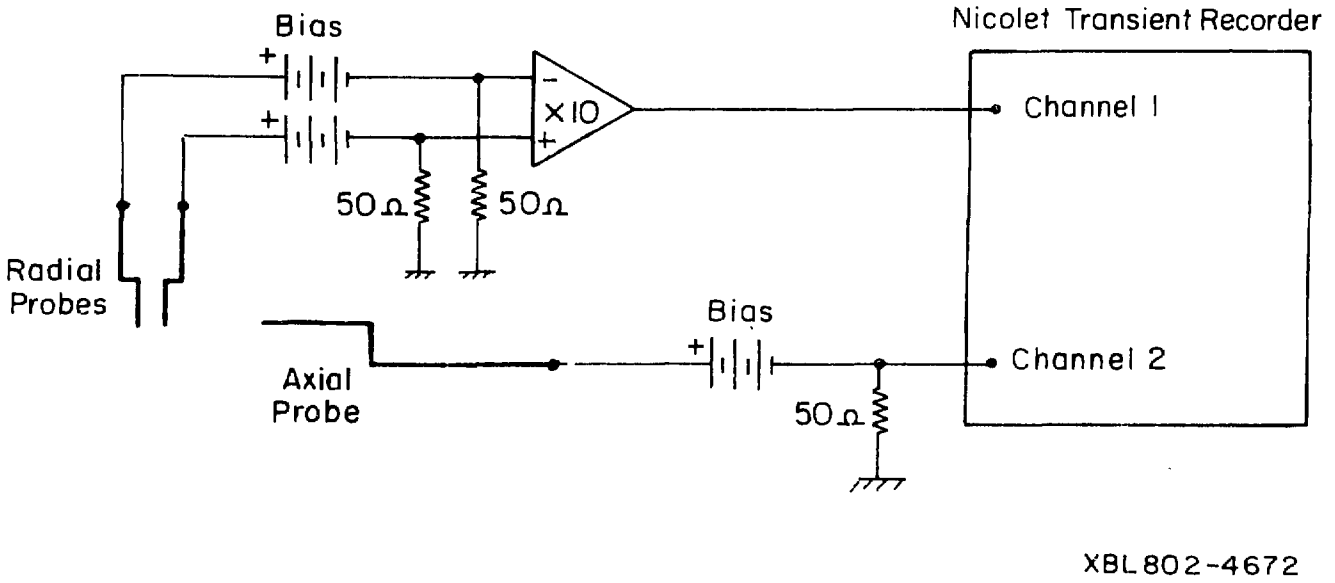

Figure IV.11 Schematic of connections for probe cross-power measurements. The bias voltages actually represent bias circuits as shown in Fig. IV.10.

$$\frac{1}{2}\left(\frac{\delta V_+}{V_{dc}} + \frac{\delta V_-}{V_{dc}}\right) = \frac{n_1}{n_o} e^{-i\omega t} \cos\left(\frac{k\Delta z}{2}\right). \qquad \text{(IV-9)}$$

At the differential amplifier output, this last signal is reduced by the common mode rejection ratio of the circuit β_{cm}. The normalized response, in terms of rms fluctuation voltage level at the output to dc output level with one probe input grounded, is then

$$\left(\frac{\delta V_{out}}{V_o}\right)_{rms} = \frac{n_1}{n_o} \times 2\left[\sin^2\left(\frac{k\Delta z}{2}\right) + \frac{1}{4}\beta_{cm}^2 \cos^2\left(\frac{k\Delta z}{2}\right)\right]^{\frac{1}{2}}. \qquad \text{(IV-10)}$$

The cross power spectral density vs. separation of the axial and radial probes is obtained as follows. The computer is used to obtain recordings from the digital oscilloscope of the differential radial probe signal and the axial probe signal (as discussed above) simultaneously. In between recordings the probe separation is changed in .5 mm increments until recordings are accumulated for a range of about 1.5 cm or more. Later the cross power spectra are computed for each recording.

From the probe cross power spectra vs. separation of the radial and axial probes the cross power vs. wavenumber k and frequency ω is obtained by spatial Fourier transform for each frequency component. First the spectra are smoothed by a Gaussian window applied to the cross correlation function obtained by transforming the cross power spectrum from frequency to time, and then transforming back. The process is equivalent (by the convolution theorem) to averaging together adjacent frequencies with a Gaussian weighting factor, the transform of the Gaussian time window. Thus the shorter the range of times retained in the correlation function, the wider is the bandwidth of the frequency filter simulated.

The spatial Fourier transform is performed upon the smoothed cross power spectra for each of a selection of frequencies, and the phase of the resulting spectral density vs. wavenumber and frequency is discarded since the zero of probe separation and the relative phase shift in the two probe circuits are uncertain. Figure IV.12 is a display of the amplitude of the spectral density obtained vs. k and ω. It is composed of plots of spectral density vs. k for each value of ω, with the origin shifted along the direction representing the frequency axis by an amount proportional to the change in frequency. To help clear up confusion caused by the curves overlapping, they have been plotted twice, with the frequency axis shifted to simulate the parallax effects of viewing from slightly to the side. One should visualize the curves for higher frequencies as being further away. Thus, in the version to the right, they appear closer to the lefthand side of the picture. With a little practice, some readers should be able to view this figure in stereo by the crossed eyes method[17] (described in Appendix E), greatly simplifying the visualization of the information contained. (By placing the explanation in Appendix E, the author hopes to reduce the temptation for those who fear the effort may reward them only with Eyestrain.)

If there is a single type of wave with a well defined relation between frequency and wavenumber, each curve in the frequency range where the wave is excited should have a well defined maximum at $k(\omega)$ of the wave. The shape of the curve results from the effects of sampling the wave at a finite set of discrete axial probe positions as discussed above. Here one should note that the FFT algorithm was not used, and more points in wavenumber space are plotted than are actually independent according to the sampling done. A dispersion relation of

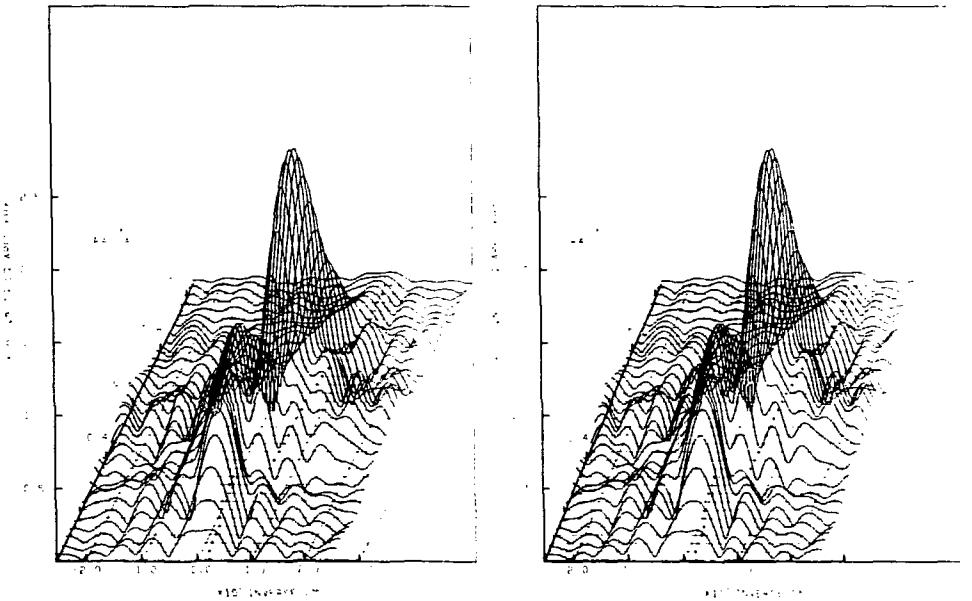

XBL 802-8162

Figure IV.12 Probe cross power spectral density vs. frequency and wavenumber with discharge conditions 140 mT He pressure and 1.0 A discharge current. In this and the following eight cross power spectral density plots, curves of spectral density vs. wavenumber are plotted for several frequencies with the origin displaced in proportion to the frequency. The two images shown provide slightly different views to help distinguish different curves by stereo viewing as explained in Appendix E, or by comparing the apparent parallax.

sorts is plotted on the k,ω plane by locating the position of the most prominent maximum for each frequency. This procedure is questionable for frequencies where two incompletely resolved modes $k(\omega)$ appear.

3. Procedure and Results. In the course of this experiment, numerous pitfalls were uncovered, and refinements were made. This section describes the present (latest) procedure and the current state of the attempt to measure the waves by TBS. In the final chapter improvements are suggested that were not possible to incorporate, and possibilities for applications of TBS are considered in light of the experience gained.

The discharge was run with background gas pressure usually about 145 mTorr, discharge current 1 amp, and anode at about 85 V. The anode position for these conditions was 20 cm from the cathode assembly. I found the behavior of the discharge to be fairly steady and repeatable, with the exception of two problems that tended to develop after the plasma had been on an hour or so. First, the discharge supply output tended to drop slowly and had to be adjusted occasionally until finally it could be adjusted no further. This was probably due to a gradual temperature rise in the transformer or the choke, as there did not seem to be an associated change in anode voltage. The other problem was that the character of the fluctuations would eventually change, with the slow, ion-acoustic-like mode finally disappearing. This change appears to be associated with the discharge tube cleaning itself by ion bombardment of the walls. Reinforcing this interpretation is the fact that the change also occurred early in a run started only a few hours after a previous one, so that the liquid nitrogen

trap had not warmed up completely.

Thus, there was apparently a period of about 30 to 40 minutes (after turning on and adjusting the discharge and making initial tests and settings of the equipment) available for recording data from the interferometer and probes, during which time it could be assumed that the behavior of the wave would not change too much. It was then necesary for the discharge to be turned off and left alone for a day or more. The diffusion pump was allowed to cool, the trap to warm up, and the discharge apparatus to reach a sort of steady state before it was operated again.

The data taking procedure eventually developed is as follows. The discharge is started and initial adjustments of the conditions (pressure and current) are made. Checking and adjustment of the interferometer takes a few minutes, winding up with a test of the response level to the plasma light with the chopper. This period of time also allows the discharge conditions to stabilize, requiring some checks and adjustments of the current and pressure. A set of signal recordings is made using the computer to operate the Nicolet digital oscilloscope and save the data. The time allowed is enough to save 90 recordings of the output of the interferometer detector-amplifier, check the response to the chopper afterward, and then switch to the probes and take about 35 recordings for probe cross power spectra at successsively larger probe separations. The switch to the probes requires changes in the settings of the Nicolet and note taken of the probe bias conditions in addition to the changes in connections. During the data taking time spot checks are made on the discharge conditions, and occasional small discharge current

adjustments (of about 20 mA out of 1 A) are necessary.

For comparison, noise spectra for the detector-amplifier without the plasma light are obtained from recordings of the output made before and after running the discharge. In earlier trials, comparison recordings were made during the run by blocking the light to the interferometer for some recordings, or varying the orientation of the polarizing beamsplitter in the input system between recordings. Unfortunately, this procedure exacerbates the problem of obtaining enough recordings for data averaging in the time required for data transfer over the present computer link. This is one of the areas of improvement to be discussed in the final chapter.

Sample rates used were 2 MHz or 5 MHz for the interferometer data, and 5 MHz for the probe data. The perturbation due to the probes is sufficient to cause the discharge conditions to vary somewhat with probe position. The effect on the wave spectrum will be discussed below. To make the comparison of probe and spectroscopy data more valid, the probe position is varied during the taking of the spectroscopy data similar to the way it is varied for the probe data.

PROBE RESULTS Figures IV.12 through IV.15 are spectral density plots from probe data taken during four separate test runs with the TBS system. To interpret the results obtained for the TBS, we must first analyze what the probe data tells about the waves present during the test. Stereo viewing reveals the two most prominent features to resemble ridges, with one dominant in the foreground in the frequency range from about 10^6 to 3 x 10^6 radians/sec, near zero wavenumber. The one toward the background is most prominent in the 4 - 9 x 10^6 radians/sec frequency range, where it varies from 5 to 10 inverse cm

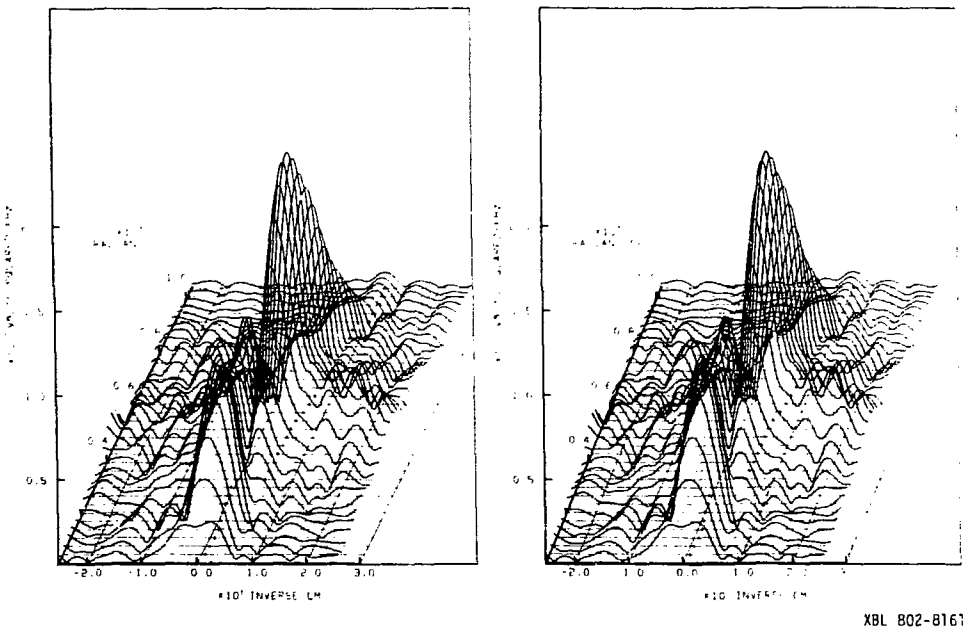

Figure IV.13 Probe cross power spectral density vs. frequency and wavenumber for a measurement repeating the conditions of Fig. IV.12. (The two images provide different perspectives for stereo viewing as explained in Appendix E.)

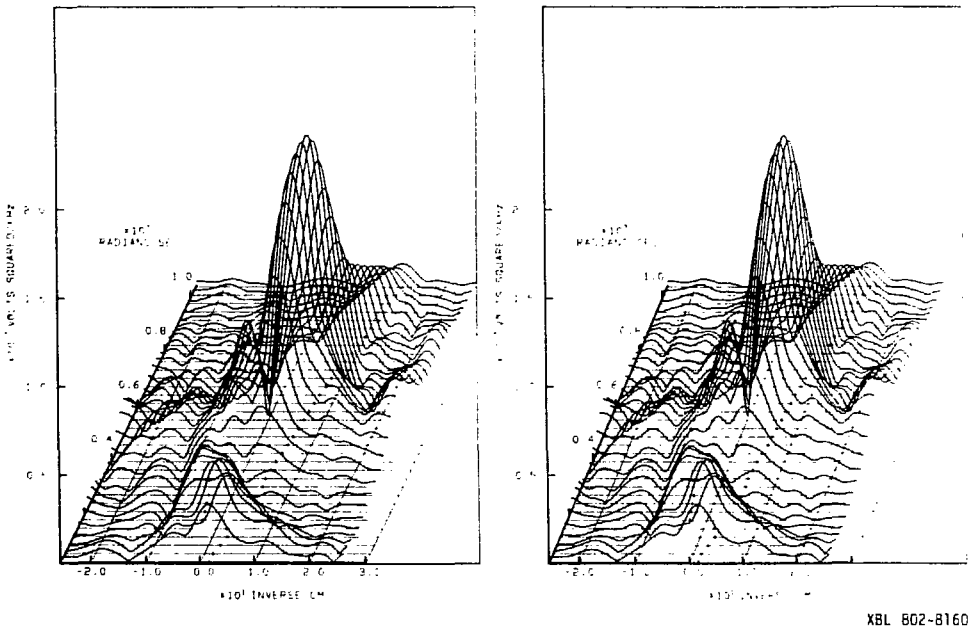

XBL 802-8160

Figure IV.14 Probe cross power spectral density vs. frequency and wavenumber with discharge conditions 165 mT and 1.1 A discharge current. (The two images provide different perspectives for stereo viewing as explained in Appendix E.)

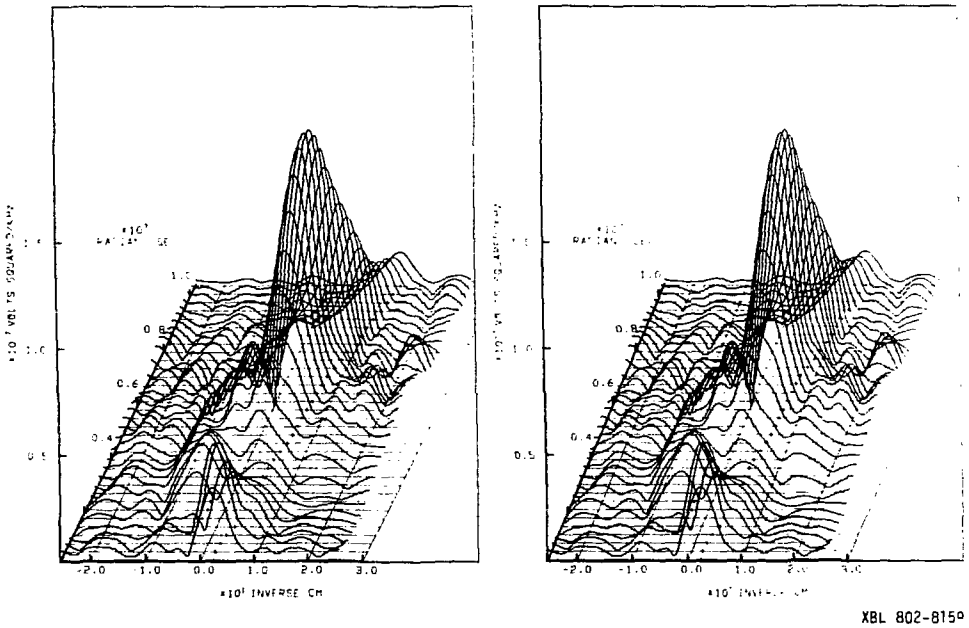

Figure IV.15 Probe cross power spectral density vs. frequency and wavenumber for a measurement repeating the conditions of Fig. IV.14. (The two images provide different perspectives for stereo viewing as explained in Appendix E.)

in wavenumber. In the region of about 3 - 5 x 10^6 radians/sec overlap occurs, and both ridge lines can be followed for a while although the computer program only plots the position of the most prominent maximum at the base. (The horizontal baselines indicate the frequency axis for each curve plotted.)

Apparently, there are two modes $k(\omega)$ present for an overlapping range of frequencies. They appear to have the general characteristics found in the initial observations discussed in the first part of this chapter. One is a small k, or fast mode, and the other resembles an ion acoustic wave with a speed of about 10^6 cm/sec. Because of the differential measurement of the twin radial probe response, we can expect that the measured spectral density for the fast mode is considerably smaller than the actual value [see Eq. (IV-10)].

Since two modes are present, the preliminary measurements of amplitude and speed of the slow mode were probably hampered by interference effects. Even the present measurements do not have sufficient resolution to prevent errors near the frequency range of overlap. For comparison, simulated probe data representing two modes of similar amplitudes, with various wavenumber separations, are analyzed and displayed using the same technique (Figs. IV.16 - IV.20). One mode has zero wavenumber and constant amplitude, while the other is displayed for various wavenumbers, with amplitude increasing from near zero at high and low frequencies, to a peak amplitude equal to that of the first mode in the middle of the frequency range. Where only the first mode is significant, we can see the effect of the finite range L of probe separations "sampled" in the width of the $k(\omega)$ vs. ω curves, and in the side lobes present. The range was chosen to be representative

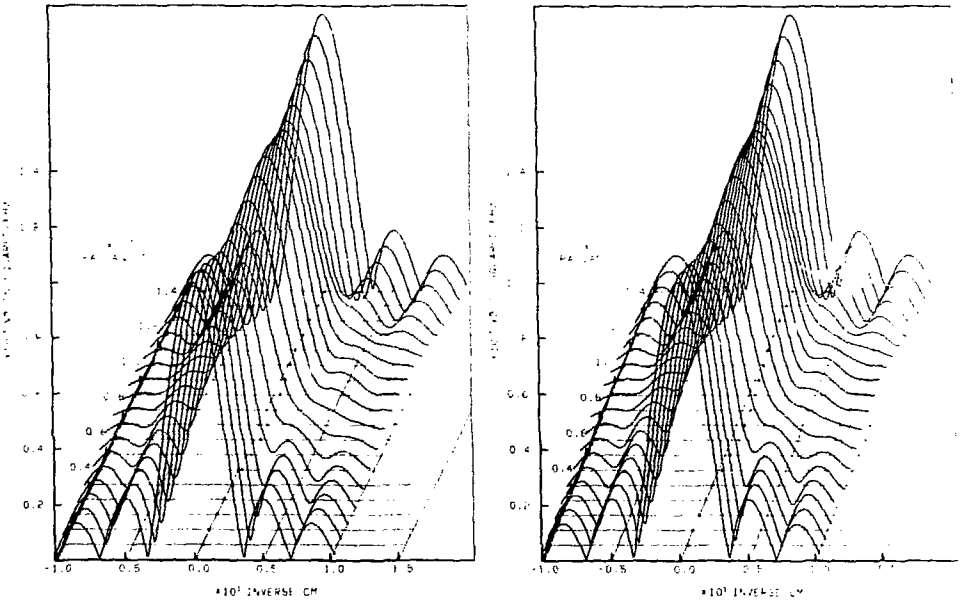

XBL 802-8165

Figure IV.16 Simulated probe cross power spectral density vs. frequency and wave number. This plot simulates two modes separated by a wavenumber difference Δk of 1.2 cm^{-1} One mode is at zero wavenumber with constant amplitude, while the other is at 1.2 cm^{-1} with a frequency-dependent amplitude. The amplitude of the second mode in this figure and the following four plots varies from zero at the low and high frequency ends to an amplitude equal to the other mode in the middle of the frequency range in a sinusoidal fashion. (The two images provide different perspectives for stereo viewing as explained in Appendix E.)

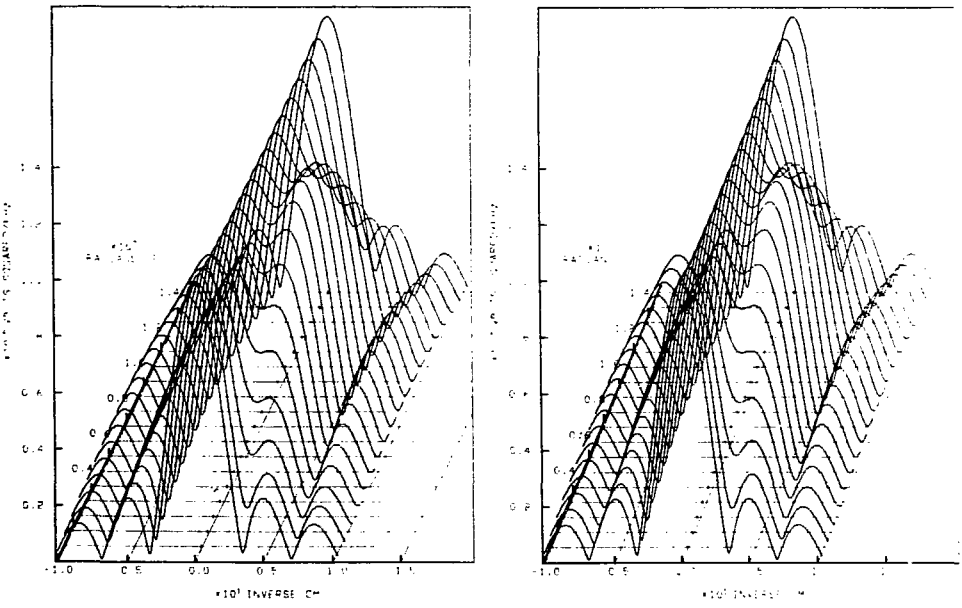

XBL 802-8164

Figure IV.17 Simulated probe cross power spectral density vs. frequency and wavenumber for two modes separated by 2.4 cm^{-1}. One mode has a constant amplitude and the other has a frequency-dependent amplitude, reaching a peak equal to the first mode. (The two views provide different perspectives for stereo viewing as explained in Appendix E.)

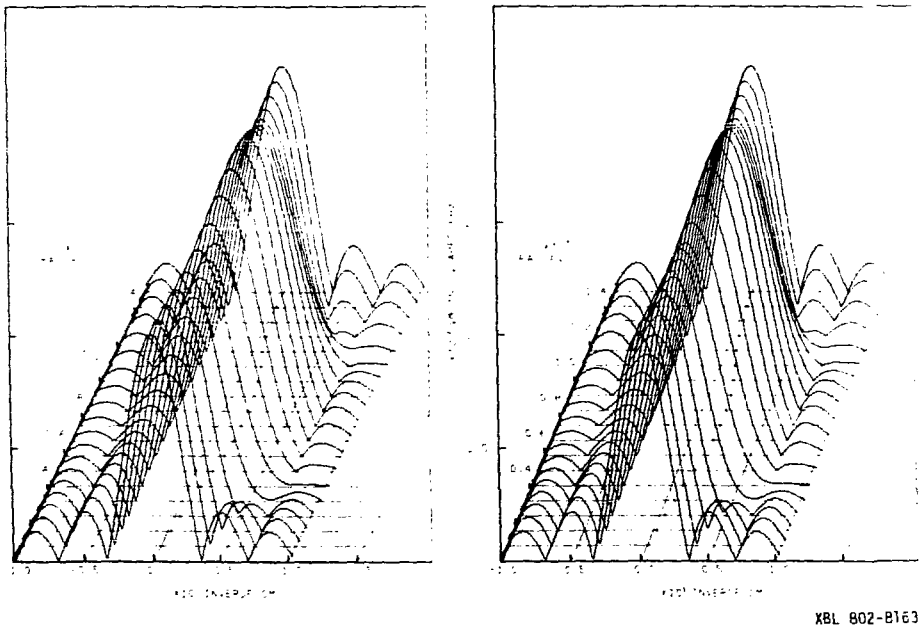

XBL 802-8163

Figure IV.18 Simulated probe cross power spectral density vs. frequency and wavenumber for two modes separated by 3.6 cm^{-1}. One mode has a constant amplitude and the other has a frequency-dependent amplitude, reaching a peak equal to the first mode. (The two images provide different perspectives for stereo viewing as explained in Appendix E.)

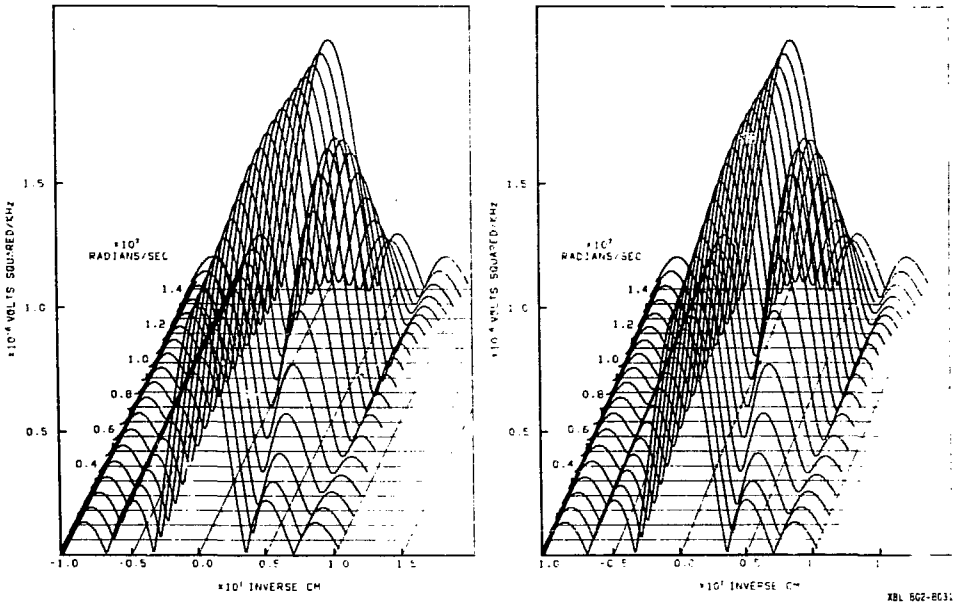

Figure IV.19 Simulated probe cross power spectral density vs. frequency and wavenumber for two modes separated by 4.8 cm^{-1}. One mode has a constant amplitude and the other has a frequency-dependent amplitude, reaching a peak equal to the first mode. (The two images provide different perspectives for stereo viewing as explained in Appendix E.)

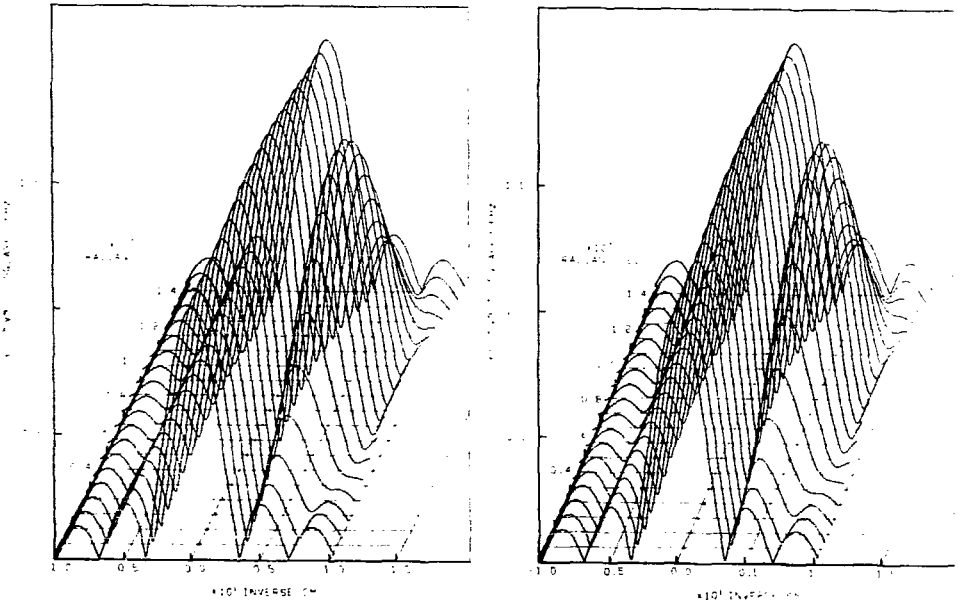

XBL 802-8166

Figure IV.20 Simulated probe cross power spectral density vs. frequency and wavenumber for two modes separated by 6.0 cm^{-1}. One mode has a constant amplitude and the other has a frequency-dependent amplitude, reaching a peak equal to the first mode. (The two views provide different perspectives for stereo viewing as explained in Appendix E.)

of the range of measurements for Figs. IV.13 - IV.15. Figure IV.12 is obtained from probe data covering a smaller range of separations, so that a change in k scale (by the ratio of the separation ranges) is appropriate for comparison with Figs. IV.16 - IV.20.

The general appearance of the spectral density plots in Figs. IV.12 - IV.15 is quite similar, especially with regard to the shorter wavelength feature of interest for TBS. The amplitude of the peak (note the change in vertical scale from plot to plot) ranges from about 1.5×10^{-7}/KHz (after normalization for dc probe conditions) for the first plot down to 7×10^{-8}/KHz for the last. For the last two plots the discharge conditions were changed somewhat by increasing the current and background gas pressure to see what the effect might be on the fluctuations. The long wavelength mode seems somewhat less prominent, while the peak of the short wavelength mode is shifted slightly to higher frequency and wavenumber. Table IV-1 is a summary of the characteristics of the spectral density peak obtained from these plots.

As mentioned earlier, variations in the behavior of the discharge as a function of the axial probe position were noted. Some effect on measurements of the fluctuation spectral density are to be expected because of this perturbation of the plasma by the probe. Such an effect may be reflected in the width in k of the spectral density curves, which is greater than the width for the simulated fluctuations with well-defined wavenumber. The excess wavenumber spread of the measurements might also reflect an actual spread in the spectral density of the fluctuations, implying a decreased correlation length due to turbulence or spatial growth (or damping). Ilić, Harker, and

TABLE IV-1: Characteristics of the Maximum in Spectral Density

Plot	Discharge		Spectral Density (KHz^{-1})	Position		Wavenumber Spread (cm^{-1})
	pressure (mTorr)	current (Amp)		frequency (KHz)	wavenumber (cm^{-1})	
IV-12	140	1.0	1.5×10^{-7}	840	5.6	6.0
IV-13	140	1.0	1.3×10^{-7}	840	5.0	6.0
IV-14	165	1.1	1.4×10^{-7}	880	6.2	7.6
IV-15	165	1.1	7×10^{-8}	930	6.2	7.0

Crawford[18] have made similar spectral density measurements of ion acoustic turbulence in a positive column which suggests such a decrease in correlation length with increasing plasma turbulence levels. The frequencies and wavenumbers they observe are considerably larger than in this experiment.

To check the effect of using differential probe measurements with the twin radial probes, the scaling factor in Eq. (IV-10) is plotted in Fig. IV.21. The common mode rejection r_{cm} of the circuit depends on the match of the probes, bias, cables, and terminators as well as the amplifier, and is expected to lie between the two extremes plotted. The value of r_{cm} is not important for the wavenumber range of the slow mode. Evidently, the fast mode has been suppressed by an amount not well determined, but probably greater than a factor of five.

Because of the spread in wavenumber over and above that attributable to the resolution of the measurement, we can infer from Fig. IV.21 that the use of the twin probes has biased the measurement in the wavenumber range of the slow mode in favor of larger wavenumbers. The amount of bias depends on the location of the peak and width of the actual spectral density vs. k. To evaluate this bias we need to estimate the actual width from the measured width. We can approximate the measured width by

$$\Delta k_m^2 = \Delta k_s^2 + \Delta k_I^2, \qquad \text{(IV-11)}$$

the expression valid for Gaussians, where Δk_m is the width measured, Δk_s^2 is the actual width, and Δk_I is the instrumental width due to the finite range of probe separation covered. Table IV-2 gives estimates of wavenumber spread and position of the maximum for the actual spectral

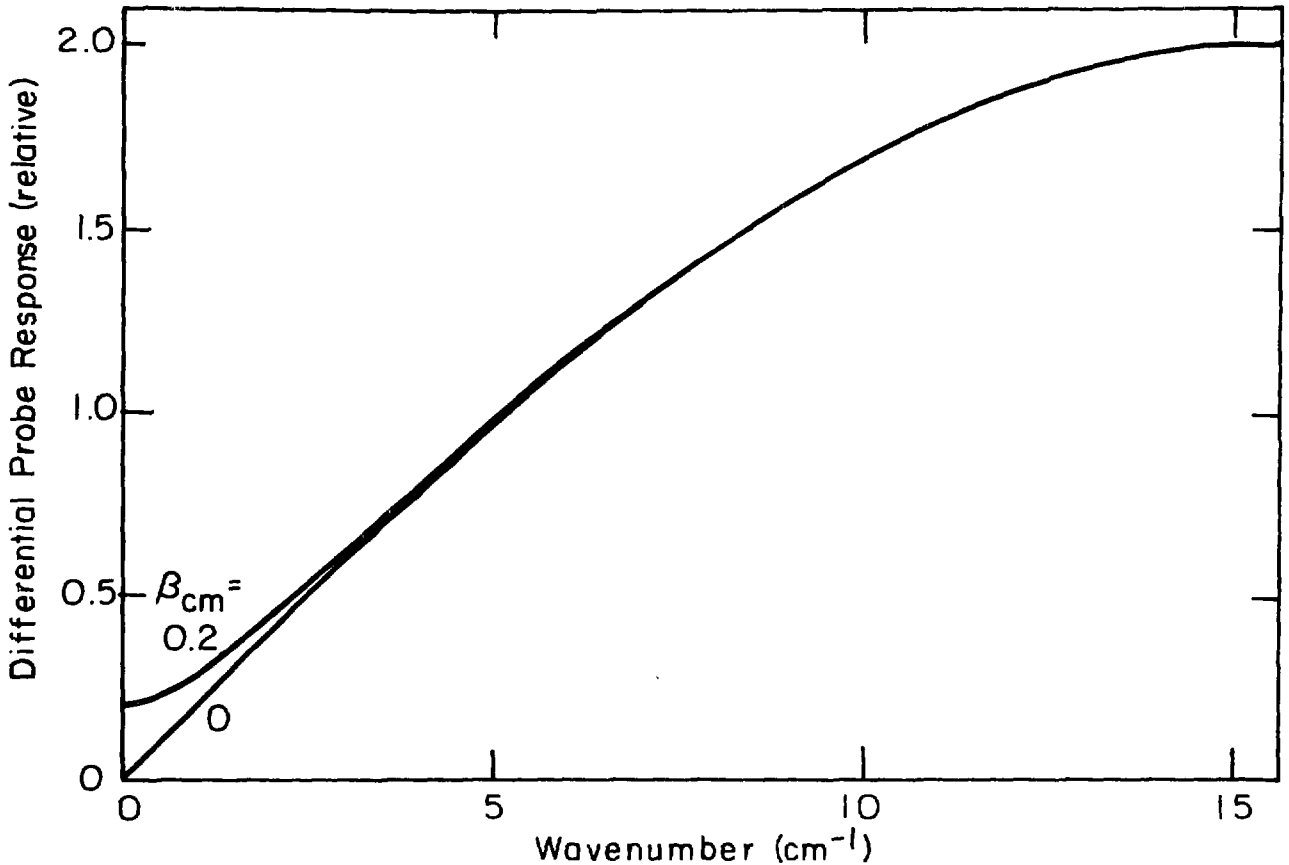

Figure IV.21 Response as a function of wavenumber for twin radial probes in differential mode. Differential response is shown relative to a single probe response for poor overall common mode rejection (β_{cm}=0.2) and for good rejection (β_{cm}=0). XBL802-4655

TABLE IV-2: Adjusted Characteristics of the Maximum in Spectral Density

Plot	Width(cm^{-1})			Adjusted Values	
	Δk_m	Δk_I	Δk_s (estimated)	wavenumber (cm^{-1})	spectral density(KHz^{-1})
IV-12	6.0	5.1	3.2	5.2	1.6×10^{-7}
IV-13	6.0	4.2	4.3	4.2	1.7×10^{-7}
IV-14	7.6	4.2	6.3	4.9	1.3×10^{-7}
IV-15	7.0	4.2	5.6	5.1	7.7×10^{-8}

density at the peak frequency.

From this probe data an estimate of the expected TBS signal may be obtained. This requires relating the normalized spectral density vs. wavenumber and frequency of the probe fluctuations to light intensity modulation and from there to response of the TBS system. The resulting estimate may then be compared with the noise level of the detector-amplifier to determine the signal to noise ratio achieved. The balance of this chapter is concerned with the signal to noise ratio estimate and the assumptions underlying it.

Since the interferometer is adjusted to a wavelength of 1 cm, we must obtain the spectral density for a wavenumber of 6.3 cm^{-1} from the probe data. This spectral density should then be rescaled by the ratio of the wavenumber resolution of the TBS system to that of the probe measurement:

$$S_{TBS}(\omega) \approx \frac{\Delta k_m}{\Delta k_s} \frac{\Delta k_{I,TBS}}{\Delta k_I} S_{probe}(6.3 \ \ cm^{-1}, \omega). \qquad \text{(IV-12)}$$

Equation (IV-12) also includes a correction factor for the increase in wavenumber spread of the measured spectral density compared to the estimated spread, assuming this latter is small compared to the resolution of the TBS system. Figure IV.22 shows the resulting estimated spectral density for the probe data of Fig. IV.12, where the frequency and wavenumber dependence near the peak spectral density has been approximated by a quadratic form, and a linear relation has been used for $k(\omega)$. Because of the spread in $k(\omega)$, most of the response of the spectrometer is to frequencies near the peak of the plasma fluctuation spectrum, although the wavelength match occurs near 1100 KHz. Also, the peak spectral density is reduced because the correlation length of the fluctuations is smaller than the length of plasma sampled

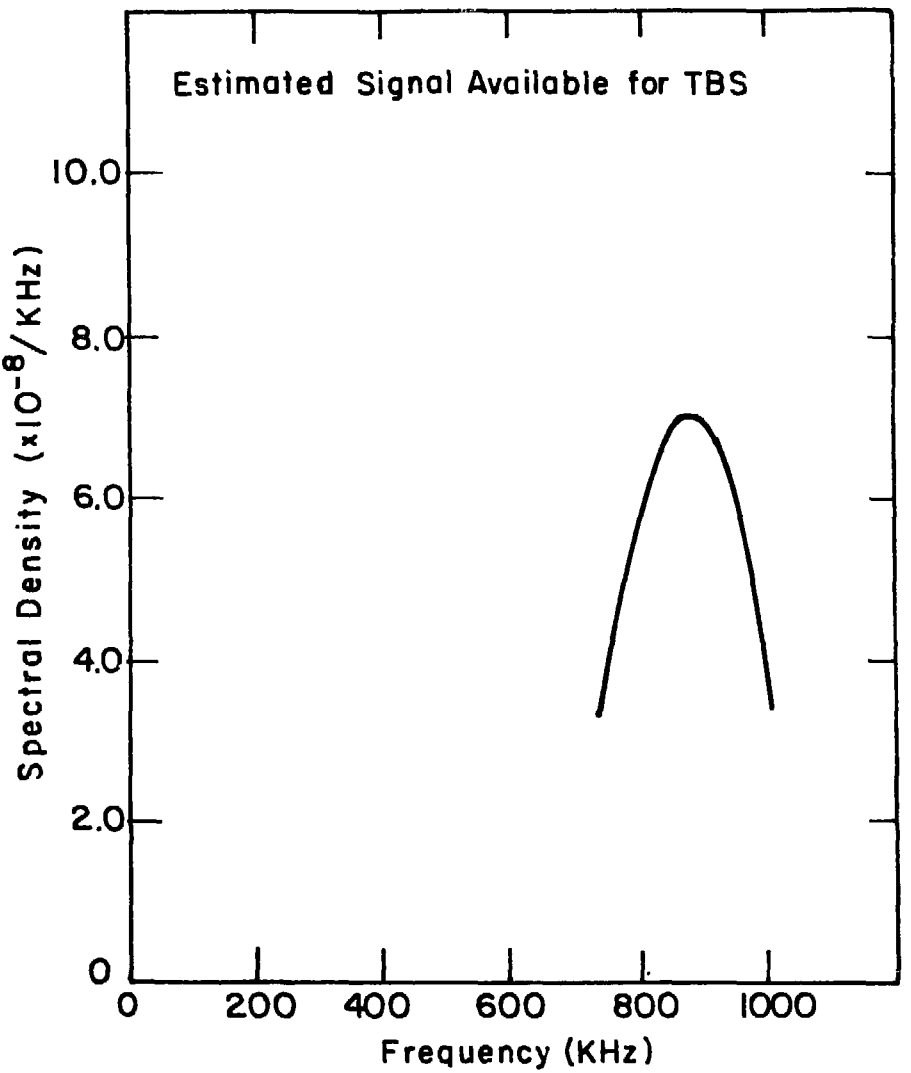

XBL 802-4662

Figure IV.22 Estimated signal available for TBS. This estimate is computed in units of probe cross power spectral density from the probe data plotted in Fig. IV.12.

by the two-beam spectrometer.

Use of the spectral density estimate in Fig. IV.22 also depends on the assumptions that the normalized probe current fluctuations are a measure of the normalized density fluctuations, and that these are a measure of the normalized light intensity fluctuations. Doucet et al.[19] make the former assumption for measurements of ion-acoustic wave density perturbation with probes biased just above the space potential, while Fenneman[1] does not attempt to measure $\delta n/n_o$, and his experimental relative response vs. probe bias, or "dynamic probe characteristic" shows a marked sensitivity to bias, which indicates the assumption can be valid only for a limited range of bias. In the present experiment, the combination of the two assumptions was crudely verified in the preliminary investigation of the fluctuations with probes and the simple light detector. The probe bias used is close to that used by Doucet et al. The actual estimate of TBS signal must be regarded as somewhat tentative.

NOISE The response of the TBS to the wave simulated by the chopper provides a good calibration of the response to relative light intensity fluctuations. The chopper simulates a plasma with one-half the actual light intensity and 100% ($\Delta I/I_o = 1$) peak modulation amplitude. Thus the peak-to-peak amplitude of the response to the chopper is equivalent to the peak amplitude response for an actual wave in the plasma having $\Delta I/I_o = 1$. To normalize the estimated spectral density in terms of the TBS system response then requires a factor of one-half (for the mean square) the peak-to-peak amplitude response to the chopper. This experimental factor then includes losses due to inefficiencies in the system. Since the simulated frequency is small compared with the

bandwidth of the detector-amplifier system, the estimate obtained is valid for the input signal level, when the chopper response is expressed in terms of input current, or for output levels, if the output chopper response is used and the frequency response of the detector-amplifier system taken into account.

In section IV.B.1 an expression was derived for the equivalent input noise for a simplified version of the amplifier-diode system assuming an ideal operational amplifier. A more complete analysis appears in Appendix D, but the expression derived [Eq. (IV-4)] has the proper form. It contains a frequency independent term due to thermal noise in the feedback network and shot noise of the photodiode current, and a term proportional to frequency squared due mainly to thermal noise in the photodiode and amplifier voltage noise.

At the output the noise will, of course, reflect the response of the amplifier-diode system. Figure IV.23 shows the measured output noise spectra (obtained by spectrum averaging Nicolet recordings using a 5 MHz sample rate) for the detector-amplifier system without plasma light, and for the amplifier with 10K resistors substituted for the photodiodes. The latter spectrum may be used to calibrate the frequency response of the amplifier. For comparison, the noise due to the feedback network is calculated (Appendix D) to be 2×10^{-8} V^2/KHz at low frequencies, and that due to the 10K resistors, 1.38×10^{-6} V^2/KHz. The factor of two discrepancy arises because the spectral density calculated is one-half the spectral density for positive frequencies derived in the Johnson noise formula. (The spectral density is an even function which includes negative frequencies. It is used consistently for the probe and spectrometer measurements, so

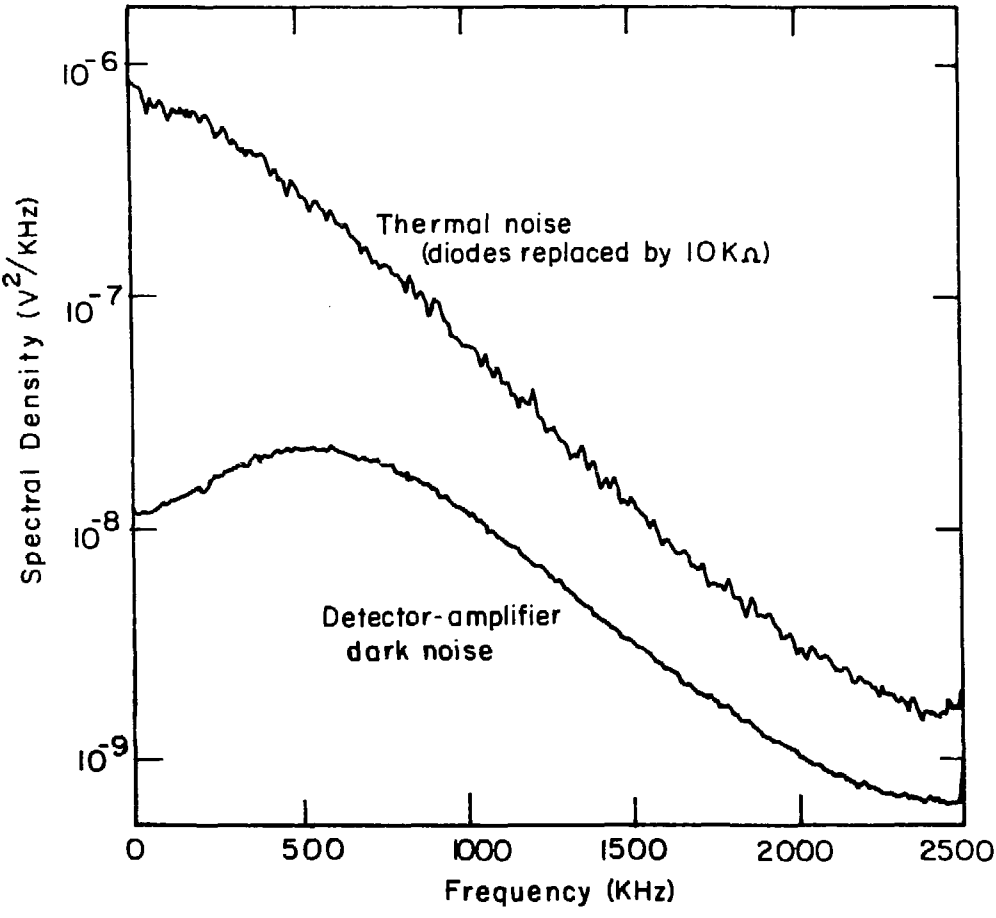

XBL 802-4652

Figure IV.23 Detector-Amplifier output noise spectral density. For comparison, thermal noise produced by 10 KΩ resistors in place of the photodiodes is also shown.

that no conflict arises in comparisons between the two.)

Figure IV.24 is an equivalent input noise spectrum (dark noise), derived from least squares fits to the data of Fig. IV.23. When the signal spectral density estimate of Fig. IV.22 is scaled as described above, the predicted peak spectral density for comparison with the equivalent noise is 1.1×10^{-24} A^2/KHz. Estimates of the diode thermal noise, based upon 1 KΩ series resistance and 10 pf junction capacitance, indicate the amplifier input voltage noise is the more important component in the noise which increases with the square of frequency. The estimated shot noise spectral density, to be added to the dark noise spectral density, is 7×10^{-24} A^2/KHz.

As explained in the last chapter, the signal-to-noise ratio is not determined by the noise spectrum above, but from the uncertainty in the signal plus noise spectrum obtained from a given set of data. The experimental spectrum of the TBS response is the average of M power spectra obtained from digitized recordings. Since the spectral density is predominantly noise power spectral density, an ensemble of such spectrum averaging experiments should yield a distribution of spectra approaching (for large M) a normal distribution with a standard deviation for each frequency point reduced to $M^{-\frac{1}{2}}$ times the standard deviation for the spectral density from a single recording or:

$$\sigma_M(\omega) = \frac{1}{M^{\frac{1}{2}}} \langle S(\omega) \rangle_{M \text{ sets}}. \qquad \text{(IV-13)}$$

In the example under consideration, M = 90 so that

$$\sigma_{90}(f) = 6.2 \times 10^{-25} \, A^2/KHz \left[2.2 + \left(\frac{f}{184 \text{ KHz}}\right)^2\right]. \qquad \text{(IV-14)}$$

This is used to normalize the estimated signal, and the result is plotted in Fig. IV.25. The total signal, then, is an average of about

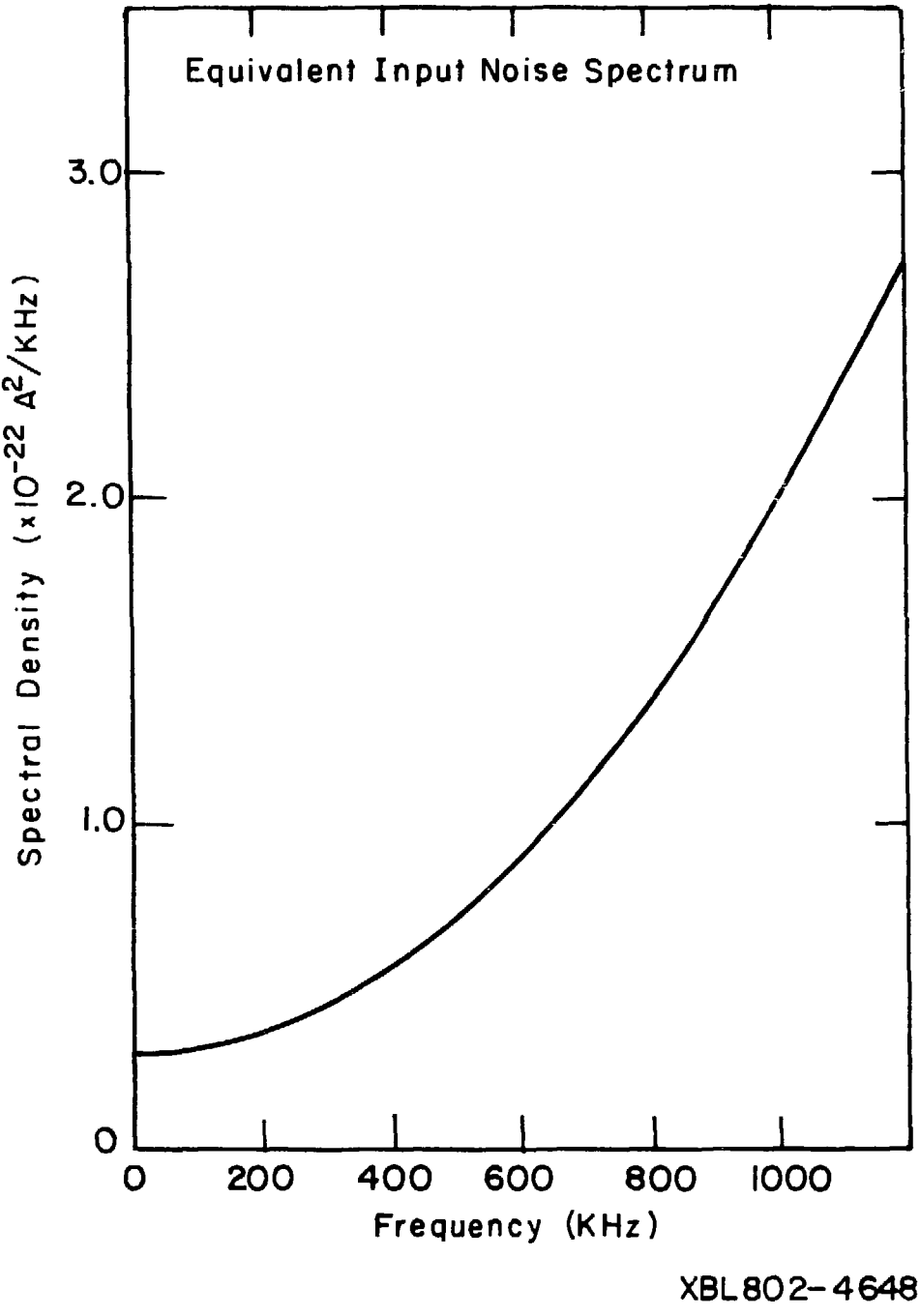

Figure IV.24 Equivalent input noise spectral density for the detector-amplifier.

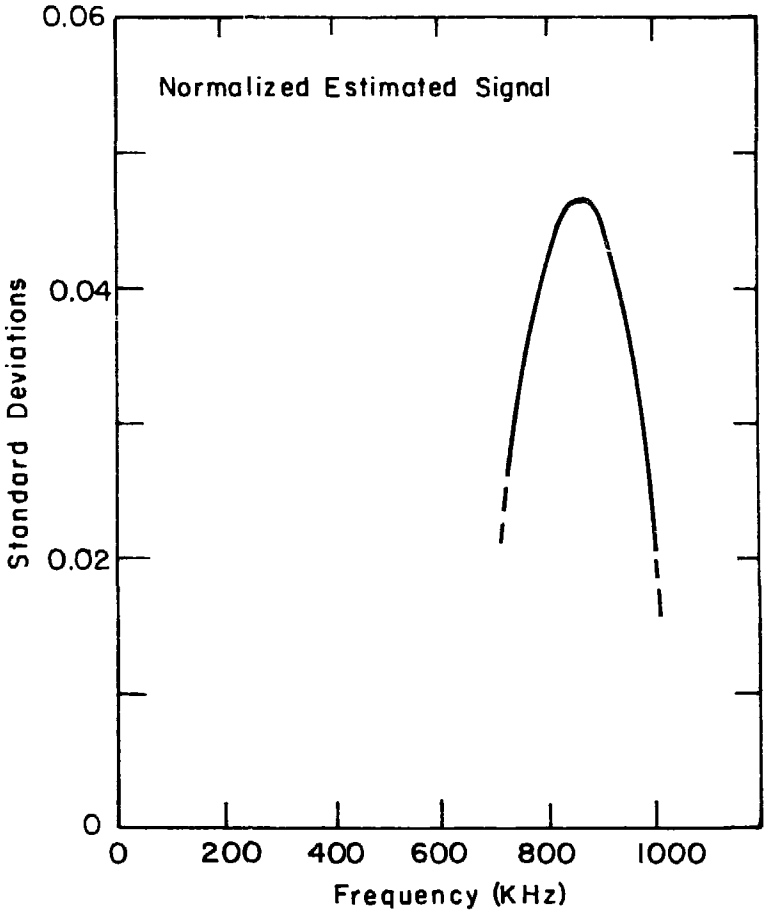

Figure IV.25 Estimated signal available for TBS normalized by uncertainty in the noise spectral density. This figure gives the ratio of the expected signal spectral density to the standard deviation in the average noise spectral density obtained from 90 spectra for each independent frequency measurement. (The finite recording time T for each spectrum limits the frequency resolution, meaning frequencies within a range T^{-1} are not independent.)

4.6×10^{-2} standard deviations over a frequency range of about 250 KHz. There are 250T (T is the length of each recording in milliseconds) independent frequencies in this range for which the signal plus noise power spectral density is determined. Therefore the total signal power is about 4.6×10^{-2} $(250T)^{\frac{1}{2}}$ standard deviations above the total noise power in the same frequency range. In this example, the result is 0.66 standard deviations for T = 0.8192 milliseconds. The next slower sampling rate (2 MHz) can provide recordings of 2.048 milliseconds, but the Nyquist frequency is then one MHz, and aliasing of the noise from the 1 to 1.25 MHz range becomes a problem. In this particular case, the 2 MHz sampling rate was tried, yielding little improvement in signal-to-noise ratio.

The conclusion is that the prototype system does not provide an adequate signal-to-noise ratio for an observation of this wave. Even if the above result were more favorable, the small size of the signal spectral density in relation to the noise spectral density (of order 0.5%) indicates that systematic changes could cause problems, and it would be desirable to obtain reference probe and noise spectra as near simultaneously as possible. Presently, it is not practical to intersperse the various measurements, and consequently changes (such as temperature drifts of order 2°C) can easily affect the noise spectrum by an amount comparable to the estimated signal. The only hope is that the frequency dependence of such effects can be distinguished from that of the estimated signal, and the accuracy of this estimate is adequate for the purpose.

REFERENCES

1. D.B. Fenneman, Ph.D. Thesis, University of Illinois at Urbana-Champaign (1972, unpublished).

2. A.W. Trivelpiece and R.W. Gould, J. Appl. Phys. 30, 1784 (1959).

3. R.N. Franklin, Plasma Phenomena in Gas Discharges (Clarendon Press, Oxford, 1976), pp. 117-119.

4. R.L. Stenzel, A.Y. Wong, and H.C. Kim, Phys. Rev. Lett. 32, 654 (1974).

5. Y. Hatta and N. Sato, in Proc. of the 5th Internat. Conf. on Ionization of Phenomena in Gases, Munich, Germany, 1961, ed. H. Maeckner (North-Holland, Amsterdam, 1962), p. 478.

6. N. Sato, A. Sasaki, K. Aoki, and Y. Hatta, Phys. Rev. Lett. 19, 1174 (1967).

7. P.D. Goldan and W.M. Leavens, Phys. Fluids 13, 433 (1970).

8. T. Chen and L. Schott, Phys. Fluids 20, 844 (1977).

9. R.W. Gould, Phys. Rev. A136, 991 (1964).

10. M. Widner, I. Alexeff, W.D. Jones, and D.E. Baldwin, Phys. Fluids 13, 2532 (1970).

11. J.L. Hirshfield, J.H. Jacob, and D.E. Baldwin, Phys. Fluids 14, 615 (1971).

12. K. Estabrook and I. Alexeff, Phys. Fluids 15, 2026 (1972).

13. D.B. Ilić, J. Appl. Phys. 44, 3993 (1973).

14. K.F. Schoenberg, private communication.

15. K.F. Schoenberg, Ph.D. Thesis, University of California, Berkeley (1979, unpublished). pp. 55-64.

16. C.J. Weinstein, IEEE Trans on Audio & Electroacoustics AU-17, 153 (1969).

17. R.S. Scorer, Clouds of the World (David & Charles, Newton Abbot Devon, 1972), pp. 170-171.

18. D.B. Ilić, K.J. Harker, and F.W. Crawford, Phys. Lett. 54A, 265 (1975).

19. H. Doucet, I. Alexeff, and W.D. Jones, Phys. Fluids 11, 2451 (1968).

CHAPTER V: CONCLUSIONS

The results to date have failed to show detection of a wave in a plasma by TBS. However, the results are encouraging because they are sufficiently explained by the wide bandwidth and low level of the plasma fluctuation, and time and equipment limitations preventing improvement of the prototype system. The experience gained, in particular with the response of the system to the chopper-simulated wave and from the probe data and measurement using the crude light detector (benefiting from approximately forty times the light gathering capacity of the TBS system), indicate that the measurement could, in principle, be made, and that it may be representative of possible practical applications for TBS. This chapter presents what has been learned from the prototype system and conclusions that can be drawn concerning applications. The first section outlines suggestions for improvement and the second applications and limitations.

A. Suggestions for Improvement

This section will consider improvements in the same order the TBS system was described in the previous chapter, that is starting with the interferometer and optics and ending with data acquisition and analysis. Not all changes can be made without affecting other parts of the system however, so the discussion will include interrelated parts when necessary.

1. Optical System. The interferometer sets the basic limitations on light acceptance (aperture and field) of the TBS system. The stability and ease of adjustment of the interferometer also affect the performance and flexibility of the system. The current two-degreee

($-2° \leq \theta \leq 2°$) field of view along the discharge axis (and the 1.2° thus subtended by the radius of the tube) with aperture of 1 cm (circular) could be improved by making the mounting more compact. This would require moving the compensating wedge to a position between the mirrors or possibly replacing the beamsplitter with a more accurate one to avoid the need for a wedge. The limit on the field would be improved as the optical path length within the interferometer is reduced until the limit for the performance of the polarizing beamsplitter is reached. Beyond that limit the aperture could be increased to take advantage of any further path reduction. The aperture could be further increased by using a larger beamsplitter. Here the limit will probably be set by the input focusing system, which will require smaller focal ratios and may introduce excessive aberrations. An oblong aperture could be used to take advantage of the smaller field of view perpendicular to the discharge axis.

Improvement on the current individual mounting system is suggested by the way the interferometer is analyzed in Appendix C. The mirrors should be mounted as one unit with a permanent adjustment of the angle between them compatible with the beamsplitter. After that, the only adjustment required should be the relative position and orientation of the axis of rotation they define and the plane of the beamsplitting surface. Ideally, the relative position adjustment along the direction normal to the beamsplitting surface will not disturb the other adjustments. It is used to vary the fringe spacing, and a calibrated fine adjustment is preferable.

In the remainder of the optical system, light efficiency can be improved somewhat by reducing the number of surfaces which reflect or

scatter some of the light passing through. This can be accomplished mainly by making changes that allow elimination of some of the lenses. In the input focusing system a single lens (given an adequate selection of focal lengths) will suffice if the polarizer used can be placed just in front of the interferometer (requiring an aperture larger than that of the interferometer beamsplitter), or can be used in divergent light (between the plasma and the lens). A possible polarizer[1] consists of a coating which could be placed on the lens, combining a pair of surfaces into one with a smaller reflection coefficient. In the output system presently in use are two coated lenses, an analyzing beamsplitter with uncoated surfaces, and the uncoated photodiode windows. Eliminating a lens would require changes in the analyzer and detector. For instance, the analyzer could be placed at the interferometer exit requiring that it have a larger aperture than the interferometer beamsplitter. If the analyzer were placed after the output lens (in converging light), the lens focal length would have to be large enough to satisfy the angular acceptance limits of the analyzer, which would also require a bigger detector area.

These changes in the input and output systems would amount to only a 5 - 8% increase in efficiency per pair of surfaces eliminated or coated. By far the greatest improvement possible is in the interferometer. If the field of view can be increased to 3.5° with satisfactory performance, making the interferometer more compact would increase the light gathering capacity by as much as five times. Rostler[2] has suggested modifying the interferometer to take advantage of the maximum light acceptance of the beamsplitter (eleven times that of the prototype interferometer). One possibility is to incorporate a

telescope within the interferometer to relay the light, thus forming an image of the entrance aperture coincident with the exit aperture. Since the two beams traverse the telescope in opposite directions, symmetry of the telescope would be very important. The power of the telescope must be unity to within a severe limit. The telescope introduces an angle between two image wavefronts $\Delta\theta$, where

$$\Delta\theta = (P - 1/P)\theta. \qquad (V\text{-}1)$$

In this equation, P is the power of the telescope (and 1/P the power of the telescope when reversed), and θ is the angle between the direction of the incident wavefront and the axis of the system. If $\Delta\theta$ is too large, the phase difference between the two image wavefronts will vary by more than a fraction of a wavelength across the aperture, and the interference effect will be reduced.

One final area for improvement of the optical system is in the methods of ruling out spurious response to overall light intensity fluctuations (any fluctuations of a wavelength long compared to the dimensions of the region of the discharge observed). Rostler[3] suggests each of the two beams be balanced using adjustments in the relative sensitivity of the two detectors and in the orientation of the analyzing beamsplitter for the two degrees of freedom needed. The prototype detector-amplifier system did not allow the accomplishment of the first adjustment electronically (some improvements in the detector-amplifier to be discussed below would eliminate this problem), but presumably some kind of adjustable light attenuator could be used in front of a detector. The main difficulty found was an additional imbalance source in the number of fringes visible to each detector. If the length of plasma observed is not an integral number of wavelengths (fringes), one of the detectors will see more of the plasma

than the other. An adjustable field stop is needed to correct this source of imbalance in the response to the total light.

Some sort of total light chopper, preferably like a shutter that could be moved in the way of the light from a direction perpendicular to the wave propagation, would be helpful in balancing the system. I found that difficulties with the photodiode mounts finally made a good balance unattainable when the smaller area SGD 100A photodiodes were substituted for the original diodes, resulting in a little of the light missing the active area of the diodes.

2. Detector-Amplifier. As discussed in the last chapter, the largest contribution to the noise problem proved to be amplifier input voltage noise and the thermal noise of the photodiode series resistance. These two sources produce the noise component which increases with frequency in accordance with the decreasing reactance of the photodiode junction capacitance and other capacitive loading of the input terminals. The photodiode noise is the smaller portion, of order one-fifth the total, based on an estimated 10 pf junction capacitance and 1 KΩ resistance. The main possibilities for noise reduction are cooling the amplifier and diodes or finding a suitable substitute diode with a lower product of junction capacitance and time constant ($R_s C_j^2$). Such a substitute will probably have a smaller active area and require a lens to concentrate the light. The capacitive loading can be minimized by using the shortest possible lead length between the amplifier and the photodiodes.

If the improvements suggested for the optical system provide a large increase in light collection, the picture starts to change around for this experiment. The shot noise of the photoconduction current begins to dominate for higher and higher frequency range,

and improvements in the detector-amplifier system become less important. Nonetheless, they should be considered for possible extension of the technique to higher frequencies or less luminous plasmas.

Photomultiplier tubes should also be considered as a detector-amplifier combination. The main difficulty confronted in this experiment is the poor quantum efficiency for the infrared light. As shown in Chapter III, the shot noise aspect of the signal-to-noise problem is made worse by a low quantum efficiency, in this case negating improvements in other aspects. There would be less sacrifice if the 5875 Å light could be used (necessitating a new beamsplitter), and the advantage over silicon detectors would be especially important for extension to higher frequencies.

Aside from the effects of quantum efficiency, the main source of noise is the statistical fluctuation in the number of secondary electrons per photoelectron, essentially determined by the number of secondaries generated at the first dynode. Dark current has negligible effect for the light levels in this experiment. The gain fluctuations cause a noise increase proportional to the shot noise.[4] When a high gain gallium arsenide-phosphide dynode is used for the first stage, the gain fluctuations are minimized, and the increase in noise over shot noise is not very large. At the photomultiplier output, the signal level will be sufficiently high that additional noise contribution from any buffer amplifiers needed can be made negligibly small.

3. Data Acquisition and Analysis. The essence of a TBS measurement is the observation of correlations in the light collected by the optical system. To this end (as has been indicated generally

in Chapter III and again more specifically for this experiment in Chapter IV), data analysis involves recognizing the fluctuations in the output due to the light intensity fluctuations of interest, as opposed to those random fluctuations due to noise. The data acquisition and analysis system accomplishes this goal by revealing spectral characteristics of the signal fluctuation distinguishable from the more slowly varying noise fluctuation spectrum or by measuring the noise spectrum separately and subtracting it from the signal plus noise spectrum obtained in the experiment. Equivalently, the data acquisition and analysis reveals, in the time correlation function of the output, signal features having a longer correlation time than that of the noise fluctuations. In principle, the technique used in this experiment is an ideal way to do so, as the data recordings contain both the signal and noise characteristics, meaning that all the spectral features were obtained simultaneously. (By contrast, an analog spectrum analyzer obtains a spectrum a little at a time, by sweeping through the frequency range at a rate slow enough to obtain the frequency resolution desired.) This section explains the practical limitations encountered with the data acquisition and analysis setup used, and the room for improvement remaining.

The data acquisition and analysis in this experiment is limited mainly by the time required for transmission of the data recorded from the Nicolet digital oscilloscope to the ModComp Systems computer. As far as the computer is concerned, only about two milliseconds of the time history of the TBS output can be "acquired" in about ten seconds. An analog spectrum analyzer could obtain (in somewhat less time) a spectrum equivalent to the spectrum obtainable from the two

millisecond time history, although the analog spectrum analysis would still be subject to the handicap that the spectrum may be affected by drifts in conditions over the longer time period required to complete the spectrum. The data transmission rate problem is a result of the indirect data link between the building containing the experiment and that housing the computer. With provision for a direct data link, the time is reduced from 11.4 seconds to 150 milliseconds. A direct link could be installed between the buildings, probably requiring some simple repeating stations to restore the attenuated signals.

Even better results could be achieved with a commercially available real-time signal averaging device. For example, an available correlation and probability analyzer is capable of obtaining the correlation function of a signal for 400 values of time delay spaced as little as 0.2 microseconds apart. The real-time capability means that the device performs this data acquisition and analysis of the signal during the period the record is obtained. This is equivalent to speeding up the present system so that no gaps occur between recordings, and the spectrum averaging calculations are completed as soon as the last recording is made. What now requires over seventeen minutes plus analysis time could be done in less than 100 milliseconds.

Real-time data acquisition is important where long averaging times are needed to improve the signal-to-noise ratio. Real-time data analysis would be helpful where adjustments may have to be made based on the results obtained. This experiment could be improved if results of the probe measurements were available quickly enough to permit optimization of the conditions producing the wave. A separate

channel to provide simultaneous probe and TBS data acquisition would also help to insure that the probe data represent the conditions present for the TBS measurement. Presently the long data acquisition time and the time required to change from TBS to probe connections allows about twenty to thirty minutes for conditions to drift between measurements.

Faster data acquisition would also improve possibilities for using reference signal measurements to aid in the analysis. There are several possibilities for turning the signal on and off so that it could be obtained by subtracting noise measurements from noise plus signal measurements. Means could be provided to temporarily block the plasma light to the two detectors and substitute two reference light sources of constant intensity equal to the average plasma intensity. If the two detector signals are amplified separately, they could be acquired separately and analyzed to compare both sum and difference fluctuation levels. The input polarizer can be rotated to eliminate the interference by extinguishing either the transmitted or reflected polarization component in the interferometer. If the system is properly balanced, this should eliminate the signal without changing the light received by the two detectors. The signal may also change in a recognizable fashion when the wavenumber magnitude setting or the propagation direction selected by the TBS system is changed.

Faster data acquisition is important when using a comparison tehcnique because of the degradation in signal-to-noise ratio pointed out in the last chapter in addition to the need for minimizing drift. Since the signal must be obtained from the difference of two nearly

equal measured quantities, twice as much data will be required for each measurement to obtain the same standard deviation calculated for the single measurement, for a total of four times the data acquisition time.

B. Estimates of Limitations for Possible Applications

In conclusion, the attempt to detect the wave in the positive column using TBS was apparently unsuccessful because of signal-to-noise limitations of the prototype system. The purpose of this section is to summarize the limitations and possible improvements in terms useful for considering the suitability of TBS for possible future applications. Estimates for this experiment will be considered first, followed by ways of evaluating other applications.

The most significant improvements outlined above would come from increasing the light acceptance of the interferometer, optimizing the detector-amplifier combination, and improving the data acquisition for increased signal averaging. Without using a larger beamsplitter, the first two could combine to produce more than a factor of thirty signal-to-noise enhancement. Shot noise then would become a major constituent, and this estimate assumes greater care in filtering out unused plasma light wavelengths. Use of a larger beamsplitter for additional light collection then could increase the signal-to-noise by about the amount of the light increase, i.e., the amount of the signal-to-shot noise improvement.

I suspect the other improvement, increased data acquisition efficiency, would be applied mainly to reducing the time for a measurement to make possible inclusion of reference data as suggested above and to improve the comparison with the probe data. The total time recorded

for a measurement would remain on the order 1/10 sec, but the actual time required would be reduced to as little as that or at least to the time required to run the axial probe through the range of positions required. Of course, many measurements could then be made and compared in the time it now takes for one, so signal-to-noise ratio improvement by data averaging is still available. What is suggested here is really a matter of judgment of what should be considered a single measurement. The argument in favor of the smaller groupings of data is that they provide separate comparisons between probe and TBS data with the possibility of altering the plasma conditions or the TBS wavenumber selection and observing the effects.

Combined, the improvements suggested in the first part of this chapter offer a reduction of the threshold for detection of the wave to the order of 1/100 the current estimate of the level of the signal in the light due to the wave. The measurement time required for this sensitivity would be reduced substantially, allowing another order of ten increase in sensitivity through additional averaging. The current estimate of the wave is a normalized mean density perturbation $\langle \delta n^2 \rangle^{\frac{1}{2}}/n_o$ of about 1%, spread over a frequency range of 300 KHz. The fluctuation available in the light for the TBS system is slightly smaller, because the wavelength chosen is shorter than that corresponding to the peak frequency, and the wavenumber resolution is smaller than the wavenumber spread of the plasma fluctuation. New equipment and rebuilding of the TBS system are required to realize these gains.

The signal level provided by the plasma fluctuation proved rather small for an initial test of TBS. That fact is encouraging for the generalization of what has been learned to evaluate other applications.

The fluctuation available is representative of a wider range of fluctuations that one might wish to measure than a narrow bandwidth externally driven mode would have been.

Figures V.1 and V.2 are maps of fluctuation intensity and bandwidth showing similarity curves for various values of the light emission rate per unit volume of the plasma. These curves are drawn for comparison with the conditions of this experiment, for which the estimated parameters of the wave for the TBS wavelength and resolution are indicated by the cross (+). Waves falling on the curve corresponding to the emission rate-time product for a given experiment will have a comparable relation of signal to dark noise (noise, such as thermal noise, in the detector-amplifier system that is not dependent on the photoconduction current) in the case of Fig. V.1, or signal to shot noise in the case of Fig. V.2. A comparable signal-to-noise relation (including dark noise and shot noise) would mean that in the same averaging time T the same overall signal-to-noise figure would be obtained. The comparison should take into account any improvements in efficiency incorporated as suggested above, and the frequency dependence of the dark noise if solid state photodiodes are to be used.

Accounted for in the efficiency of the TBS system should be the light acceptance of the optical system and effects of excess noise of the detector-amplifier system including that due to overall quantum efficiency less than unity. In addition, differences between the normalized density perturbation and the normalized light intensity fluctuation may arise for several reasons. The light may also depend on fluctuating electron temperature or ion density in the wave. As was the case in this experiment, the wavenumber spread of $k(\omega)$ can exceed

Figure V.1 Similarity curves of light emission rate vs. fluctuation intensity and bandwidth for comparison with the experimental signal to dark noise relationship. An experiment (using the same TBS apparatus), for which the point representing the fluctuation level observable and bandwidth to be detected falls on (or above) the line corresponding to the volume emission rate of the plasma light, would achieve the same (or better) signal to dark noise relation in the same total averaging time as was achieved in this experiment. In addition, if the improvements suggested in the text are incorporated in the apparatus, the estimate of potential signal to noise improvement in this chapter would apply. The total signal to noise relation of an experiment would also depend on the signal to shot noise relation, for which similarity curves are shown in Fig. V.2.

Figure V.2 Similarity curves of light emission rate vs. fluctuation intensity and bandwidth for comparison with the experimental signal to shot noise relationship. This figure is useful in comparing signal available to noise associated with the light (shot noise of the photoelectron current, and pulse gain fluctuations in the case of photomultipliers) for a contemplated experiment with what was obtained in this experiment (or what is estimated assuming needed improvements are made). The comparison should be made in the same manner and in conjunction with the signal to dark noise comparison explained in Fig. V.1.

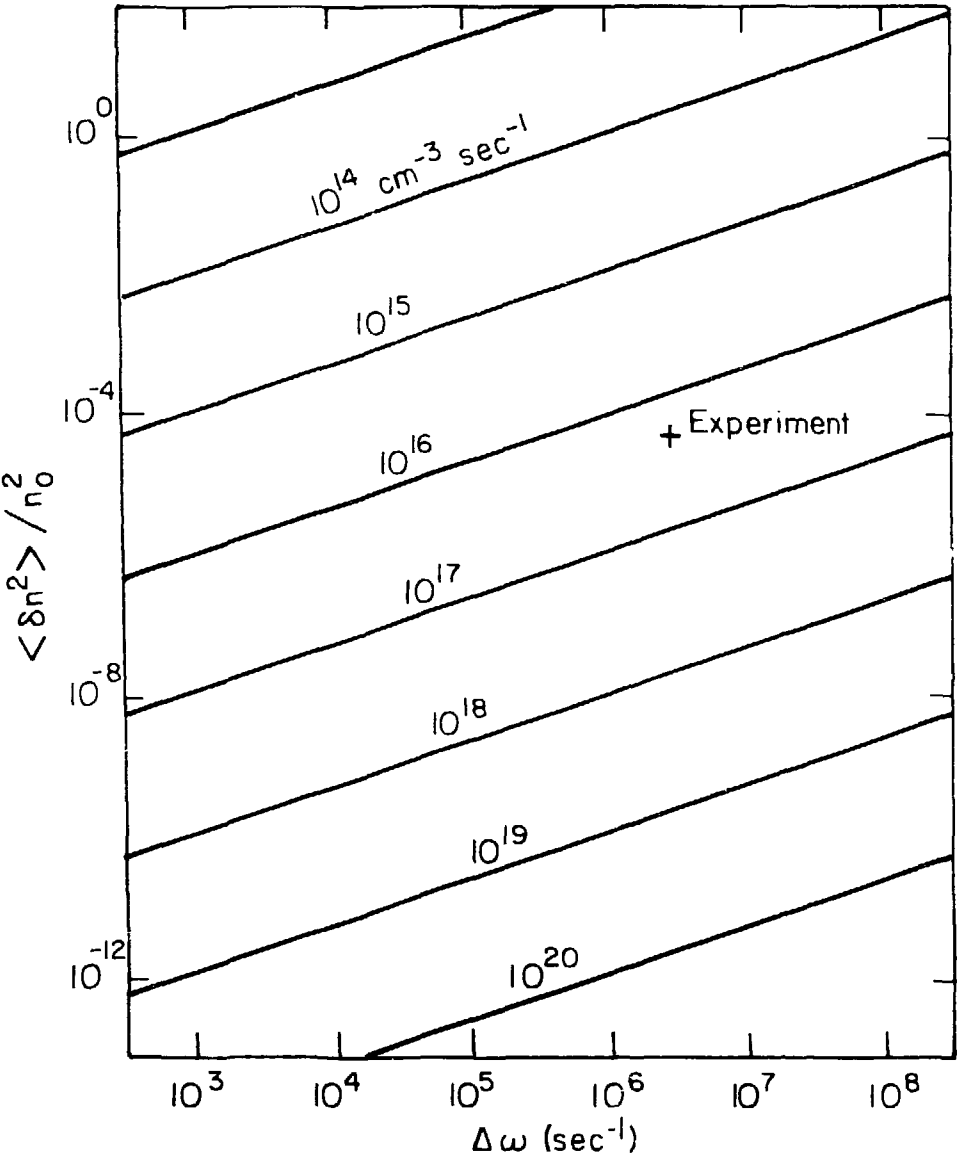

XBL802-4654

Figure V.1

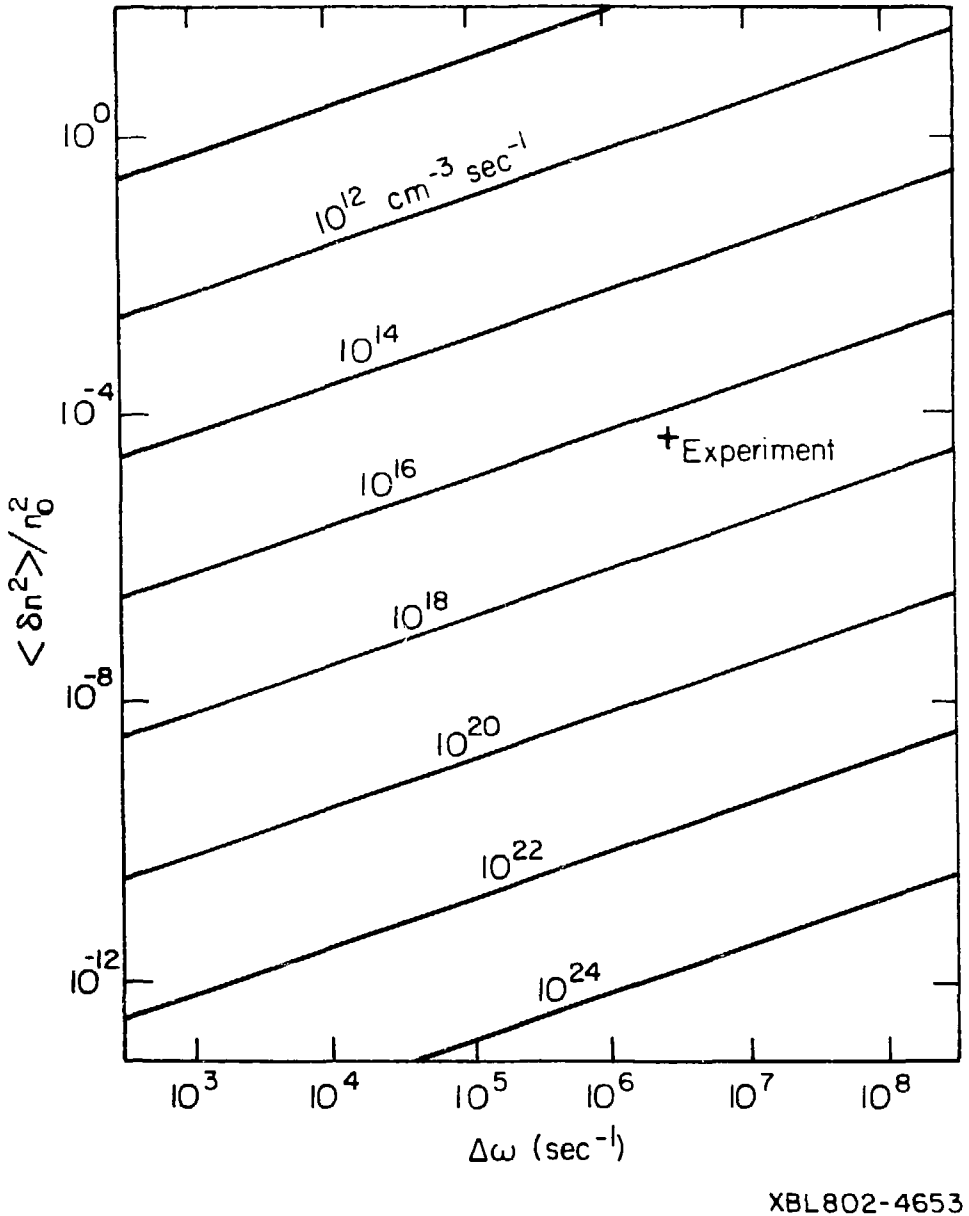
10^{0}
10^{-4}
10^{-8}
10^{-12}
10^{12} cm^{-3} sec^{-1}
10^{14}
10^{16}
10^{18}
10^{20}
10^{22}
10^{24}
+Experiment
$\langle \delta n^2 \rangle / n_o^2$
10^{3}
10^{4}
10^{5}
10^{6}
10^{7}
10^{8}
$\Delta\omega$ (sec^{-1})
XBL802-4653

Figure V.2

the wavenumber resolution of the TBS system. If spatial resolution along the line of sight limits the volume of the plasma in which the wave is observed, the light fluctuations will be a smaller portion of the total light collected. One effect limiting light collection in the experiment which was not discussed earlier but which can be important for comparing measurements of other waves is that the plasma did not fill the entire volume from which light could have been collected, due to the large wavelength of the fluctuation. This situation represents a borderline case of the appropriateness of TBS, and most applications would thus offer greater light collection efficiency than estimated for this experiment.

In summary it is difficult to make general statements about the applicability of TBS in other experimental situations. Specific conditions can be compared with those of this experiment using Figs. V.1 and V.2. Assuming the recommended improvements in the TBS system are incorported, comparable conditions would indicate a very favorable signal-to-noise relation, or the possibility of reducing the averaging time (in proportion to the square of the acceptable signal-to-noise reduction) for a faster response in the measurement.

C. Summary

Briefly, the following important theoretical and experimental findings are presented in this thesis. A new and simpler TBS system design can replace the multiple-beam system proposed by Rostler. Theoretical calculations presented confirm the new system offers greater light collection efficiency without sacrificing the possibility of spatial resolution.

In addition a mechanism of wavelength compensation is now provided for use with broadband light sources. The comparison of TBS with stellar interferometry made in the introduction suggests one possible application outside plasma diagnostics for which this advantage should be considered. Light available is one problem in the application of the stellar interferometry technique, and it is exacerbated by the necessity of selecting a narrow wavelength range of the light.

Experimental results show the basic optical performance of the prototype system, and the existence of a spontaneous wave in the positive column suitable for study by TBS, if not quite adequate for demonstration of the prototype optical system. This system can be substantially improved in ways suggested earlier in this chapter. Given the time and equipment needed, the improvements possible should allow measurement of the wave, based on the signal-to-noise estimate obtained.

Since the wave used is a spontaneous fluctuation and not a coherent mode as would have been preferable for the test of the prototype TBS system, The measurement ultimately attempted in this experiment is more closely comparable to possible applications of TBS. Thus the conditions encountered are presented in a manner suitable for evaluating other diagnostic applications.

REFERENCES

1. R. Hagstrom, Phys. Rev. Lett. 35, 1677 (1975).
2. P.S. Rostler, private communication.
3. P.S. Rostler, Ph.D. Thesis, University of California, Berkeley (1974, unpublished). pp. 92-93.
4. F. Robben, Appl. Opt. 10, 776 (1971).

APPENDIX A: ANALYSIS OF THE INTERFEROMETER USING ROTATIONS AND REFLECTIONS

In idealized form, the interferometer constructed for this experiment makes use of combinations of reflections for the alternative paths of the two interfering beams. A formalism used in group theory[1] in which rotations are represented as combinations of reflections or mirrorings is helpful in analyzing the performance of the interferometer, and the notation and properties needed for this purpose are explained below. First, a brief description of the propagation of wavefronts through the interferometer is presented to indicate the assumptions made in using the mathematical model.

In Fig. A.1, wavefronts are followed through the interferometer for incidence parallel to the axis and incidence at 3.5° to the axis. Figure A.1 (a) shows the path of beam A, which has π polarization, while Fig. A.1 (b) shows beam B, the σ polarization component of the light. The extent of the wavefronts has been limited (as shown by the cross sections depicted) by an aperture placed in the preceeding optical system.

An image of this aperture is positioned at the midpoint of the optical path within the interferometer. In the part of the system illustrated, the effect of the real aperture can be found from the aperture image, according to a well-known result of geometric optics.[2] As shown, the system is adjusted to suit the interferometer if the beamsplitter has a useful aperture of 80% of its width and can be used for angles of incidence up to 3.5°.

Figure A.1 Schematic of basic interferometer, showing paths of light for beams A and B in (a) and (b) respectively. The aperture image (3) shows that the wavefronts and paths have been arranged by the preceding optical system to pass the interferometer without vignetting the wavefronts by the edges of the mirrors (2) or the beamsplitter (1). The path shown entering at an angle to the axis of the interferometer represents the maximum angle of acceptance allowed by the input system consistent with this requirement.

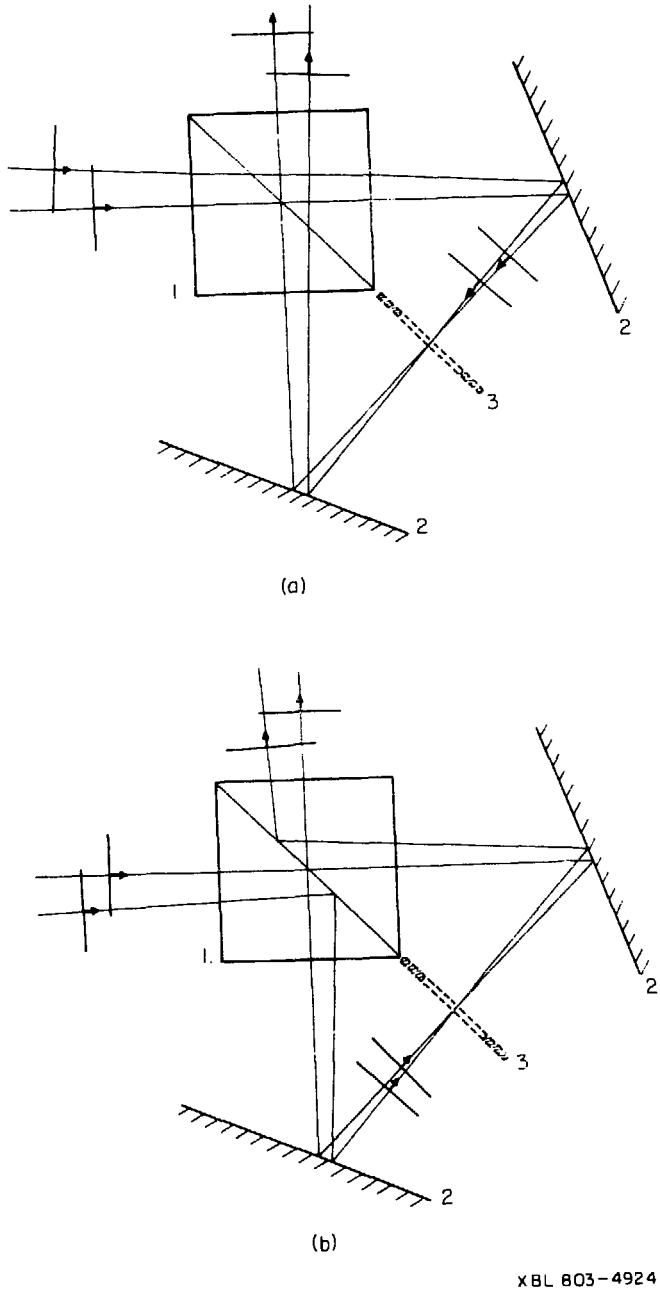

Figure A.1

If diffraction effects are small, we may assume the positions of the edges of the mirrors and beamsplitter are not important as long as they are outside of the beams. Since these conditions are well-satisfied for the interferometer shown, the mirrors and beamsplitter may be represented by simple planes of reflection, and the propagation of wavefronts may be determined from the propagation of the image wavefronts resulting from the appropriate sets of reflections. Figure A.2 illustrates the interferometer models for beams A and B, indicating the order in which the reflections are to be applied.

To obtain the image wavefront resulting from a set of reflections according to this model, the set of points on the surface of the wavefront is transformed mathematically according to the reflections involved. The transformed points then make up the image wavefront. Figure A.3 shows how a reflection may be represented. The plane of reflection M is specified by the direction of the unit normal vector $\hat{e}$ and by a point $\underline{x}$ contained in the plane. The transformation of the point $\underline{P}$ by the reflection M is then represented by

$$\underline{P}' = M\underline{P} \equiv M_{\underline{x}}(\hat{e})\underline{P}. \qquad \text{(A-1)}$$

When $\underline{P}$ is seen after two reflections (first M_1, then M_2), the image of $\underline{P}$ is written

$$\underline{P}'' = M_2\underline{P}' = M_2M_1\underline{P}$$

$$= M_{\underline{x}_2}(\hat{e}_2)M_{\underline{x}_1}(\hat{e}_1)P. \qquad \text{(A-2)}$$

Any representation of a reflection which defines the same plane of reflection is equivalent, that is

$$M_{\underline{x}}(\hat{e}) = M_{\underline{x}'}(\hat{e}'), \qquad \text{(A-3)}$$

if

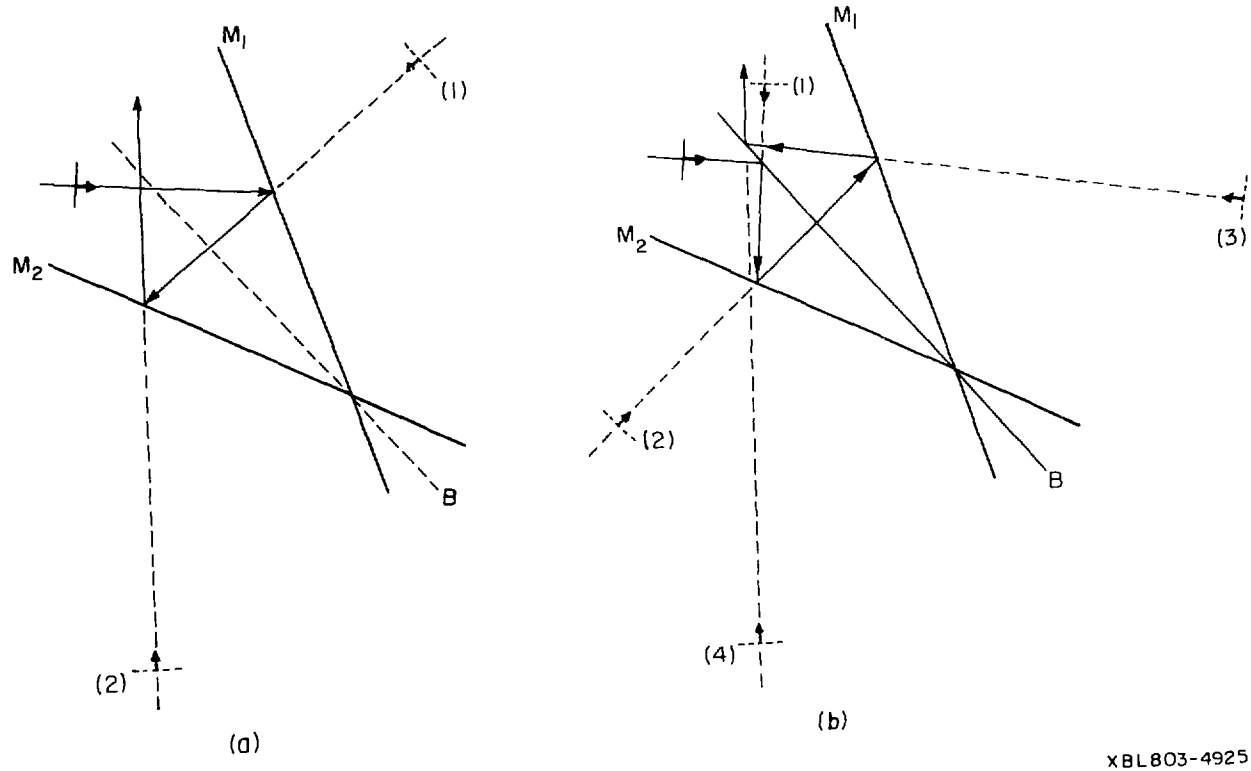

Figure A.2 Model for the interferometer illustrated in Fig. A.1 indicating the planes of reflection of the mirrors M_1 and M_2 and the beamsplitter B. Light paths for beams A and B showing the order of the reflections are shown separately in (a) and (b) respectively. An incoming wavefront is also shown, along with the successive images for beams A and B.

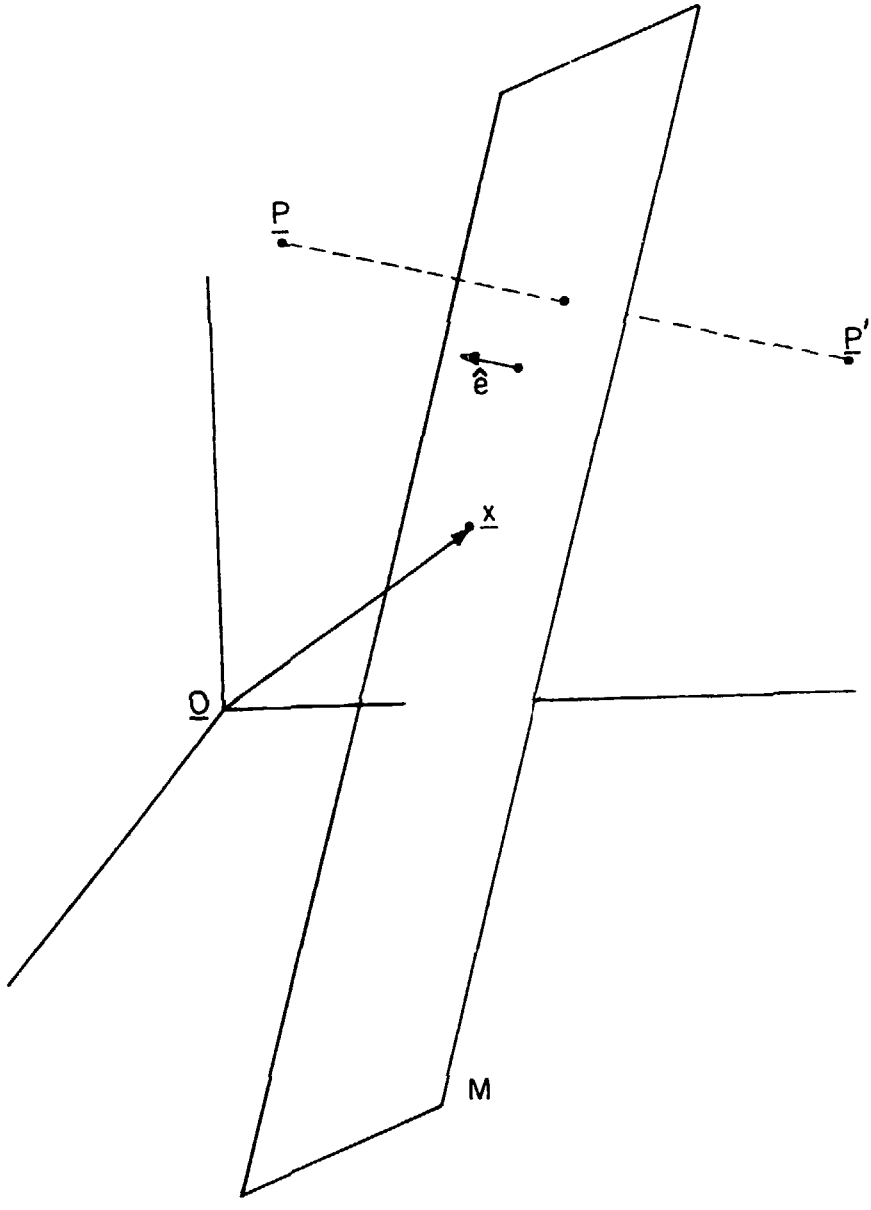

XBL803-4923

Figure A.3 A plane of reflection M showing a point $\underline{x}$ in the plane and a unit normal $\hat{e}$ used in the representation of $M_{\underline{x}}(\hat{e})$.

$$|\hat{e} \cdot \hat{e}'| = 1 \tag{A-4}$$

and

$$(\underline{x} - \underline{x}') \cdot \hat{e} = 0 \tag{A-5}$$

The analysis of the interferometer model then requires determination of the transformations corresponding to combinations or products of reflections. These reflections, and therefore their products, are distance-preserving transformations. When all possible combinations are considered, they make up the group of all distance-preserving transformations, which is the direct product of the group of inversions and the Euclidean group. (The Euclidean group consists of rotations and translations. As shown below, rotations about any axis can be expressed as a product of two reflections, and parallel rotations by equal angles are related by translations.) Clearly a reflection is its own inverse:

$$M_{\underline{x}}(\hat{e})M_{\underline{x}}(\hat{e}) = I. \tag{A-6}$$

Another important property is associativity--for example,

$$M_{\underline{x}_2}(\hat{e}_2)M_{\underline{x}_1}(\hat{e}_1)\underline{P} = [M_{\underline{x}_2}(\hat{e}_2)M_{\underline{x}_1}(\hat{e}_1)]\underline{P}. \tag{A-7}$$

As illustrated by the two-dimensional sketch in Fig. A.4, we note that these transformations are not in general commutative:

$$M_{\underline{x}_2}(\hat{e}_2)M_{\underline{x}_1}(\hat{e}_1) \neq M_{\underline{x}_1}(\hat{e}_1)M_{\underline{x}_2}(\hat{e}_2).$$

Another useful property indicated in Fig. A.5 is that a pair of reflections combines to form a rotation. Two planes of reflection intersecting at an angle θ produce a rotation about the line of intersection by an angle 2θ, in the same sense as that of the first plane being rotated into the second:

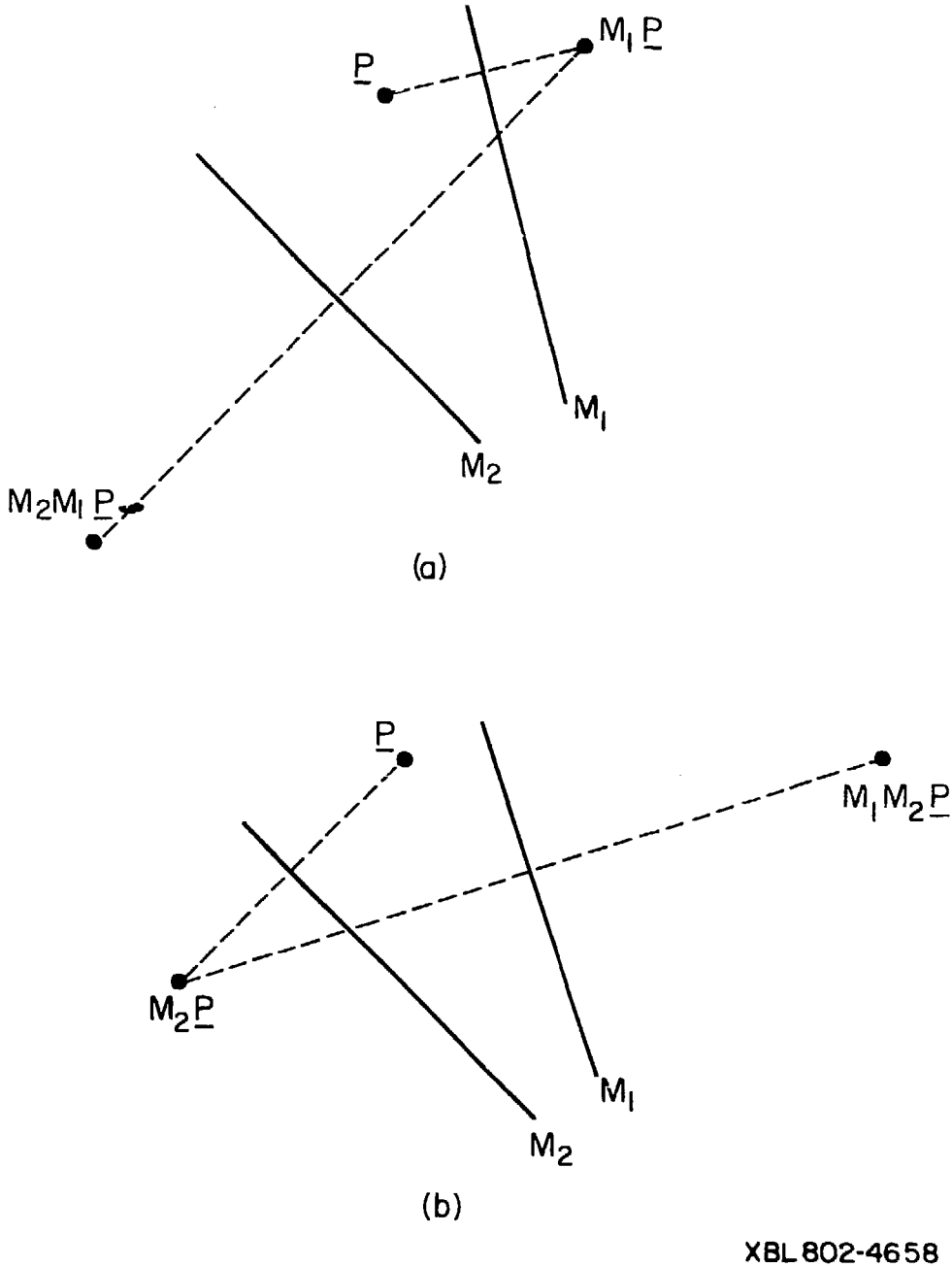

Figure A.4 An example showing that reflections are not generally commutative. In (a) the order of the reflections is first M_1 then M_2 while in (b) the order is reversed.

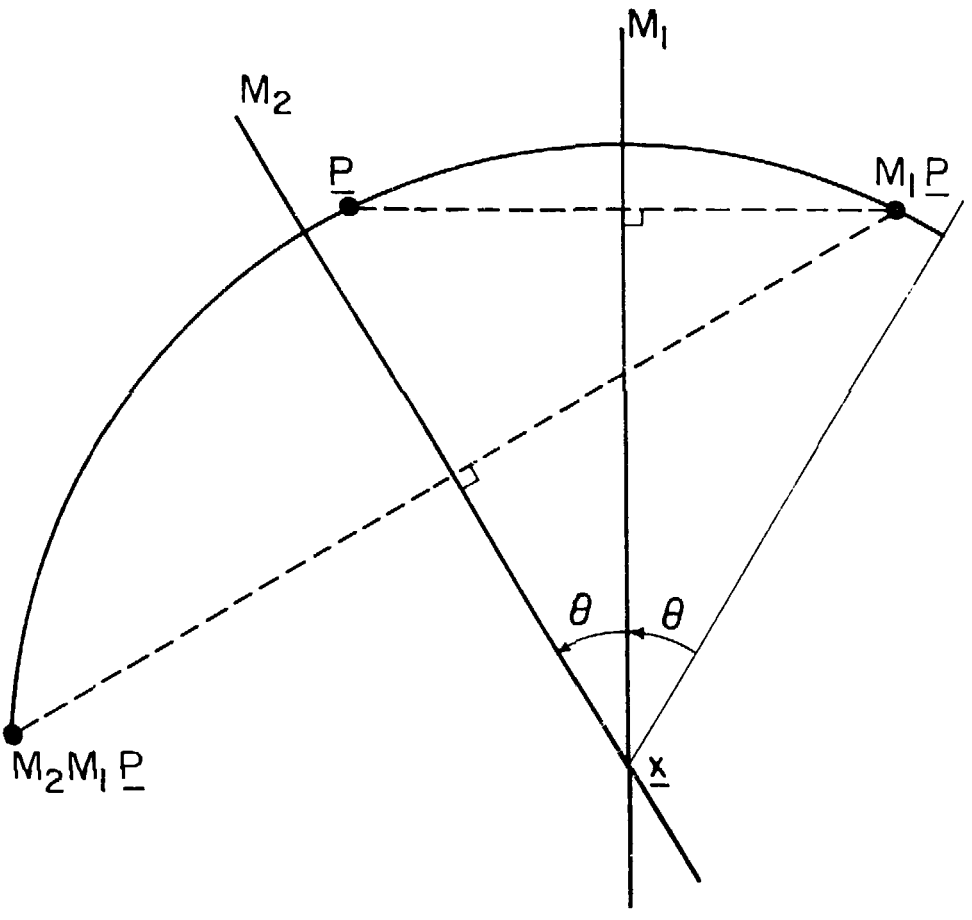

XBL802-4659

Figure A.5 A construction illustrating that two reflections form a rotation.

$$M_{\underline{x}_2}(\hat{e}_2)M_{\underline{x}_1}(\hat{e}_1) = M_{\underline{x}}(\hat{e}_2)M_{\underline{x}}(\hat{e}_1)$$

$$= R_{\underline{x}}(\hat{e}_1 \times \hat{e}_2, 2\theta), \qquad \text{(A-9)}$$

where

$$(\underline{x} - \underline{x}_1)\cdot \hat{e}_1 = (\underline{x} - \underline{x}_2)\cdot \hat{e}_2 = 0, \qquad \text{(A-10)}$$

and

$$\cos\theta = \hat{e}_1 \cdot \hat{e}_2. \qquad \text{(A-11)}$$

Thus $R_{\underline{x}}(\hat{e},\theta)$ represents a rotation about an axis parallel to $\hat{e}$ through $\underline{x}$ by an angle θ, seen as counterclockwise when $\hat{e}$ points at the viewer.

Figure A.6 illustrates the transformation of one reflection by another. This property can be expressed

$$M_2 M_{\underline{x}_1}(\hat{e}_1)M_2 = M_{M_2\underline{x}_1}(M_2\hat{e}_1) \qquad \text{(A-12)}$$

or

$$M_2 M_{\underline{x}_1}(\hat{e}_1) = M_{M_2\underline{x}_1}(M_2\hat{e}_1)M_2, \qquad \text{(A-13)}$$

where $M_{\underline{x}_2}(\hat{e}_2)$ has been shortened to M_2. If the order of two reflections is reversed, the one originally first must be replaced by its mirror image as formed by the other. Applying this result to a rotation yields

$$M_1 R_{\underline{x}}(\hat{e},\theta) = R_{M_1\underline{x}}(M_1\hat{e},-\theta)M_1; \qquad \text{(A-14)}$$

in words, a reflection transforms a rotation into its mirror image rotation.

From the above properties, the transformation for beam A is already solved. The image wavefront is obtained by applying the rotation defined by the reflections M_1 followed by M_2 shown in Fig. A.2 (a):

$$T_A = M_{\underline{x}_2}(\hat{e}_2)M_{\underline{x}_1}(\hat{e}_1). \qquad \text{(A-15)}$$

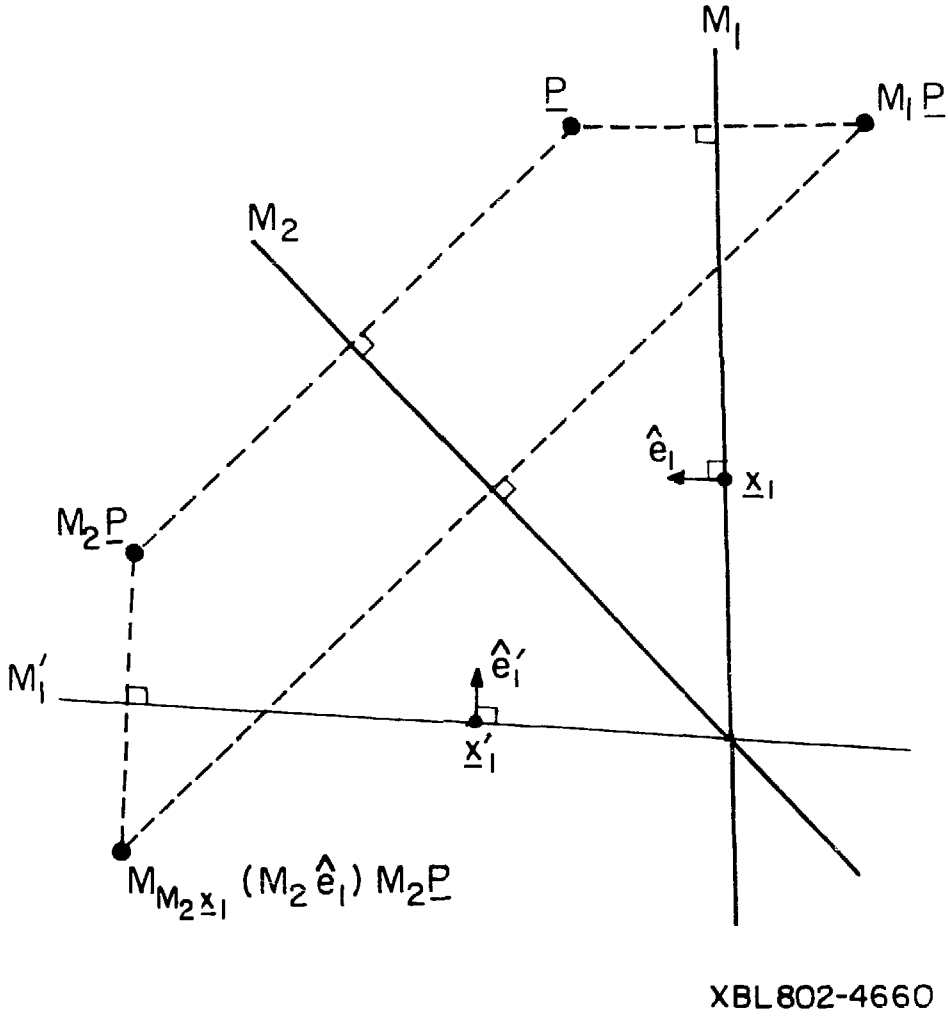

Figure A.6 Transformation of one reflection by another. The order of two reflections may be reversed if one plane is replaced by its mirror image as seen in the other.

For polarization B the transformation is more complicated, but it is expressible in a straightforward manner. We can choose an origin $\underline{0}$ in the plane of the beamsplitter and a point $\underline{x}$ in the line of intersection of two mirrors. Then the transformation to the image wavefront is

$$T_B = M_{\underline{0}}(\hat{e}_b)M_{\underline{x}}(\hat{e}_1)M_{\underline{x}}(\hat{e}_2)M_{\underline{0}}(\hat{e}_b) \tag{A-16}$$

where $\hat{e}_b$ is the normal vector for the beamsplitter, and $\hat{e}_1$ and $\hat{e}_2$ are the normal vectors for the mirrors M_1 and M_2. [The numbering of the mirrors agrees with that in Fig. A.2 (a).] In this notation the rotation for beam A is re-expressed as

$$T_A = M_{\underline{x}}(\hat{e}_2)M_{\underline{x}}(\hat{e}_1)$$
$$R_{\underline{x}}(\hat{e},2\theta). \tag{A-17}$$

In Eq. (A-16), the middle two reflections form the same rotation as for polarization A except in the opposite direction, making

$$T_B = M_{\underline{0}}(\hat{e}_b)R_{\underline{x}}(-\hat{e},2\theta)M_{\underline{0}}(\hat{e}_b)$$
$$= M_{\underline{0}}(\hat{e}_b)R_{\underline{x}}(\hat{e},-2\theta)M_{\underline{0}}(\hat{e}_b). \tag{A-18}$$

Using Eqs. (A-6) and (A-14), the result reduces to

$$T_B = R_{M_0(\hat{e}_b)\underline{x}}(M_{\underline{0}}(\hat{e}_b)\hat{e},2\theta). \tag{A-19}$$

When the axis of rotation defined by $\underline{x}$ and $\hat{e}$ is parallel to the plane of reflection of the beamsplitter, as it is intended to be in the interferometer, the relations

$$M_{\underline{0}}(\hat{e}_b)\hat{e} = \hat{e}, \tag{A-20}$$

and

$$T_B = R_{M_{\underline{0}}(\hat{e}_b)\underline{x}}(\hat{e},2\theta) \tag{A-21}$$

hold. In this case the two transformations are rotations of the

same angle about parallel axes separated by a distance $2\hat{e}_b \cdot \underline{x}$. The situation can then be represented two-dimensionally (Fig. A.7), showing how the image wavefronts are parallel and simply offset from each other by a fixed translation.

Equations (A-17) and (A-21) are of the form desired for a properly adjusted interferometer. When there are adjustment errors, the behavior is more complicated and requires the full three-dimensional analysis based on the formalism explained above. Appendix C contains a more general discussion, and requires one more set of relations for combining rotations.

The product of two rotations by the same angle in opposite directions about the same axis is clearly an identity transformation, so for every rotation there is an inverse rotation. A more general version of this can be deduced from Fig. A.7:

$$R_{\underline{x}_2}(\hat{e},-\theta)R_{\underline{x}_1}(\hat{e},\theta)\underline{P} = \underline{P} + R_{\underline{x}_2}(\hat{e},-\theta)\underline{x}_1 - \underline{x}_1, \qquad \text{(A-22)}$$

so

$$R_{\underline{x}_2}(\hat{e},\theta) = R_{\underline{x}_1}(\hat{e},\theta) + R_{\underline{x}_2}(\hat{e},-\theta)R_{\underline{x}_1}(\hat{e},\theta) \qquad \text{(A-23)}$$

is a relation that expresses a rotation about one axis as the sum of a rotation about a parallel axis and a translation.

Figure A.8 shows three planes which all intersect at the center $\underline{x}$ of a sphere, and which can represent three rotations with intersecting axes as follows:

$$\begin{aligned} R_{\underline{x}}(\hat{e}_1,2\theta_1) &= M_{\underline{x}}(\hat{e}_b)M_{\underline{x}}(\hat{e}_a), \\ R_{\underline{x}}(\hat{e}_2,2\theta_2) &= M_{\underline{x}}(\hat{e}_c)M_{\underline{x}}(\hat{e}_b), \\ R_{\underline{x}}(\hat{e}_3,2\theta_3) &= M_{\underline{x}}(\hat{e}_a)M_{\underline{x}}(\hat{e}_c). \end{aligned} \qquad \text{(A-24)}$$

Combining Eqs(B-24) yields an identity:

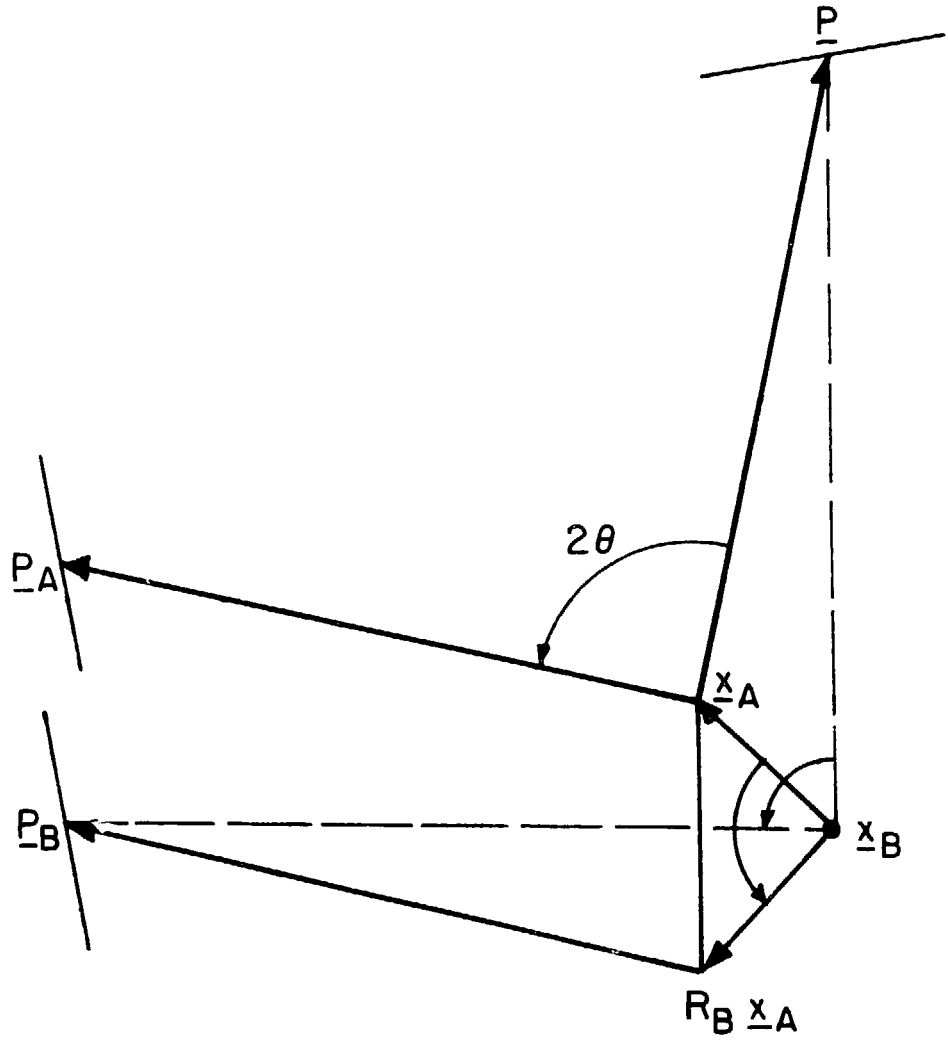

XBL802-4661

Figure A.7 Transformations of a wavefront at $\underline{P}$ to the points $\underline{P}_A$ and $\underline{P}_B$ for beams A and B respectively. This construction also illustrates the relation between two parallel rotations by the same angle 2θ.

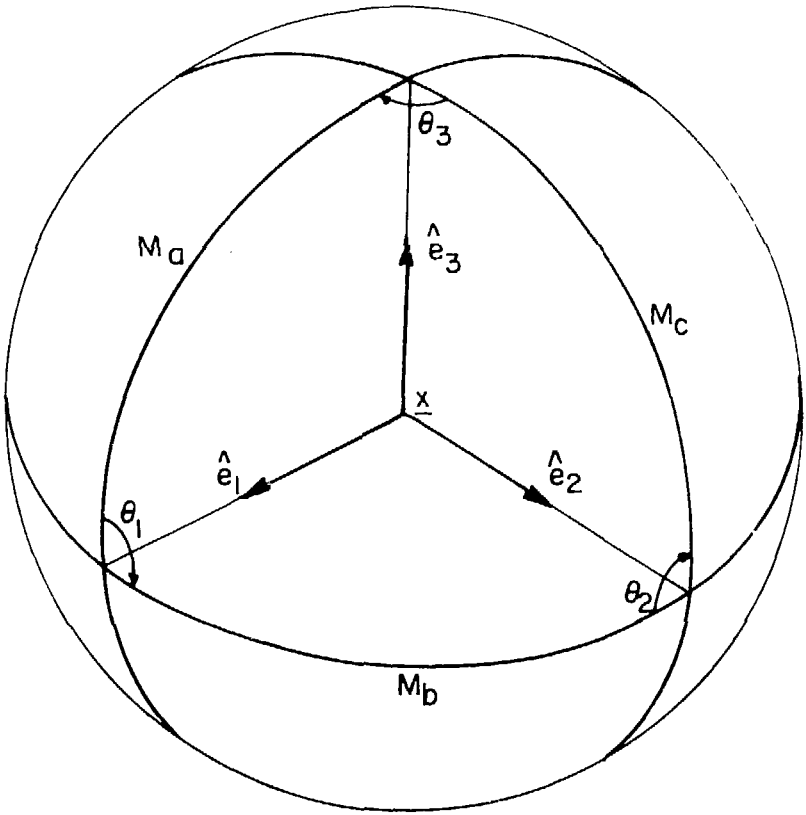

XBL803-4921

Figure A.8 Solution of a product of rotations by a spherical triangle. The planes M_a, M_b, and M_c are used in pairs to represent the three rotations by $2\theta_1$, $2\theta_2$, and $2\theta_3$ about $\hat{e}_1$, $\hat{e}_2$, and $\hat{e}_3$ respectively. The triangle is formed by the same three planes cutting the unit sphere centered at the common point of intersection $\underline{x}$.

$$R_3R_2R_1 = M_aM_cM_cM_bM_bM_a$$

$$= M_aIIM_a$$

$$= I, \qquad \text{(A-25)}$$

implying the product of R_1 and R_2 is the inverse of R_3. Thus the products of rotations are rotations that can be found by solving the spherical triangle formed as shown in Fig. A.8.

REFERENCES

1. M. Hammermesh, Group Theory and Its Application to Physical Problems (Addison-Wesley, Reading, MA, 1962), pp. 32-38.

2. K. Halbach, Am. J. Phys. 32, 90 (1964).

APPENDIX B: THE ACHROMATIC INTERFEROMETER

The advantage of the interferometer explained in Appendix A is that it can be made achromatic--wavelength independent. In Appendix A the performance of the interferometer is described in terms of a pair of rotations (for the two polarization components) separated by a displacement depending on the positions of the mirrors relative to the beamsplitter. The distance between the two rotation axes enters into Eq. (II-49) as a displacement by $2x_{AB}$, determining the fluctuation wavevector $\underline{k}_{\Delta}$ which the TBS system selects. Adding a dispersive component to the interferometer to vary this separation with wavelength in the proper manner can cancel the dependence of $\underline{k}_{\Delta}$ on the wavelength of the light and make the TBS system achromatic. This appendix explains how to achromatize the interferometer using a tilted glass window to add a wavelength-dependent displacement between the two beams.

Figure B.1 shows the interferometer with a glass window inserted. Also shown is the straightened-out line-of-sight or optical axis as seen at the output, with the two images of the window as seen via beams A and B. With the window tilted from normal to the optical axis as shown, the two beams will be shifted sideways in opposite directions by a small amount dependent on the wavelength for a dispersive medium like glass.

More to the point, the window introduces delays in the propagation of the two beams which vary with the angle of incidence and the wavelength. The delays can be analyzed as in Fig. B.2, showing the additional distance x the wavefront must travel because of the glass.

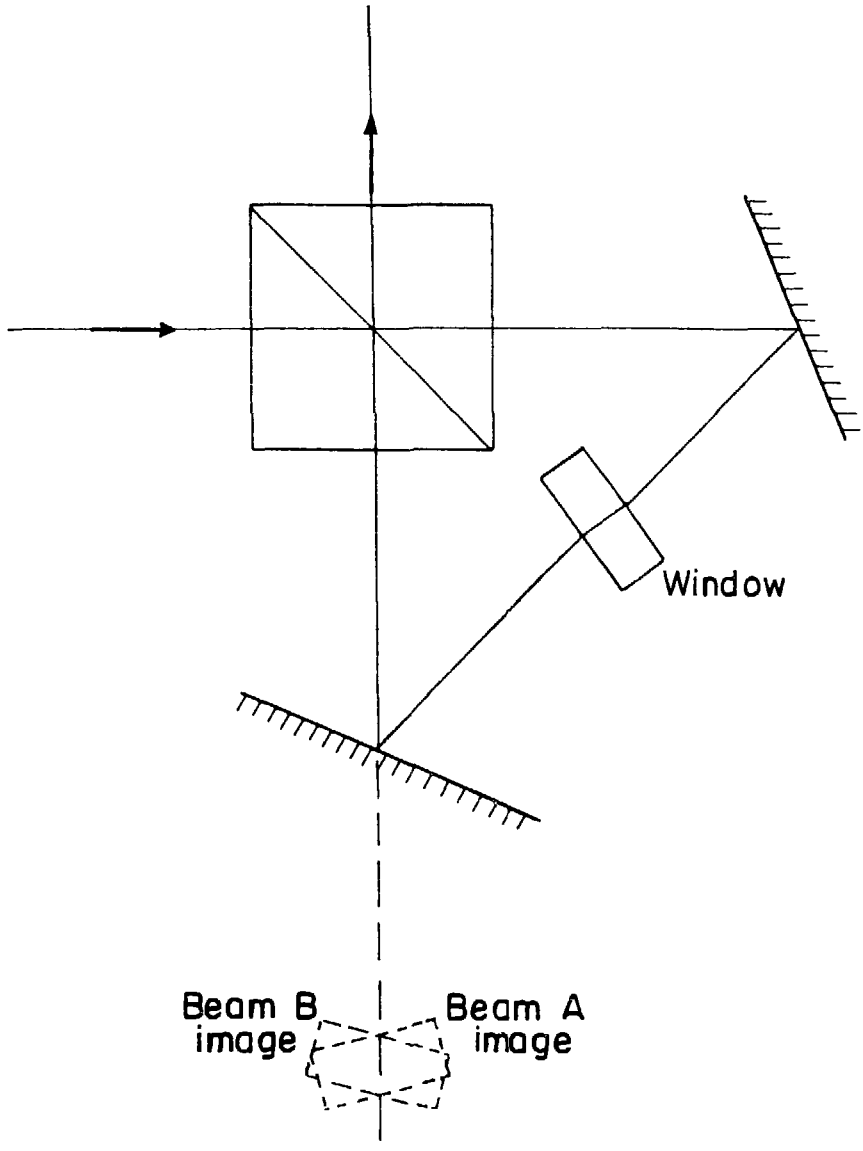

Figure B.1 Interferometer with window inserted to provide wavelength compensation. Images of the window as seen from the exit of the interferometer with each polarization component (beams A and B) are indicated by dashed lines.

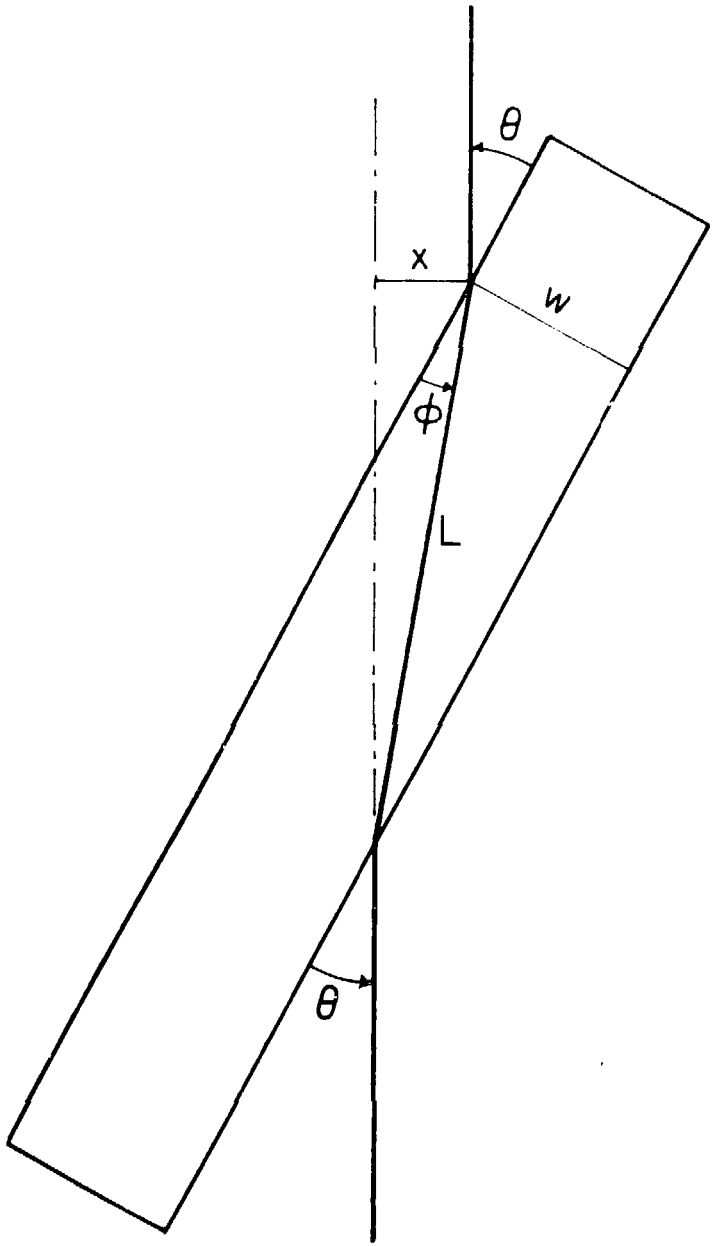

XBL 802-4668

Figure B.2 Delay of a wavefront incident on a window at an angle θ. The wavefront is delayed by the window of thickness W as if it had to propagate the extra distance X.

The equations needed to find x are Snell's law:

$$n(\lambda) \sin \phi = \sin \theta \qquad \text{(B-1)}$$

where θ and ϕ are the angles of incidence and refraction as shown, and $n(\lambda)$ is the index of refraction of the glass (as a function of wavelength λ) relative to air; and the relations for the two right triangles with the hypotenuse L:

$$W = L \sin \phi \qquad \text{(B-2)}$$

and

$$x = L \sin(\theta - \phi), \qquad \text{(B-3)}$$

where W is the thickness of the window. Combining these equations and solving for x yields

$$x = W[n(\lambda) \cos \phi - \cos \theta]. \qquad \text{(B-4)}$$

For a plane wave propagating parallel to the optical axis, the angle of incidence for beam B is the negative of that for beam A, and the net delay vanishes. The derivative of the extra path length with respect to the angle of incidence is given by

$$\frac{\partial x}{\partial \theta} = W\left[\sin \theta - n(\lambda) \sin \phi \frac{\partial \phi}{\partial \theta}\right]$$

$$= W(\sin \theta - \tan \phi \cos \theta). \qquad \text{(B-5)}$$

If the angle of incidence increases by a small angle $\delta\theta$ for beam A, it decreases by $\delta\theta$ for beam B. The difference in retardation (extra path length for beam A relative to beam B is then

$$x_{A-B} = 2W(\sin \theta - \tan \phi \cos \theta)\delta\theta. \qquad \text{(B-6)}$$

The relative retardation is also expressible as the result of a sideways separation of the A and B wavefronts (perpendicular to the optical axis) by an amount $2x_{AB}^{W}(\lambda)$, in analogy to the separation resulting from the displaced rotations used in Chapter II. The relative retardation is the component of the displacement perpendicular

to the wavefront, and is given for small angles by

$$x_{A-B} = 2x^{W}_{AB}(\lambda)\theta, \tag{B-7}$$

or

$$x^{W}_{AB}(\lambda) = \frac{\partial x}{\partial \theta}$$

$$= W\{\sin\theta - \frac{n(\lambda)\sin\theta\cos\theta}{[1 - n(\lambda)^2\sin^2\theta]^{\frac{1}{2}}}\}. \tag{B-8}$$

Expressed in this way, the action of the tilted window can be combined with that of the interferometer without the window by adding $x^{W}_{AB}(\lambda)$ to x_{AB}. Equation (II-49) in then modified to

$$k_{\Delta} = \frac{\omega_o}{c}\frac{2[x^{W}_{AB}(\lambda) + x_{AB}]}{f_1} \tag{B-9}$$

(where we are interested in the magnitude of k_{Δ} only). Since the wavelength of the light is inversely proportional to the frequency ω_o, the way to make the interferometer achromatic (k_{Δ} constant) is to arrange for the term in brackets to be proportional to wavelength. This is possible for at least some range of wavelengths because we can always expand $x^{W}_{AB}(\lambda)$ and arrange for x_{AB} to cancel the zero order term by adjusting the mirrors. For higher orders a combination of glasses could be used.

APPENDIX C: ANALYSIS OF ALIGNMENT ERRORS IN THE INTERFEROMETER

In Appendix A a properly adjusted interferometer was analyzed in terms of combinations of reflections that make up rotations. The two mirrors are supposed to be adjusted to form a rotation about an axis parallel to the plane of the beamsplitter so that the reversed rotation for polarization B is transformed to a parallel rotation when the effects of the two beamsplitter reflections are included. In this appendix we consider the case where the rotations are not parallel, and show the results can be used to explain the effects of inaccuracies in the angles between the beamsplitter surfaces.

If the rotation axis (the line of intersection of the planes of the two mirrors) is not parallel to the beamsplitter surface, then there is a point of intersection between the rotation axis and the plane of the beamsplitter surface. This point is a convenient choice of origin for the coordinate system. Let the x axis be normal to the beamsplitter plane, the y axis be the projection of the rotation axis in the plane, and the z axis be the other axis in the plane of the beamsplitter (see Fig. C.1).

The first step in analyzing this situation is to express the rotation due to the misaligned mirrors as the product of an aligned rotation and an error rotation [see Fig. C.2 (a)]. As explained in Appendix A, the relations between these rotations can be found by solving the spherical triangles formed by three reflection planes generating the rotations [see Fig. C.2 (b)]. It is convenient to let the common point of intersection of the rotations be at the origin and to restrict the choice of component rotations to an aligned

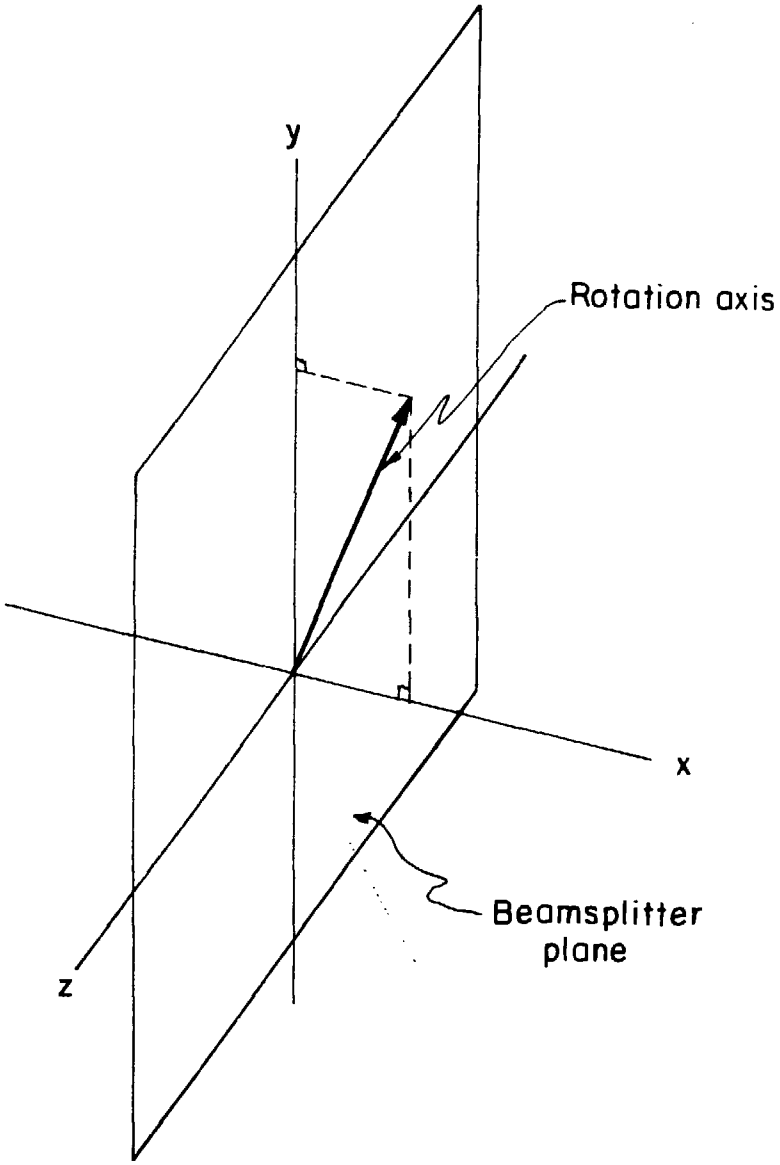

XBL 802-4667

Figure C.1 Choice of coordinate system for analyzing a misaligned rotation. The rotation axis shown is assumed to be misaligned out of the plane of the beamsplitter. The desired axis of rotation is chosen as the y-axis.

Figure C.2 Decomposition of the misaligned rotation into an aligned rotation and an error rotation. The relation between the misaligned rotation by $2\theta'$ about $\hat{e}'$ and the product of the error rotation by 2ϕ about $\hat{e}''$ followed by the aligned rotation by 2θ about $\hat{e}$ is constructed as in (a) and determined by solving the spherical triangle formed as indicated in (b). The technique is explained in Appendix A.

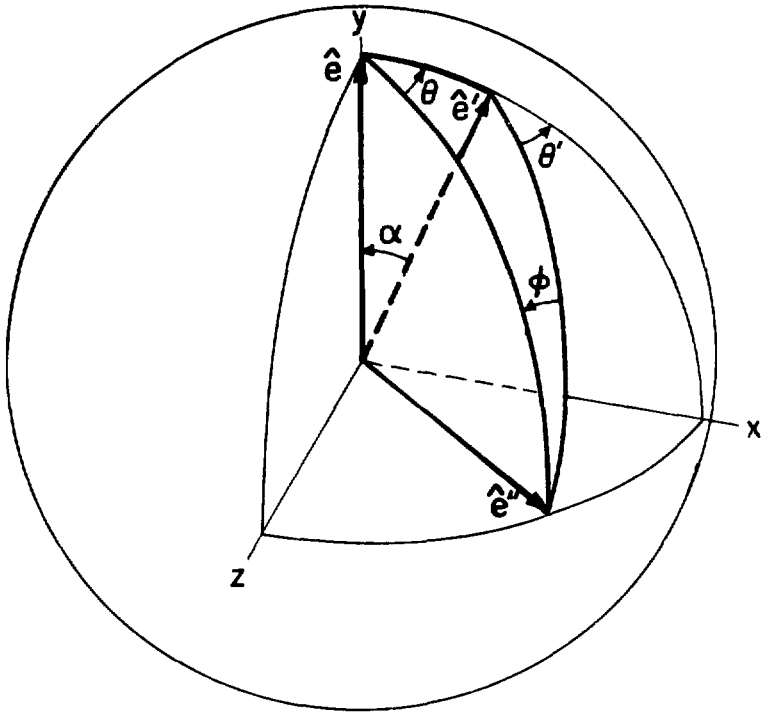

(a)

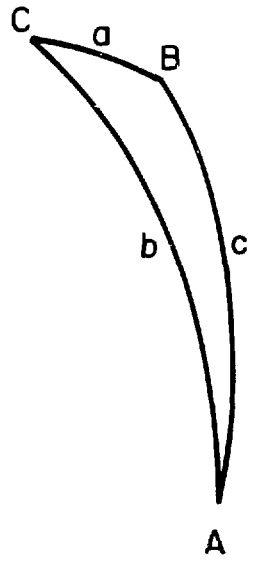

(b)

XBL 802-4669

Figure C.2

rotation about the y axis and an error rotation about a perpendicular axis [as illustrated in Fig. C.2 (a)]. Thus we can write the relationship [from Eq. (A-25)]:

$$R(\hat{e}',2\pi-2\theta')R(\hat{e},2\theta)R(\hat{e}'',2\phi) = I \qquad (C\text{-}1)$$

or

$$R(\hat{e},2\theta)R(\hat{e}'',2\phi) = R^{-1}(\hat{e}',2\pi-2\theta')$$

$$R^{-1}(\hat{e}',-2\theta') = R(\hat{e},2\theta)R(\hat{e}'',2\phi)$$

$$R(\hat{e}',2\theta') = R(\hat{e},2\theta)R(\hat{e}'',2\phi). \qquad (C\text{-}2)$$

Here the subscripts specifying the points through which the axes of rotation pass are omitted since they all pass through the origin. The aligned rotation is represented by $R(\hat{e},2\theta)$, the error rotation by $R(\hat{e}'',2\phi)$, and the misaligned rotation by $R(\hat{e}',2\theta')$, with the unit vectors and angles illustrated in Fig. C.2 (a).

A useful example to consider is the following. The angle θ' between the mirrors can be adjusted enough to give a desired angle 2θ for the aligned rotation, but the axis of the two mirrors is misaligned out of the beamsplitter plane by a small angle α which cannot be eliminated. What is the angle 2ϕ of the error rotation representing the misalignment? The axis $\hat{e}''$ of the error rotation is fixed by ϕ and the choice $\hat{e}\cdot\hat{e}'' = 0$. The law of sines for spherical triangles as in Fig. C.2 (b) states

$$\sin A/\sin a = \sin B/\sin b = \sin C/\sin c, \qquad (C\text{-}3)$$

from which follow the relations

$$\frac{\sin\phi}{\sin\alpha} = \frac{\sin(\pi-\theta')}{\sin\pi/2} = \frac{\sin\theta}{\sin\gamma} \qquad (C\text{-}4)$$

where γ is the angle between $\hat{e}''$ and $\hat{e}'$. Applying the law of cosines:

$$\cos a = \cos b \cos c + \sin b \sin c \cos A \qquad (C\text{-}5)$$

to find $\cos\gamma$ yields

$$\cos \gamma = 0 + \sin \alpha \cos \theta. \qquad \text{(C-6)}$$

Equations (C-4) and (C-6) combine to yield

$$\sin \phi = \frac{\tan \theta}{\tan \gamma} . \qquad \text{(C-7)}$$

From Fig. C.2 (a) we see that for small α, $\theta' \approx \theta$ and $\gamma \approx \pi/2$.

The relation in Eq. (C-2) represents the transformation for the beam (designated beam A in Appendix A) which is transmitted each time it encounters the beamsplitter. A corresponding relation for beam B must include a reflection by the beamsplitter on entering and again on leaving the interferometer, along with a reversal of the order of the transformations within the interferometer, resulting in a reversal of the rotation $R(\hat{e},2\theta')$ to $R(\hat{e}',-2\theta')$. To compare the two beams, we start with the spherical triangle obtained by substituting $M(\hat{z})\hat{e}''$ for $\hat{e}''$. This is identical to the triangle used above except for the reflection in the x-y plane. Corresponding to Eq. (C-1) we have

$$R(\hat{e},2\pi-2\theta')R[M(\hat{z})\hat{e}'',2\phi]R(\hat{e},2\theta) = I \qquad \text{(C-8)}$$

which is the same except for the permuted order. From this we obtain

$$R(\hat{e}',-2\theta') = R(\hat{e},-2\theta)R[M(\hat{z})\hat{e}'',-2\phi]. \qquad \text{(C-9)}$$

To take into account the beamsplitter reflections, we multiply on the left and on the right by $M(\hat{x})$ in Eq. (C-9). After using the fact that $M(\hat{x})$ is its own inverse, we have

$$M(\hat{x})R(\hat{e}',-2\theta')M(\hat{x}) = M(\hat{x})R(\hat{e},-2\theta)M(\hat{x})M(\hat{x})R[M(\hat{z})\hat{e}'',-2\phi]M(\hat{x}) \qquad \text{(C-10)}$$

or

$$M(\hat{x})R(\hat{e}',-2\theta')M(\hat{x}) = R(\hat{e},2\theta)R[M(\hat{x})M(\hat{z})\hat{e}'',2\phi] \qquad \text{(C-11)}$$

with the help of Eq. (A-14) [and $M(\hat{x})\hat{e} = \hat{e}$]. Since $\hat{e}''$ is perpendicular to $\hat{e}$ (or $\hat{y}$), it is in the x-z plane, and the two reflections $M(\hat{x})M(\hat{z})$ result in an inversion of $\hat{e}''$. Therefore, we find for the

transformation corresponding to beam B:

$$M(\hat{x})R(\hat{e}',-2\theta')M(\hat{x}) = R(\hat{e},2\theta)R(-\hat{e}'',2\phi)$$

$$= R(\hat{e},2\theta)R(\hat{e}'',-2\phi), \qquad \text{(C-12)}$$

which is identical to the result [Eq. (C-2)] for beam A except for the sign of the error rotation.

The expressions derived above [Eqs. (C-2) and (C-12)] are needed to explain the peculiar behavior of a misaligned interferometer (see Chapter IV.B.1: Interferometer). If one observes the fringes through the interferometer, they change spacing as the eye is moved parallel to the fringes, and they tilt if the eye is moved perpendicular to the direction of the fringes. Sometimes they can be made to rotate continuously by moving the eye in a circle about some point of observation. As the eye is moved to this point the fringes expand until they disappear. Such behavior is unacceptable because the transmission of light to a detector from each source varies across the wavefront incident on the detector rather than being dependent only on the position of the source.

The reason for this behavior is explainable using the error rotations introduced above. The common rotation in Eqs. (C-2) and (C-12) serves essentially to rotate the line-of-sight, or optical axis, through the interferometer from the input axis to the exit axis. Since it is the same for the two beams, it does not enter into the interference effects. Inspection of a diagram of the interferometer [e.g., Fig. A.1 (a)] shows that the angle by which the optical axis should be rotated is twice the angle of incidence at the beamsplitter plane. Comparison with Fig. C.2 (a) then shows the error rotation axis is parallel to the optical axis.

To analyze the behavior, we determine the interference pattern for an eye position or detector point $\underline{r}$. Field propagation to the point $\underline{r}$ via the two beams A and B is determined by finding the propagation (in the absence of the interferometer) to corresponding points $\underline{r}_A$ and $\underline{r}_B$ such that

$$\underline{r} = R(\hat{e},2\theta)R(\hat{e}'',2\phi)\underline{r}_A \qquad \text{(C-13)}$$

and

$$\underline{r} = R(\hat{e},2\theta)R(\hat{e}'',-2\phi)\underline{r}_B, \qquad \text{(C-14)}$$

from Eqs. (C-2) and (C-12), which describe the effects of the interferometer. Imagining the eye or detector positioned instead at $\underline{r}'$, where

$$\underline{r}' = R(\hat{e},-2\theta)\underline{r} = R(\hat{e}'',\pm 2\phi)\underline{r}_{A,B}, \qquad \text{(C-15)}$$

with the plus (+) corresponding to the first subscript A, and the minus (-) to B, allows elimination of the common rotation. From Eq. (C-15) we see that $\hat{e}''$ defines the direction of an axis of symmetry (through the origin) parallel to the line of sight, and it becomes apparent that the interference effects should have the appropriate symmetry implied in the behavior described above.

To complete the prediction of the interference behavior, we consider a plane wavefront described by a wavevector $\underline{k}$ (nearly parallel to the optical axis) and the point $\underline{x}$ where the wavefront and the optical axis intersect. If $\underline{r}'$ is at a distance ρ' from the axis, it follows that $\underline{r}_A$ and $\underline{r}_B$ are also at that distance, and separated by $2\rho' \sin 2\phi$ from each other, along the line perpendicular to both the axis and the radial component $\underline{\rho}'$ of $\underline{r}'$. The wavevector should be described in terms of its magnitude and the angles it makes with the axis in the directions parallel and perpendicular to $\underline{\rho}'$. Only

the angle β perpendicular to $\underline{\rho}'$ affects the phase difference $\underline{k}\cdot\underline{r}_A - \underline{k}\cdot\underline{r}_B$ between the two points $\underline{r}_A$ and $\underline{r}_B$:

$$\underline{k}\cdot\underline{r}_A - \underline{k}\cdot\underline{r}_B = 2k\rho' \sin \beta \sin 2\phi. \qquad \text{(C-16)}$$

From this equation we can predict fringes parallel to the line from the axis to the observation point ($\underline{\rho}'$) with spacing varying inversely as the distance, fitting the behavior described.

A similar misalignment of the rotation axis would result from any added component that introduced an error rotation. The case discussed above is easily adapted to any error rotation about the origin in the x-z plane by redefining the x and z axes. For example, exchanging the x and z axes in Fig. C.2 (a) covers the case where the error rotation is about an axis perpendicular to the line of slight (and to the desired rotation) and misaligns the rotation axis by an angle α in the plane of the beamsplitter. The points $\underline{r}_A$ and $\underline{r}_B$ will be separated by $2\rho' \sin 2\phi$ along the line of sight and Eq. (C-16) becomes

$$\begin{aligned} \underline{k}\cdot\underline{r}_A - \underline{k}\cdot\underline{r}_B &= 2k\rho' \cos \beta \sin 2\phi \\ &\approx 2k\rho' \sin 2\phi. \end{aligned} \qquad \text{(C-17)}$$

For a given incident direction, the interference changes by one fringe over a change in distance of

$$\Delta\rho' = \lambda/2 \sin 2\phi \qquad \text{(C-18)}$$

from the axis of the error rotation. This effect is also likely to impair the performance of the interferometer, unless ϕ is very small or the error rotation axis happens to be at some distance along the line of sight nearly in front of or behind the detector.

When we consider error rotations introduced by other components in the interferometer, rather than by mirror misalignment, we need a

generalization of the above treatment to allow for skewed error rotations--rotations about an axis which does not pass through the origin. The generalization is straightforward, involving the relation between rotations of equal angle about parallel axes given in Appendix A [Eq. (A-23)], and it is not analyzed here.

Finally, the analysis given above may be used to determine the effects of an imperfect beamsplitter (see Chapter IV.B.1: Interferometer). Ideally, the beamsplitter is a perfect cube, or at least a rhombic prism, so that for the incident light direction for which the reflected component leaves normal to the exit face, the transmitted component also leaves normal to the other exit face. Otherwise the transmitted component is deflected at an angle from the direction it would have exited. For small errors and for points reasonably near the line of sight at sufficient distance from the beamsplitter, we can treat this error approximately as an error rotation about the line of intersection between the planes of the exit face and the ideal exit face. The ideal exit face is the reflection in the plane of the beamsplitting surface of the other exit face.

Since the axis of the error rotation is in the plane of the beamsplitter face, its direction could be anywhere from parallel to the desired rotation to perpendicular to it (and the line of sight). The latter case is analyzed above, while the former case clearly just modifies the angle of rotation without misaligning. Of course the wavelength dependence of the error could prove important for an achromatic interferometer. Otherwise it does not cause any undesirable effects. This is a useful consideration if a round window beamsplitter is used instead of a prism. It could be rotated to eliminate problems caused by the faces not being parallel.

APPENDIX D: THE DETECTOR-AMPLIFIER CIRCUIT

In Chapter IV a simplified detector-amplifier is described to illustrate the basic operating principles and noise sources of the actual circuit which is diagrammed in Fig. D.1. The purpose of this appendix is to discuss some of the details of the actual circuit. Figure D.2 is an equivalent circuit for use in the analysis.

Both detectors are coupled to a single amplifier in the differential mode, and two parallel feedback networks are provided, one to determine the output response to signal current and the second to provide high frequency stability and incorporate the shielding of the detector leads. The latter function is accomplished by using the capacitance between each signal conductor and an inner shield for capacitor C_2, and that between the inner shield and a second shield for C_1. In addition a third shield included around the shield connected to the output is grounded to help prevent spurious coupling between the output and input. The capacitance between these two shields adds to the loading of the output and is not shown.

The resistance capacitor combination R_3 - C_3 between the two inner shields forms a voltage divider with capacitors C_1, attenuating the negative feedback reaching the inputs through capacitors C_2. This is a version of "T" network feedback adapted to the balanced circuit needed for the differential mode signal expected in the two detectors. In Fig. D.2, one "T" network from the output to the inverting input consists of the impedances Z_1 and Z_2 of the shield capacitances C_1 and C_2, and one-half the impedance Z_3 of the combination R_3 - C_3. A corresponding "T" goes from the ground to the

Figure D.1 Detector-amplifier circuit providing differential response to the current in the two photodiode detectors. The two series capacitances C_1 - C_2 are each formed by a pair of shields around the lead between the diode and the amplifier input. The combination R_3 - C_3 is connected between the two inner shields. The feedback resistors R are 511kΩ metal film resistors. Other values are: C_3 = 1000 pf, R_3 = 18Ω, C_1 ≈ 20 pf, and C_2 ≈ 10 pf.

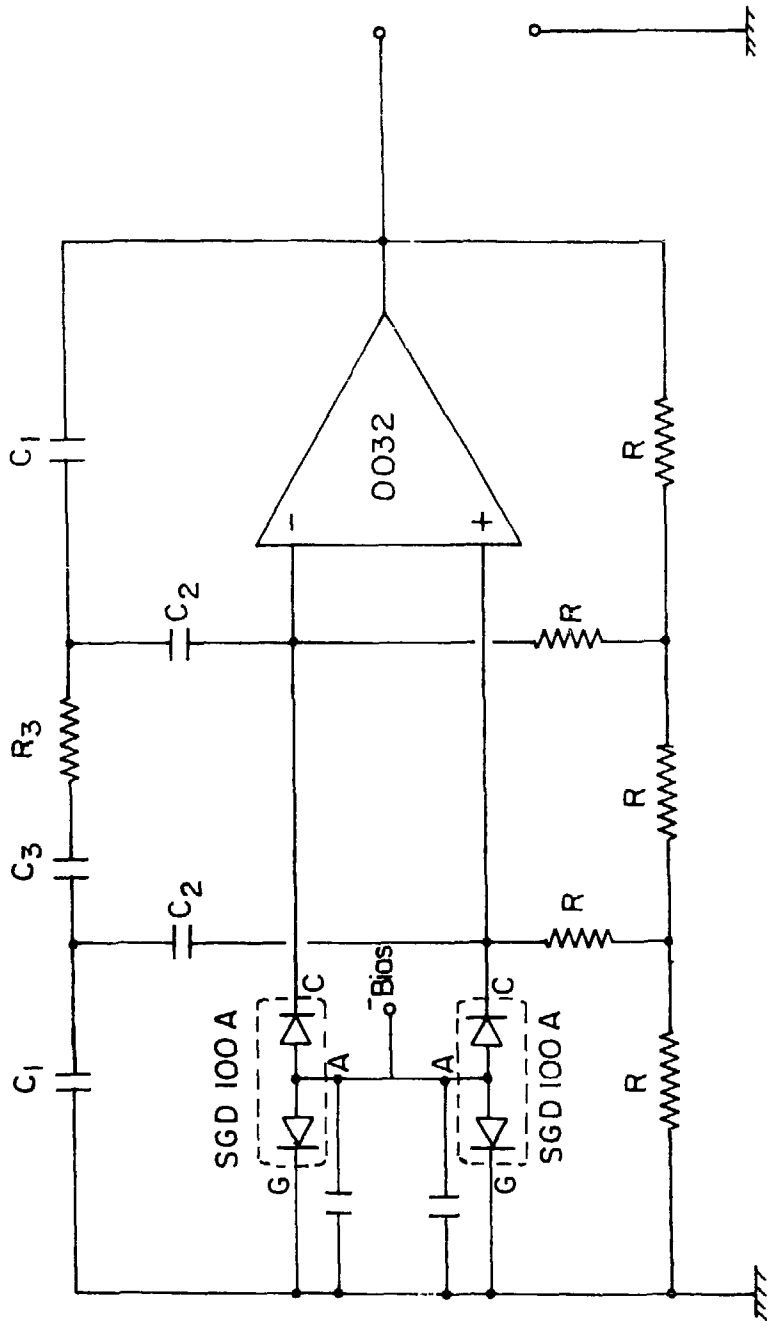

Figure D.1

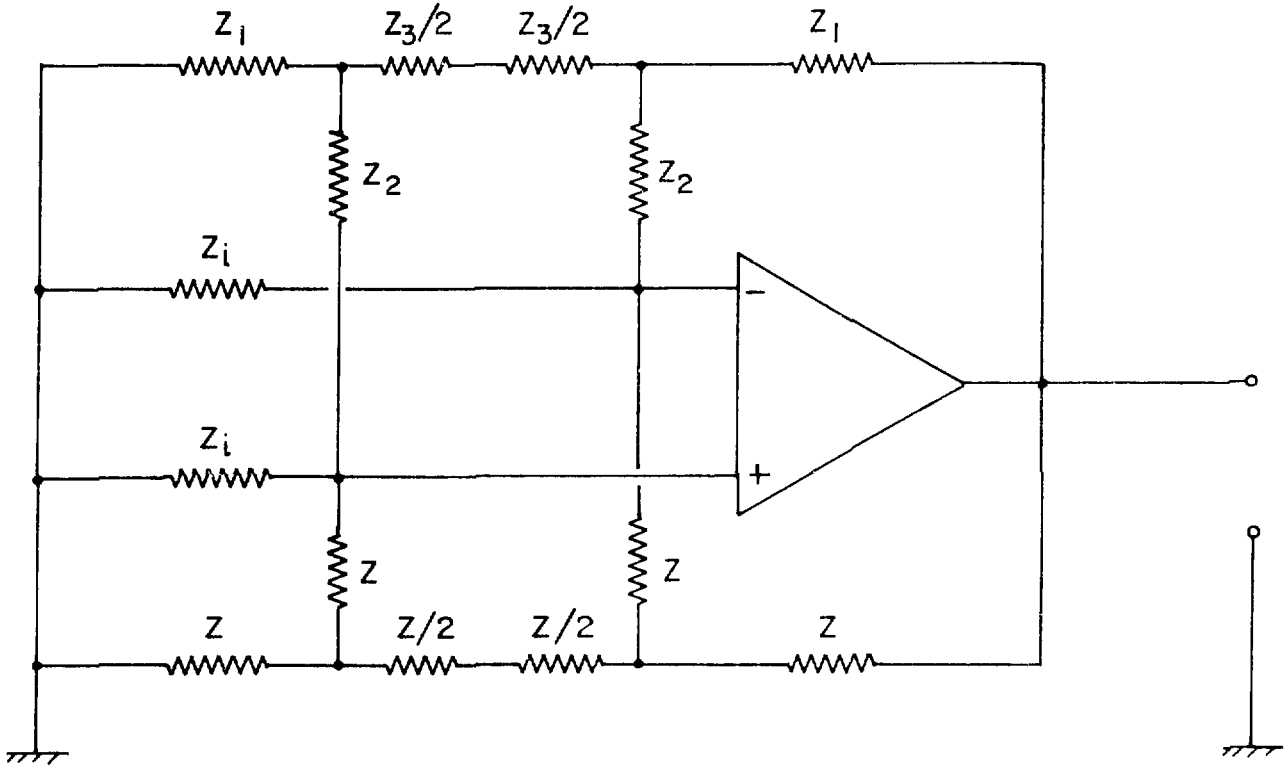

XBL 803-4913

Figure D.2 Detector-amplifier equivalent circuit. The feedback resistors are represented by an impedence Z which includes the stray capacitance of the components.

non-inverting input. The network of five resistors R are shown forming a similar pair of "T's," where their impedance is labeled Z' (to allow for effects of stray capacitance).

The attenuation of the feedback in a "T" network is used to simulate feedback impedances, for example, by using smaller resistances with minimal stray capacitance problems to obtain a higher effective resistance. For the purpose of determining the output voltage response to an input (differential mode) current, the "T" network consisting of Z_1, Z_2, and $Z_3/2$ is equivalent to an effective impedance Z_{eff}, where

$$Z_{eff} = (Z_1 + Z_2)\left(1 + \frac{Z_1 Z_2}{Z_1 + Z_2}\frac{2}{Z_3}\right). \qquad \text{(D-1)}$$

From Eq. (D-1) it follows that the effective impedance of each half of the network of resistors is four times the impedance of each resistor.

As far as the noise performance is concerned, some sacrifice is made in using the network instead of an actual feedback impedance Z_{eff}. The thermal noise is due mainly to the resistive feedback network. If the two "T" networks were replaced by the two effective feedback impedances $4Z$, the differential mode noise current across them would be given by the Johnson noise formula:

$$i_n^2 = \frac{2}{\pi} kT \, \mathrm{Re}\frac{(8Z)}{|8Z|^2} \, d\omega, \qquad \text{(D-2)}$$

where k is Boltzmann's constant, and T is the temperature. This current just flows in the feedback impedance (since there is no voltage between the ideal amplifier inputs, no current can leave via the amplifier inputs or the input impedances), resulting in the same output noise voltage as if the current appeared across the inputs.

When the combined noise power of the network is computed and expressed as an input noise current squared, the result is larger than that given in Eq. (D-2) by a factor of three

Similarly, the response to amplifier voltage noise is larger than if the effective feedback impedance were realized with an actual pair of components from the output to the inverting input and from ground to the non-inverting input. In the latter case, the noise voltage indicated as a differential voltage source v_a in series with the inputs in Fig. D.3, is equivalent to a noise current source across the input of magnitude

$$i_n = v_n\left(\frac{1}{2Z_i} + \frac{1}{2Z_{eff}}\right), \qquad (D\text{-}3)$$

i.e., equal to the current drawn by the parallel combination of the input and feedback impedances. With the "T" network, the equivalent current drawn is increased to

$$i_n = v_n\left[\frac{1}{2Z_i} + \frac{1}{2Z_2}\left(1 - \frac{2Z_1}{Z_{eff}}\right)\right]. \qquad (D\text{-}4)$$

The amplifier current noise appears exactly as any differential mode input current source would, and therefore the response is the same with the network as with the equivalent impedance represented by the network.

Figure 1.3 Detector-amplifier equivalent circuit with some noise sources indicated. The amplifier input voltage and current noise are v_{na} and i_{na} respectively, and the thermal noise of the feedback resistors is indicated by current sources i_{nf}. The voltage sources $\pm v_o/2$ indicated by the small triangles are inserted to indicate a way to determine the response of the circuit as a superposition of the $+v_o/2$ and $-v_o/2$ solutions.

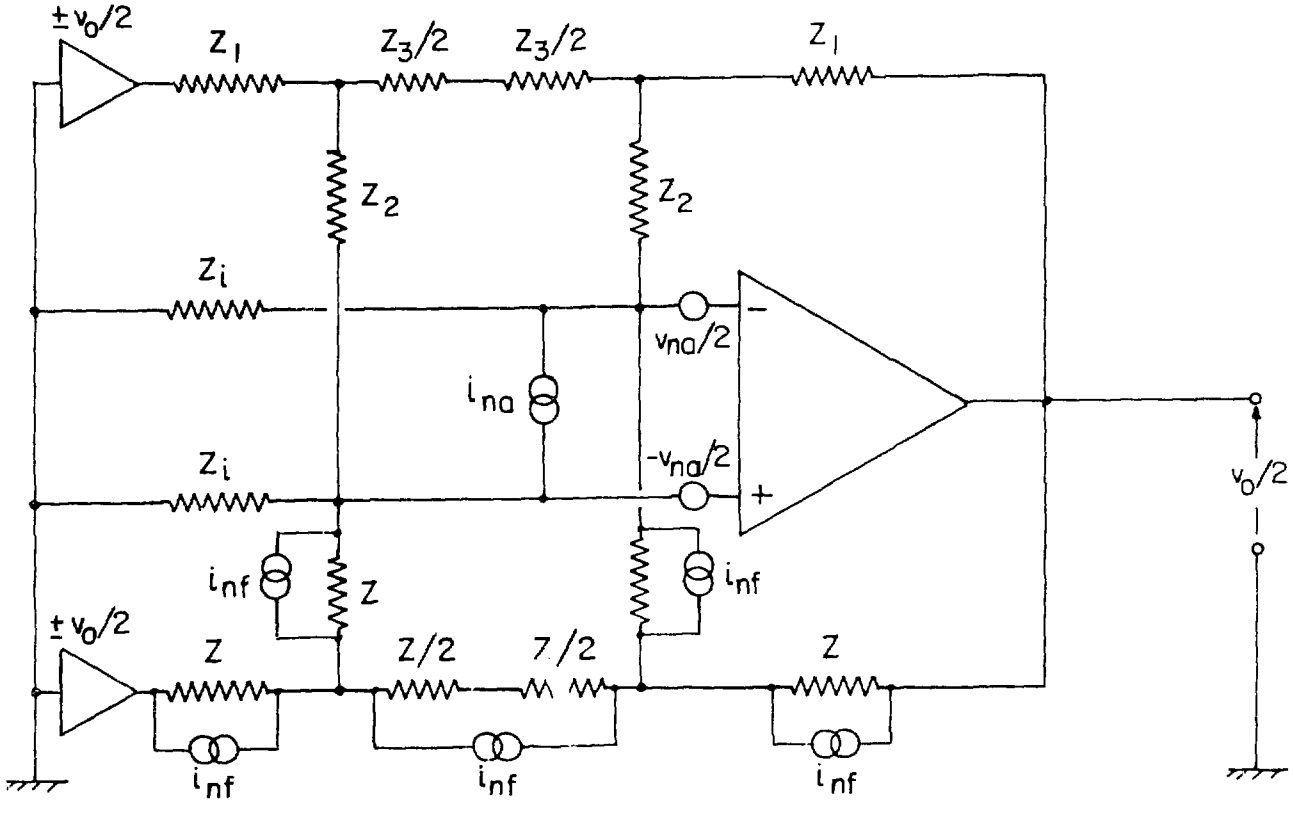

XBL 803-4930

Figure D.3

APPENDIX E: STEREO VIEWING BY THE CROSSED EYES METHOD

In Chapter IV, Figs IV.12 through IV.20 show spectral density versus wavenumber curves for a number of frequencies on the same plot. The frequencies are distinguished by shifting the origin according to the frequency for each curve, simulating a projection of a three-dimensional plot. Changing the origin displacement versus frequency slightly to the left gives a new projection showing parallax effects as if the curves for the higher frequency were farther away before they were projected into a single plane. With some study, one can distinguish the overlapping curves by comparing the two views.

Better still, one can use the pairs of plots for stereoscopic viewing. As they are presented, the pairs of plots are compatible with the crossed eyes method of viewing used by Scorer.[1] This method requires no equipment and can be learned by as many as two out of three persons. I explain the method below, but if the reader has another method, he should note that the view for the left eye is on the right in each figure.

Stereo viewing requires that separate images for the two eyes be registered, that is, made to coincide so that they may be interpreted as images of a single scene as viewed by the two eyes (with slightly different perspective). When actually viewing an object, the eyes have to do this by shifting inward or outward according to the distance so that the lines of sight converge at the object. Otherwise, double images are seen, as when one goes cross-eyed.

When a stereo picture pair is viewed, the two separate images can be registered by crossing the eyes so that the left eye is centered

on the picture to the right, while the right eye is centered on the picture to the left. The problem is that most of us have learned to coordinate focusing with convergence of the eyes. Since the line of sight converges in front of the pictures, we focus our eyes too near to see the pictures clearly. The method requires learning to relax the coordination between the focus and convergence of the eyes.

To learn the crossed eyes method, it may be helpful to practice with two small identical objects such as coins, screws, or bottle caps. Start by placing them close together compared with the distance between the eyes, so that the error in focusing caused by crossing the eyes to view them will be minimized. They should be lined up parallel to the line between the two eyes, or the head tilted so that the images may be registered. Crossing the eyes should then produce two pairs of images in a line, and if the convergence of the eyes is correct, the inner two will be merged into one, probably blurred, image. This is the image on which to concentrate.

Scorer suggests it may be helpful to bring two cards, preferably black, close together between the eyes and the objects (or pictures) so that the middle image is seen between the cards, and the other two images become less noticeable. Alternatively, the objects could be viewed through a card with a hole in it placed where the lines of sight of the two eyes should converge. (You can also make a mask with your hands, fingers overlapping at right angles, leaving an opening between the crooks of your thumbs large enough to see one of the objects.) Looking at the hole in the mask and moving it toward and then away from the eyes, one should then be able to make the objects appear to separate and merge into one, although of course it is the hole which will be in focus.

Once the two images can be registered it is necessary to bring them into focus at the same time. This requires some experimentation since it is an unfamiliar use of the eyes. Moving toward or away from the objects and back again may help. The focus change seems to require relaxation as opposed to forcing, so the eyes should not feel strained. Rather than squinting, try allowing the eyelids to droop a little or to blink a few times.

If the stereo view is first obtained with the two matching objects placed close together, it should be practiced for larger separations until a transition can be made to the plots in Figs. IV.12 through IV.20. The image of the objects will be exaggerated stereo because the parallax is greater than for the two eyes viewing one object at the same distance. The exaggeration is not always obvious, however.

For those who find this method difficult to learn it may be easier to obtain or make a viewer using a pair of magnifying lenses to form overlapping virtual images of the two views. This would result in an inverted stereo image, with the frequency axis projecting outwards and upwards and the curves seen from below. The pictures may be too large and therefore too far apart to register easily with a viewer, in which case it would be necessary to reproduce them on a smaller scale, and they could then be switched to avoid the inverted stereo effect.

REFERENCE

1. R.S. Scorer, Clouds of the World (David & Charles, Newton Abbot Devon, 1972), pp. 170-171.